12-2019

Characterizing Hydrothermal System Groundwater Dynamics Using Conservative and Non-conservative Tracers: Insights and Implications Drawn from Study at the Taupo Volcanic Zone (New Zealand) and Valles Caldera (USA)

Joshua Michael Blackstock
University of Arkansas, Fayetteville

Characterizing Hydrothermal System Groundwater Dynamics Using Conservative and Non-conservative Tracers: Insights and Implications Drawn from Study at the Taupo Volcanic Zone (New Zealand) and Valles Caldera (USA)

A dissertation submitted in partial fulfillment
of the requirements for the degree of
Doctor of Philosophy in Geosciences

by

Joshua M. Blackstock
University of Arkansas at Little Rock
Bachelor of Science in Geology, 2003
University of Canterbury
Master of Science with First Class Honours in Geology, 2011

December 2019
University of Arkansas

This dissertation is approved for recommendation to the Graduate Council

Phillip D. Hays, PhD
Dissertation Director

Matthew D. Covington, PhD
Committee Member

Kenneth L. Kvamme, PhD
Committee Member

Kristofor R. Brye, PhD
Committee Member

Benjamin R. K. Runkle, PhD
Committee Member

Abstract

Hydrothermal systems constitute an important component of heat and mass transport within Earth's crust having direct and indirect impacts to society. Investigating contemporary hydrochemical differences and change are critical to evaluating and deconvolving factors that influence geothermal systems through time. In this dissertation, groundwater mixing approaches were used to study hydrochemical differences in two globally significant hydrothermal areas, which included fabrication of a low-cost dissolved CO_2 monitoring for dissolved inorganic carbon (DIC). In the Taupo Volcanic Zone (New Zealand), empirical spatial relations were used to derive low-temperature groundwater end-members of Cl and Cl/Br for end-member mixing analysis (EMMA). Using EMMA, mixing ratios exhibited a wide-range of dilutions and Cl/Br ratios between low- and high-temperature groundwater sources. To explain Cl/Br differences in selected hydrothermal surface features, fluid recirculation is inferred. In the Valles Caldera, NM (USA), mixing analysis consisted of DIC and $\delta^{13}C_{DIC}$ analyses of surface water along the Jemez River. Results and findings presented dissolved CO_2 versus HCO_3 concentration, CO_2 versus HCO_3 loads, and $\delta^{13}C_{DIC}$ relations from which four groundwater end-members were interpreted. This corroborated with previous investigations using trace-element chemistry. Analysis of historical DIC data was used to determine seasonal patterns of DIC loads. Seasonal changes in DIC loads were inferred to be controlled by groundwater-climate feedbacks. A low-cost, Arduino-interfaced monitoring platform (LAMP) was also used to monitor dissolved CO_2 (CO2-LAMP) at sites in the Valles Caldera and in Northwest Arkansas. The CO2-LAMP demonstrated replicable and accurate measurements compared to reference gases. Also, the platform captured hourly variability of CO_2 in cave air, soil atmosphere, and dissolved CO_2 in a cave stream. Humid cave air and dissolved CO_2 results were found to be within 15% of a more expensive infrared gas analyzer. For dissolved CO_2, this range in measurement difference is regularly

observed among methods. Formulation of gas analyzer operation found "corrections" currently made to dissolved CO_2 measurements using membrane-enclosed infrared gas analyzers are unwarranted. This body of research presented empirical spatial analysis, EMMA, instrumentation development, and DIC and $\delta^{13}C_{DIC}$ analyses which provides new inferences as to the nature and extent of hydrothermal fluid circulation in Earth's crust.

Acknowledgements

This dissertation would not have been possible without the keen guidance and unwavering support my PhD committee: Phillip D. Hays, Matthew D. Covington, Kenneth L. Kvamme, Kristofer R. Brye, and Benjamin R. K. Runkle. Phil, you have been a great friend, an excellent adviser, and an artesian well of enthusiasm. I look forward to the upcoming expeditions and science along the Black River and more soccer on Saturday and Sunday. Matt, you, too, have been a great friend and adviser and I look forward to more adventures in caves, gas, and mass. . .transport. A very important thank you must also go to my original PhD committee when I originally started this PhD journey at the University of Canterbury in Christchurch, New Zealand: Travis W. Horton, Darren Gravley, Cindy Werner, Wendy Calvin, and Kevin L. Brown.

Funding for this dissertation is gratefully acknowledged and was bestowed from the Walton Foundation, the Department of Geosciences at the University of Arkansas, the J. William Fulbright College of Arts and Sciences at the University of Arkansas, the University of Arkansas Graduate School, the Geological Society of America, the American Association of Petroleum Geologists, the Geothermal Resources Council, and the Evolving Earth Foundation.

An incalculable amount of thanks must also go to my comrades of Oz27. Chelsea, Max, Victor, Celia, Kelly, Ruby, and Ryan. I only hope that an equal amount of mayhem, mischief, and fun continues in the confines of this little corner of the universe.

Copious thanks must also go to the Department of Geosciences at the faculty and students within the Department of Geosciences at the University of Arkansas. I cannot overstate my esteem for this department and the feeling of collegiality that has come with my small part in its

day to day ongoings. To Lisa, JoAnne, Theresa, Jackie, and Amanda, thank you for always being patient and helpful. You all keep the show running!

Katie, your love and support has been tremendous. I am very much grateful for you.

To my family, these acknowledgements would not be here for your support over these past several years.

Dedication

To my family, a second text twice in length to this dissertation might just begin to capture my earnest thanks.

Table of Contents

List of Published Papers

Chapter 2, in preparation
Blackstock, J.M., Hays, P.D., Horton, T.W., Brown, K.L., in preparation, Br-Cl mixing relations in the Taupo Volcanic Zone, New Zealand: Insights and open questions: Journal of Hydrology

Chapter 3, in preparation
Blackstock, J.M., Hays, P.D., Covington, M.D., in preparation, Variable carbon sources and mass fluxes in a hydrothermal watershed, Valles Caldera, New Mexico (USA): implications for tracing surface water sources and lithospheric carbon: Journal of Geophysical Research–Solid Earth.

Chapter 4, in review
Blackstock, J.M., Covington, M.D., Perne, M., Myre, J.M., in review, Monitoring atmospheric, soil, and dissolved CO_2 using a low-cost, Arduino monitoring platform (CO2-LAMP): theory, fabrication, and operation: Frontiers in Earth Science

Chapter 1: Introduction

Whether in natural or human-influenced environments, fluid migration and chemistry are highly variable in groundwater systems (Ingebritsen and Sanford, 1999). Owing to its pervasiveness in the subsurface, groundwater plays a critical role in not only geologic, but biologic and climatic processes in the Earth System (Tóth, 1999; Bovolo et al., 2009; Davidson et al., 2010; Fan, 2015; Hernández-Antonio et al., 2015; Szynkiewicz et al., 2019). In turn, these processes drive both small and large-scale mass transport within the crust and to terrestrial environments (Tóth, 1999; Ingebritsen et al., 2010; Fan, 2015; Duvert et al., 2018). Groundwater flow paths and chemical compositions may exhibit drastic changes due to variable hydroclimatic, tectonomagmatic, and human perturbations (King, 1986; Arnórsson and Andrésdóttir, 1995; Brahana et al., 1999; Alley, 2002; Glover and Mroczek, 2009; Stewart, 2012; Kresse et al., 2014). Thus, for groundwater systems with limited water level observations, geophysical data, or numerical simulation, chemistry derived from available boreholes and springs are the best indicators of the groundwater system at depth, particularly for hydrothermal systems (Ingebritsen and Sanford, 1999; Kissling and Weir, 2005; Lowenstern and Hurwitz, 2008; Cullen et al., 2015).

This body of research sought to further understanding of groundwater mixing in hydrothermal systems using: 1, halogen species; 2, dissolved inorganic carbon and stable isotope geochemical of $\delta^{13}C_{DIC}$; and 3, low-cost dissolved monitoring to elucidate groundwater mixing in hydrothermal watersheds. Specifically, the three primary research questions of this dissertation were:

1. Are end-member mixing analyses (EMMA) models using Br and Cl appropriate for tracing and interpreting groundwater flow paths in hydrothermal systems? How are end-members estimated, particularly when a paucity of data exists?

2. Where hydrothermal fluid emergence at the surface is known, are inorganic carbon inputs, specifically CO_2, from hydrothermal systems traceable using related inorganic carbon speciation and stable isotopic compositions? Are contributions significant?
3. Would using a low-cost, CO_2 infrared gas analyzer (IRGA) and microcontroller be a viable alternative, cost-effective method to measure and record (or log) dissolved CO_2 measurements in surface waters and other environments (e.g. groundwater, soil)? If so, how would this system compare with more typical, higher-cost platforms?

Geothermal systems and hydrothermal fluid circulation in the subsurface

At depth, heat is transferred from a source (e.g. magma) to surrounding rock formations and formation-hosted fluids (i.e. groundwater) via conduction, advection, or variable combinations between these two. Predominance of conductive or advective heat transfer in the crust primarily depend on three geophysical parameters: 1) heat flux (or heat flow) from the source; 2) rate of groundwater flow through fluid-hosted rock formations (i.e. permeability); and 3) rate of heat removal from the heat source (Burns et al., 2015). Relations between these geophysical parameters are described numerically by the dimensionless Rayleigh-Darcy number. In general, with increasingly lower Rayleigh-Darcy numbers, groundwater movement is characterized by slower flow rates, which increases heat transfer via conduction. However, with an increasing value of the Rayleigh-Darcy number, groundwater flow rates are higher. In turn, heat transfer from the heat source to surrounding geologic media (i.e. lithologic formations and fluids) via advection is more prevalent. In regions of the crust with sufficient permeability, ample groundwater recharge, and sustained elevated heat fluxes, heat transfer from the lower crust upwards to Earth's surface will occur primarily through advection via hydrothermal groundwater (Bibby et al., 1995; Hochstein, 1995; Ague, 2014).

While advection and convection are often stated interchangeably (Saar, 2011), convection as discussed here is defined as a type of groundwater advection (i.e. transport of heat and mass) (Ingebritsen and Sanford, 1999). Specifically, hydrothermal groundwater movement and heat transfer as advection can be categorized between two end-member convection models: 1, forced convection (or pipe flow); and free convection driven by buoyant forces (Burns et al., 2015). In forced convection, high- and low-temperature groundwater movement is driven by hydraulic gradients, such as topographic relief, between groundwater recharge and discharge areas. Moreover, Rayleigh-Darcy numbers are not high enough to generate groundwater flow purely by temperature-density differences. Therefore, groundwater may be heated from various sources in the crust, but hydraulically driven flow and high permeability conduits (i.e. fracture sets, faults) are necessary for high-temperature groundwater movement and discharge back at the surface as thermal springs below critical Rayleigh-Darcy values (Elder, 1966; Freeze and Cherry, 1979). Examples of forced convection-type hydrothermal groundwater systems include hot springs discharge within the Ouachita Mountains, USA (e.g. Hot Springs National Park) (Kresse and Hays, 2009), Appalachian Mountains (Lowell, 1975), and Noto Peninsula, Japan (Umeda et al., 2009).

Where Rayleigh numbers are greater than a critical value for a given fluid system, groundwater movement arises from buoyant forces. This movement (i.e. free convection) stems from temperature-density contrasts between high- and low-temperature groundwater (Hayba and Ingebritsen, 1997). Unlike forced convection, movement of high-temperature groundwater towards the surface is not solely dependent on hydraulic gradients. However, hydraulic gradients may affect discharge location. Near the surface, circulating low-temperature groundwater may effectively 'push' rising hydrothermal plumes in free-convection systems toward lower elevations

partially following groundwater flow paths near the surface (Kissling and Weir, 2005; Ratouis and Zarrouk, 2016). In turn, this forms laterally migrating hydrothermal plumes, which in some cases, have been documented to shift high-temperature groundwater discharge emergence up to several kilometers away from location of hydrothermal plume, at depth (Hedenquist, 1982; Giggenbach et al., 1994; Kissling et al., 2009). Free-convection type systems with hydrothermal discharge at the surface are commonly observed within large, caldera-hosted geothermal areas such as those within the TVZ (New Zealand) (Bertrand et al., 2012; Ratouis and Zarrouk, 2016), Yellowstone (USA) (Truesdell et al., 1977; Waite, 2002; Lowenstern and Hurwitz, 2008), Krafla (Iceland) (Truesdell et al., 1989; Dempsey et al., 2012; Scott et al., 2015; Stefánsson et al., 2016), and, in general, submarine mid-ocean ridge hydrothermal systems (Kelley et al., 1992; Johnson et al., 2000; Lupton et al., 2006; Foustoukos and Seyfried, 2007).

In high-relief environments (e.g. stratovolcanoes, montane environments) hosting high-temperature hydrothermal systems, free convection may be present, at depth, but liquid-dominated fluids typically do not reach the summit (Hedenquist and Lowenstern, 1994; Evans et al., 2002; Burns et al., 2015). Rather, higher elevation hydrothermal discharge is dominated by high-steam, acid-sulphate waters caused by phase separation and decoupling of gases from the liquid-dominated hydrothermal plume (Ingebritsen et al., 2013, 2016). As previously described for large caldera-hosted hydrothermal systems, elevated topographic relief yields high hydraulic gradients (i.e. greater movement of low-temperature groundwater) (Ratouis and Zarrouk, 2016). Therefore, in high-relief hydrothermal systems, low-temperature groundwater will drive lateral movement of the hydrothermal plume to the volcanic flanks where controls on hydrothermal groundwater circulation switch to predominately forced-convection and discharge of liquid-dominated fluids occur at lower elevations (Goff et al., 1988; Rogie et al., 2001; Ingebritsen et

al., 2016). Examples of these high-relief, high-steam and liquid-dominated hydrothermal discharge include the Lassen hydrothermal system, USA (Ingebritsen et al., 2016), Mammoth Mountain, USA (Rogie et al., 2001; Evans et al., 2002), and the Valles Caldera, USA (Goff et al., 1985, 1988; Truesdell and Janik, 1986).

More thorough reviews and discussion of heat transfer modes, formulation, and application in modeling groundwater flow within hydrothermal systems are presented in Hayba and Ingebritsen (1997), Ingebritsen et al. (2010), Ingebritsen and Sanford (1999), and Saar (2011).

Major chemical differences in hydrothermal fluids

As hydrothermal groundwater rises to shallower depths, fluids also adiabatically boil giving rise to a two-phase solution (Arnorsson et al., 2007; Stefánsson et al., 2016). In this body of research, hydrothermal systems investigated are predominately liquid-dominated meaning vapor (or steam) dominated components are limited to the upper portions of the hydrothermal system. In both liquid and vapor-dominated systems, transport of water and heat from depth is accompanied by prodigious mass transport of elements and compounds whereby chemical differences of hydrothermal fluids are driven by the predominance of liquid versus vapor dominated regimes (Truesdell and Janik, 1986; Giggenbach, 1987; Fournier et al., 1994; Evans et al., 2002, 2004; Arnorsson et al., 2007; Lowenstern et al., 2014; Scott et al., 2015).

In deeper hydrothermal systems, wells may not penetrate to the base of hydrothermal circulation, as is the case in the Taupo Volcanic Zone (TVZ), but important chemical differences exist at depth. At the base of hydrothermal convection are primary fluids, which are typically acidic, hyper-saline, and gas-rich (Arnorsson et al., 2007). Hydrothermal wells typically extract neutral-chloride fluids, from more shallow hydrothermal reservoirs where fluids have been

buffered by water-rock interaction during ascent (Truesdell et al., 1981; Giggenbach, 1995; Lowenstern et al., 2012). Neutral chloride fluids reaching the surface which form hot pools and springs of neutral pH may still be high in total dissolved solids (TDS), but are often more dilute than hydrothermal reservoir compositions owing to mixing with low-temperature groundwater. Where rising fluids fail to reach the surface, hydrothermal fluids will laterally migrate in shallow aquifers and gases may exsolve from the hydrothermal solution and migrate upwards often forming steaming ground and CO_2-rich soil zones (Giggenbach et al., 1994; Giggenbach, 1995; Stefánsson et al., 2016; Thomas et al., 2016). As steam and vapor collect and condense at the surface, acid-sulphate-type discharge features will form (e.g. mud pools, gryphons, mud volcanoes) (Goff et al., 1985; Charles et al., 1986; Svensen et al., 2009). This general evolution of fluid chemistry is observed in most hydrothermal systems across Earth (Arnorsson et al., 2007), but specific origins for many solutes (e.g. Cl, Br, CO2) are debated (Arnórsson, 1986; Truesdell et al., 1989; Hedenquist et al., 1990; Arnórsson and Andrésdóttir, 1995; Giggenbach, 1995; Martini, 1996; Kerrick and Caldeira, 1998; Fehn and Snyder, 2003; Simmons and Brown, 2006; Bégué et al., 2017).

Mixing models

Mixing models between end-member compositions in groundwater systems provide a useful tool to quantify and qualitatively assess relative proportions of end-member sources in collected water samples (Phillips and Gregg, 2001; Parnell et al., 2010; Horner et al., 2017). Quantitative mixing models are typically used in conjunction with conservative species, whereas qualitative models may incorporate non-conservative species during fluid transport, exact compositional changes of end-members from other processes (e.g. mineralization, degassing) may not be well constrained (Campeau et al., 2017; Horner et al., 2017), but overall trends can

be assessed. Application of conservative tracers like Br and Cl are relatively straight forward whereby a mixture, X_m is equal to the fractional sum of two end-member fractions:

$$X_m = f_A X_A + f_B X_B \quad (1)$$

where f_A and f_B are fractional values for the end-member concentrations of end-member A, X_A, and end-member B, X_B, respectively. Considering a mass-balance, the two fractions, f_A and f_B, should equal one for a given mixture (Phillips and Gregg, 2001):

$$1 = f_A + f_B \quad (2)$$

$$f_A = 1 - f_B \quad (3)$$

As such, end-member fractions and end-member compositions may be derived, respectively:

$$f_A = \frac{X_m - (f_B X_B)}{X_a} \quad (4)$$

Using equation 3, X_A may be solved where f_A is unknown:

$$X_A = \frac{X_m - (f_B X_B)}{(1 - f_B)} \quad (5)$$

An exhaustive presentation of more complex mixing models, while outside the scope of this review, include variable end-member compositions, analytical uncertainty, and in-stream processes (e.g. evapotranspiration, mineralization), which affect modeled mixing fractions (or mixing ratios) (Truesdell et al., 1977; Phillips and Koch, 2002; Liu et al., 2008; Parnell et al., 2010; Horner et al., 2017). In this dissertation research, end-member compositions were independently determined, and mixing ratios were generated based on equation 1.

Natural tracers in hydrothermal systems

While ratios of dissolved boron and chloride are commonly used to estimate mixing between deep hydrothermal wells and hydrothermal surface features, boron is preferentially taken up in alteration mineralogical assemblages at lower temperatures (Ellis and Mahon, 1967;

Arnórsson and Andrésdóttir, 1995; Millot et al., 2012; Reyes and Trompetter, 2012). Effectively, boron does not behave conservatively at lower temperatures, and in turn, using boron for EMMA in hydrothermal systems is temperature limited. In more distal portions of hydrothermal systems, determination of mixing with lower-temperature groundwater is critical to assessing water quality changes based on hydrothermal plume extent.

While not as widely used, Br and Cl are highly soluble in natural waters, with increasing analytical certainty for lower Br concentrations typical of low-temperature groundwaters (Davis et al., 1998, 2004; Fehn and Snyder, 2003; Hurwitz et al., 2005; Bernal et al., 2014; Horner et al., 2017), Cl-Br could more accurately quantify mixing between hydrothermal wells and low-temperature groundwater, particularly at low temperatures and low mixing ratios.

Inorganic carbon fluxes and gas decoupling

Carbonic springs emanating near fault zones (Kerrick and Caldeira, 1998; You et al., 2004; Forrest et al., 2005; Cathles and Schoell, 2007; Banerjee et al., 2011; Schütze et al., 2012), caldera flanks (Goff and Janik, 2002; Evans et al., 2002; Chiodini et al., 2015), and within caldera hosted geothermal systems (Goff and Janik, 2002; Bloomberg et al., 2014; Hanson et al., 2014; Lowenstern et al., 2015) emit large volumes of lithospheric-sourced CO_2 (Rogie et al., 2001; Kerrick, 2001; Crossey et al., 2009). In hydrothermal areas, discharge of high CO_2 upflow may manifest as acidic ground with high soil CO_2 fluxes (Werner et al., 2000; Chiodini et al., 2005; Lewicki et al., 2005), bicarbonate springs (Evans et al., 2002; Lewicki and Oldenburg, 2005), or acid-sulphate waters (Giggenbach, 1987; Giggenbach et al., 1994; James et al., 1999; Bergfeld et al., 2008; Lowenstern et al., 2012). As CO_2 may decouple from circulating hydrothermal groundwater (Truesdell et al., 1989; Lowenstern et al., 2012; Stefánsson et al., 2016), typical methods of tracing groundwater mixing using more soluble species? (e.g. Cl, B),

as previously mentioned, may inherently not capture the full range of CO_2 sources due to decoupling from the liquid solution. Methods and application of EMMA tracing CO_2 and other inorganic species longitudinally in hydrothermal watersheds from high-CO_2 sources is limited (Evans et al., 2002).

Determination of CO_2 in shallow groundwater and surface waters has great potential for not only tracing hydrothermal inputs and estimating these C inputs within hydrothermal watersheds, but also for monitoring changes in hydrothermal reservoirs at depth (e.g. magmatic inputs, depressurization) and differentiating inorganic carbon variability between geogenic and biologic CO_2 sources for regional and global carbon budgets (Hurwitz et al., 2007; Lowenstern and Hurwitz, 2008; Johnson et al., 2009; Burton et al., 2013; Campeau et al., 2017).

Application of affordable sensors and microcontrollers for environmental monitoring

In the last two decades the availability and use of 'off the shelf' microcontrollers to interface commercially available environmental sensors has increased dramatically in scientific research (Cressey, 2017). This growth comes as the diversity of research questions and increasingly challenging environmental conditions where sensors are being installed have required researchers to seek-out and adopt low-cost sensors and related components (e.g. data loggers) to not only offset capital costs, but manage cost and benefits knowing the potential risks for equipment damage, or in extreme more cases, total equipment loss (Pearce, 2012; Cressey, 2017; Beddows and Mallon, 2018). Many 'proof-of-concept' studies in hydrology, to-date, have focused on typical measured field parameters, such as temperature (Hut et al., 2016). As a parameter of broad importance, development of a low-cost platform to measure and monitor dissolved CO_2 would be applicable not only in hydrothermal systems, but the larger Earth Sciences community.

Organization of the Dissertation

Specific objectives and outcomes are described in the following three chapters, which are presented here as three independent manuscripts intended for submission to peer-review journals. Chapter 2 explores the development and application of a EMMA in the Taupo Volcanic Zone of New Zealand using Br-Cl abundances and accompanying Cl-δ^2H relationships to examine not only the range of mixtures between low- and high-temperature groundwater but the potential role of recirculation to explain Cl/Br ratio changes. Findings were also incorporated into a conceptual model of Br-Cl and Cl-δ^2H evolution in liquid dominated geothermal systems. Chapter 3 investigated changes in DIC and $\delta^{13}C_{DIC}$ along the Jemez River, New Mexico to develop a mixing relations among groundwater components contributing to streamflow in the Valles Caldera geothermal system. Chapter 4 provides an not only details on the fabrication and operation of a low-cost, dissolved CO_2 monitoring platform, but also using first principles, a formulation between dissolved gas concentrations in the water and responses within a membrane-enclosed CO_2 IRGA. Results from field trials in both aquatic and soil environment and recommendations for future iterations are discussed. Lastly, a broader exposition of findings, open questions, and implications stemming from this research are discussed in the Conclusions chapter.

References Cited

Ague, J.J., 2014, Fluid Flow in the Deep Crust, in Treatise on Geochemistry, Elsevier, v. 4, p. 203–247, doi:10.1016/B978-0-08-095975-7.00306-5.

Alley, W.M., 2002, Flow and Storage in Groundwater Systems: Science, v. 296, p. 1985–1990, doi:10.1126/science.1067123.

Arnórsson, S., 1986, Chemistry of gases associated with geothermal activity and volcanism in Iceland: A review: Journal of Geophysical Research: Solid Earth, v. 91, p. 12261–12268, doi:10.1029/JB091iB12p12261.

Arnórsson, S., and Andrésdóttir, A., 1995, Processes controlling the distribution of boron and chlorine in natural waters in Iceland: Geochimica et Cosmochimica Acta, v. 59, p. 4125–4146, doi:10.1016/0016-7037(95)00278-8.

Arnorsson, S., Stefansson, A., and Bjarnason, J.O., 2007, Fluid-Fluid Interactions in Geothermal Systems: Reviews in Mineralogy and Geochemistry, v. 65, p. 259–312, doi:10.2138/rmg.2007.65.9.

Banerjee, A. et al., 2011, Deep permeable fault-controlled helium transport and limited mantle flux in two extensional geothermal systems in the Great Basin, United States: Geology, v. 39, p. 195–198, doi:10.1130/G31557.1.

Beddows, P.A., and Mallon, E.K., 2018, Cave Pearl Data Logger: A Flexible Arduino-Based Logging Platform for Long-Term Monitoring in Harsh Environments: Sensors, v. 18, p. 530, doi:10.3390/s18020530.

Bégué, F., Deering, C.D., Gravley, D.M., Chambefort, I., and Kennedy, B.M., 2017, From source to surface: Tracking magmatic boron and chlorine input into the geothermal systems of the Taupo Volcanic Zone, New Zealand: Journal of Volcanology and Geothermal Research, v. 346, p. 141–150, doi:10.1016/j.jvolgeores.2017.03.008.

Bergfeld, D., Evans, W.C., McGee, K., and Spicer, K.R., 2008, Pre- and Post-Eruptive Investigations of Gas and Water Samples from Mount St. Helens, Washington, 2002 to 2005: A Volcano Rekindled: The Renewed Eruption of Mount St. Helens, 2004-2006., p. 523–542.

Bernal, N.F., Gleeson, S.A., Dean, A.S., Liu, X.-M., and Hoskin, P., 2014, The source of halogens in geothermal fluids from the Taupo Volcanic Zone, North Island, New Zealand: Geochimica et Cosmochimica Acta, v. 126, p. 265–283, doi:10.1016/j.gca.2013.11.003.

Bertrand, E.A. et al., 2012, Magnetotelluric imaging of upper-crustal convection plumes beneath the Taupo Volcanic Zone, New Zealand: Geophysical Research Letters, v. 39, p. n/a-n/a, doi:10.1029/2011GL050177.

Bibby, H.M., Caldwell, T.G., Davey, F.J., and Webb, T.H., 1995, Geophysical evidence on the structure of the Taupo Volcanic Zone and its hydrothermal circulation: Journal of Volcanology and Geothermal Research, v. 68, p. 29–58, doi:10.1016/0377-0273(95)00007-H.

Bloomberg, S., Werner, C., Rissmann, C., Mazot, A., Horton, T., Graveley, D., Kennedy, B., and Oze, C., 2014, Soil CO2 emissions as a proxy for heat and mass flow assessment, Taupo Volcanic Zone, New Zealand: Geochemistry, Geophysics, Geosystems: G3, v. 15, p. 4885–4904, doi:10.1002/2014GC005327.Received.

Bovolo, C.I., Parkin, G., and Sophocleous, M., 2009, Groundwater resources, climate and vulnerability: Environmental Research Letters, v. 4, p. 035001, doi:10.1088/1748-9326/4/3/035001.

Brahana, J.V., Hays, P.D., Kresse, T.M., Sauer, T.J., and Stanton, G.P., 1999, The Savoy Experimental Watershed–Early Lessons for Hydrogeologic Modeling From a Well-Characterized Karst Research Site, in Palmer, A.N., Palmer, M.V., and Sasowsky, I.D. eds.,

Karst Waters Institute Special Publication 5, Charles Town, WV, Karst Waters Institute, p. 247–254.

Burns, E.R., Williams, C.F., Ingebritsen, S.E., Voss, C.I., Spane, F.A., and DeAngelo, J., 2015, Understanding heat and groundwater flow through continental flood basalt provinces: insights gained from alternative models of permeability/depth relationships for the Columbia Plateau, USA: Geofluids, v. 15, p. 120–138, doi:10.1111/gfl.12095.

Burton, M.R., Sawyer, G.M., and Granieri, D., 2013, Deep Carbon Emissions from Volcanoes: Reviews in Mineralogy and Geochemistry, v. 75, p. 323–354, doi:10.2138/rmg.2013.75.11.

Campeau, A., Wallin, M.B., Giesler, R., Löfgren, S., Mörth, C.M., Schiff, S., Venkiteswaran, J.J., and Bishop, K., 2017, Multiple sources and sinks of dissolved inorganic carbon across Swedish streams, refocusing the lens of stable C isotopes: Scientific Reports, v. 7, p. 1–14, doi:10.1038/s41598-017-09049-9.

Cathles, L.M., and Schoell, M., 2007, Modeling CO2 generation, migration, and titration in sedimentary basins: Geofluids, v. 7, p. 441–450, doi:10.1111/j.1468-8123.2007.00198.x.

Charles, R.W., Buden, R.J.V., and Goff, F., 1986, An interpretation of the alteration assemblages at Sulphur Springs, Valles Caldera, New Mexico: Journal of Geophysical Research, v. 91, p. 1887, doi:10.1029/JB091iB02p01887.

Chiodini, G., Cardellini, C., Lamberti, M.C., Agusto, M., Caselli, A., Liccioli, C., Tamburello, G., Tassi, F., Vaselli, O., and Caliro, S., 2015, Carbon dioxide diffuse emission and thermal energy release from hydrothermal systems at Copahue-Caviahue Volcanic Complex (Argentina): Journal of Volcanology and Geothermal Research, v. 304, p. 294–303, doi:10.1016/j.jvolgeores.2015.09.007.

Chiodini, G., Granieri, D., Avino, R., Caliro, S., Costa, A., and Werner, C., 2005, Carbon dioxide diffuse degassing and estimation of heat release from volcanic and hydrothermal systems: Journal of Geophysical Research B: Solid Earth, v. 110, p. 1–17, doi:10.1029/2004JB003542.

Cressey, D., 2017, Toolbox: Age of the Arduino: Nature, v. 544, p. 125–126, doi:10.1038/544125a.

Crossey, L.J., Karlstrom, K.E., Springer, a. E., Newell, D., Hilton, D.R., and Fischer, T., 2009, Degassing of mantle-derived CO2 and He from springs in the southern Colorado Plateau region--Neotectonic connections and implications for groundwater systems: Geological Society of America Bulletin, v. 121, p. 1034–1053, doi:10.1130/B26394.1.

Cullen, J.T., Barnes, J.D., Hurwitz, S., and Leeman, W.P., 2015, Tracing chlorine sources of thermal and mineral springs along and across the Cascade Range using halogen concentrations and chlorine isotope compositions: Earth and Planetary Science Letters, v. 426, p. 225–234, doi:10.1016/j.epsl.2015.06.052.

Davidson, E.A., Figueiredo, R.O., Markewitz, D., and Aufdenkampe, A.K., 2010, Dissolved CO2 in small catchment streams of eastern Amazonia: A minor pathway of terrestrial carbon loss: Journal of Geophysical Research: Biogeosciences, v. 115, p. 1–6, doi:10.1029/2009JG001202.

Davis, S.N., Fabryka-Martin, ;, Wolfsberg, J.T.;, and Laura E, 2004, Variations of Bromide in Potable Ground Water in the United States: Ground Water, v. 42, p. 902–909, doi:10.1111/j.1745-6584.2004.t01-8-.x.

Davis, S.N., Whittemore, D.O., Fabryka-Martin, J., Fabryka-Martin, ;, Wolfsberg, J.T.;, and Laura E, 1998, Uses of Chloride/Bromide Ratios in Studies of Potable Water: Ground Water, v. 36, p. 338–350, doi:10.1111/j.1745-6584.1998.tb01099.x.

Dempsey, D.E., Simmons, S.F., Archer, R.A., and Rowland, J. V., 2012, Delineation of catchment zones of geothermal systems in large-scale rifted settings: Journal of Geophysical Research: Solid Earth, v. 117, p. 1–19, doi:10.1029/2012JB009515.

Duvert, C., Butman, D.E., Marx, A., Ribolzi, O., and Hutley, L.B., 2018, CO2 evasion along streams driven by groundwater inputs and geomorphic controls: Nature Geoscience, v. 11, p. 813–818, doi:10.1038/s41561-018-0245-y.

Elder, J.W., 1966, Heat and Mass Transfer in the Earth: Hydrothermal Systems: Wellington, New Zealand Department of Scientific and Industrial Research, v. 169, 115 p., https://catalogue.nla.gov.au/Record/1865431 (accessed June 2019).

Ellis, A.J., and Mahon, W.A.J., 1967, Natural hydrothermal systems and experimental hot water/rock interactions (Part II): Geochimica et Cosmochimica Acta, v. 31, p. 519–538, doi:10.1016/0016-7037(67)90032-4.

Evans, W.C., van Soest, M.C., Mariner, R.H., Hurwitz, S., Ingebritsen, S.E., Wicks, C.W., and Schmidt, M.E., 2004, Magmatic intrusion west of Three Sisters, central Oregon, USA: The perspective from spring geochemistry: Geology, v. 32, p. 69, doi:10.1130/G19974.1.

Evans, W.C., Sorey, M.L., Cook, A.C., Kennedy, B.M., Shuster, D.L., Colvard, E.M., White, L.D., and Huebner, M.A., 2002, Tracing and quantifying magmatic carbon discharge in cold groundwaters: lessons learned from Mammoth Mountain, USA: Journal of Volcanology and Geothermal Research, v. 114, p. 291–312, doi:10.1016/S0377-0273(01)00268-2.

Fan, Y., 2015, Groundwater in the Earth's critical zone: Relevance to large-scale patterns and processes: Water Resources Research, v. 51, p. 3052–3069, doi:10.1002/2015WR017037.

Fehn, U., and Snyder, G.T., 2003, Chapter 9 Origin of Iodine and 129 I in Volcanic and Geothermal Fluids from the North Island of New Zealand : Implications for Subduction Zone Processes: Society of Economic Geologists, v. 10, p. 159–170.

Forrest, M.J., Ledesma-Vázquez, J., Ussler, W., Kulongoski, J.T., Hilton, D.R., and Greene, H.G., 2005, Gas geochemistry of a shallow submarine hydrothermal vent associated with the El Requesón fault zone, Bahía Concepción, Baja California Sur, México: Chemical Geology, v. 224, p. 82–95, doi:10.1016/j.chemgeo.2005.07.015.

Fournier, R.O., Kennedy, B.M., Aoki, M., and Thompson, J.M., 1994, Correlation of gold in siliceous sinters with 3He/4He in hot spring waters of Yellowstone National Park: Geochimica et Cosmochimica Acta, v. 58, p. 5401–5419, doi:10.1016/0016-7037(94)90238-0.

Foustoukos, D.I., and Seyfried, W.E., 2007, Fluid Phase Separation Processes in Submarine Hydrothermal Systems: Reviews in Mineralogy and Geochemistry, v. 65, p. 213–239, doi:10.2138/rmg.2007.65.7.

Freeze, R.A., and Cherry, J.A., 1979, Groundwater: Upper Saddle River, NJ 07458, Prentice Hall.

Giggenbach, W.F., 1987, Redox processes governing the chemistry of fumarolic gas discharges from White Island, New Zealand: Applied Geochemistry, v. 2, p. 143–161, doi:10.1016/0883-2927(87)90030-8.

Giggenbach, W.F., 1995, Variations in the chemical and isotopic composition of fluids discharged from the Taupo Volcanic Zone, New Zealand: Journal of Volcanology and Geothermal Research, v. 68, p. 89–116, doi:10.1016/0377-0273(95)00009-J.

Giggenbach, W.F., Sheppard, D.S., Robinson, B.W., Stewart, M.K., and Lyon, G.L., 1994, Geochemical structure and position of the Waiotapu geothermal field, New Zealand\r[Monograph] Waimangu, Waiotapu, and Waikite geothermal systems, New Zealand: Geothermics, v. 23, p. 599–644.

Glover, R.B., and Mroczek, E.K., 2009, Chemical changes in natural features and well discharges in response to production at Wairakei, New Zealand: Geothermics, v. 38, p. 117–133, doi:10.1016/j.geothermics.2008.12.008.

Goff, F., Gardner, J., Vidale, R., and Charles, R., 1985, Geochemistry and isotopes of fluids from sulphur springs, Valles Caldera, New Mexico: Journal of Volcanology and Geothermal Research, v. 23, p. 273–297, doi:10.1016/0377-0273(85)90038-1.

Goff, F., and Janik, C.J., 2002, Gas geochemistry of the Valles caldera region, New Mexico and comparisons with gases at Yellowstone, Long Valley and other geothermal systems: Journal of Volcanology and Geothermal Research, v. 116, p. 299–323, doi:10.1016/S0377-0273(02)00222-6.

Goff, F., Shevenell, L., Gardner, J.N., Vuataz, F.-D., and Grigsby, C.O., 1988, The hydrothermal outflow plume of Valles Caldera, New Mexico, and a comparison with other outflow plumes: Journal of Geophysical Research, v. 93, p. 6041–6058, doi:10.1029/JB093iB06p06041.

Hanson, M.C., Oze, C., and Horton, T.W., 2014, Identifying blind geothermal systems with soil CO2 surveys: Applied Geochemistry, v. 50, p. 106–114, doi:10.1016/j.apgeochem.2014.08.009.

Hayba, D.O., and Ingebritsen, S.E., 1997, Multiphase groundwater flow near cooling plutons: Journal of Geophysical Research: Solid Earth, v. 102, p. 12235–12252, doi:10.1029/97jb00552.

Hedenquist, J.W., 1982, Fluid flow in the Waiotapu geothermal system, New Zealand: implications for its potential: New Zealand Geothermal Workshop, p. 61–67.

Hedenquist, J.W., Goff, F., Phillips, F.M., Elmore, D., and Stewart, M.K., 1990, Groundwater Dilution and Residence Times, and Constraints on Chloride Source, in the Mokai Geothermal System, New Zealand, From Chemical, Stable Isotope, Tritium, and 36 Cl

Data: Journal of Geophysical Research, v. 95, p. 19365–19375, doi:10.1029/JB095iB12p19365.

Hedenquist, J.W., and Lowenstern, J.B., 1994, The role of magmas in the formation of hydrothermal ore deposits: Nature, v. 370, p. 519–527, doi:10.1038/370519a0.

Hernández-Antonio, A., Mahlknecht, J., Tamez-Meléndez, C., Ramos-Leal, J., Ramírez-Orozco, A., Parra, R., Ornelas-Soto, N., and Eastoe, C.J., 2015, Groundwater flow processes and mixing in active volcanic systems: The case of Guadalajara (Mexico): Hydrology and Earth System Sciences, v. 19, p. 3937–3950, doi:10.5194/hess-19-3937-2015.

Hochstein, M.P., 1995, Crustal heat transfer in the Taupo Volcanic Zone (New Zealand): comparison with other volcanic arcs and explanatory heat source models: Journal of Volcanology and Geothermal Research, v. 68, p. 117–151, doi:10.1016/0377-0273(95)00010-R.

Horner, K.N., Short, M.A., and McPhail, D.C., 2017, Chloride and bromide sources in water: Quantitative model use and uncertainty: Journal of Hydrology, v. 549, p. 571–580, doi:10.1016/J.JHYDROL.2017.04.028.

Hurwitz, S., Lowenstern, J.B., and Heasler, H., 2007, Spatial and temporal geochemical trends in the hydrothermal system of Yellowstone National Park: Inferences from river solute fluxes: Journal of Volcanology and Geothermal Research, v. 162, p. 149–171, doi:10.1016/j.jvolgeores.2007.01.003.

Hurwitz, S., Mariner, R.H., Fehn, U., and Snyder, G.T., 2005, Systematics of halogen elements and their radioisotopes in thermal springs of the Cascade Range, Central Oregon, Western USA: Earth and Planetary Science Letters, v. 235, p. 700–714, doi:10.1016/j.epsl.2005.04.029.

Hut, R., Tyler, S., and Van Emmerik, T., 2016, Proof of concept: Temperature-sensing waders for environmental sciences: Geoscientific Instrumentation, Methods and Data Systems, v. 5, p. 45–51, doi:10.5194/gi-5-45-2016.

Ingebritsen, S.E. et al., 2013, Hydrothermal monitoring data from the Cascade Range, northwestern United States:, doi:10.5066/F72N5088.

Ingebritsen, S.E., Bergfeld, D., Clor, L.E., and Evans, W.C., 2016, The Lassen hydrothermal system: American Mineralogist, v. 101, p. 343–354, doi:10.2138/am-2016-5456.

Ingebritsen, S.E., Geiger, S., Hurwitz, S., and Driesner, T., 2010, Numerical simulation of magmatic hydrothermal systems: Reviews of Geophysics, v. 48, p. RG1002, doi:10.1029/2009RG000287.

Ingebritsen, S.E., and Sanford, W.E., 1999, Groundwater in Geologic Processes:, doi:10.2113/gseegeosci.15.1.48.

James, E.R., Manga, M., and Rose, T.P., 1999, CO2 degassing in the Oregon Cascades: Geology, v. 27, p. 823, doi:10.1130/0091-7613(1999)027<0823:CDITOC>2.3.CO;2.

Johnson, M.S., Billett, M.F., Dinsmore, K.J., Wallin, M., Dyson, K.E., and Jassal, R.S., 2009, Direct and continuous measurement of dissolved carbon dioxide in freshwater aquatic systems-method and applications: Ecohydrology, v. 3, p. n/a-n/a, doi:10.1002/eco.95.

Johnson, Hutnak, Dziak, Fox, Urcuyo, Cowen, Nabelek, and Fisher, 2000, Earthquake-induced changes in a hydrothermal system on the Juan de Fuca mid-ocean ridge: Nature, v. 407, p. 174–7, doi:10.1038/35025040.

Kelley, D.S., Robinson, P.T., and Malpas, J.G., 1992, Processes of brine generation and circulation in the oceanic crust: Fluid inclusion evidence from the Troodos Ophiolite, Cyprus: Journal of Geophysical Research, v. 97, p. 9307, doi:10.1029/92JB00520.

Kerrick, D.M., 2001, Present and past nonanthropogenic CO2 degassing from the solid earth: Reviews of Geophysics, v. 39, p. 565–585, doi:10.1029/2001RG000105.

Kerrick, D.M., and Caldeira, K., 1998, Metamorphic CO2 degassing from orogenic belts: Chemical Geology, v. 145, p. 213–232, doi:10.1016/S0009-2541(97)00144-7.

King, C.-Y., 1986, Gas geochemistry applied to earthquake prediction: An overview: Journal of Geophysical Research, v. 91, p. 122–169, doi:10.1029/JB091iB12p12269.

Kissling, W., Ellis, S., Charpentier, F., and Bibby, H., 2009, Convective Flows in a TVZ-like Setting with a Brittle/Ductile Transition: Transport in Porous Media, v. 77, p. 335–355, doi:10.1007/s11242-008-9328-3.

Kissling, W.M., and Weir, G.J., 2005, The spatial distribution of the geothermal fields in the Taupo Volcanic Zone, New Zealand: Journal of Volcanology and Geothermal Research, v. 145, p. 136–150, doi:10.1016/j.jvolgeores.2005.01.006.

Kresse, T.M., and Hays, P.D., 2009, Geochemistry, comparative analysis, and physical and chemical characteristics of the thermal waters east of Hot Springs National Park, Arkansas, 2006-09: U.S. Geological Survey Scientific Investigations Report 2009-5263:, doi:10.3133/sir20095263.

Kresse, T.M., Hays, P.D., Merriman, K.R., Gillip, J.A., Fugitt, D.T., Spellman, J.L., Nottmeier, A.M., Westerman, D.A., Blackstock, J.M., and Battreal, J.L., 2014, Aquifers of Arkansas-Protection, Management, and Hydrologic and Geochemical Characteristics of Groundwater Resources in Arkansas: U.S. Geological Survey Scientific Investigations Report 2014-5149:, doi:10.3133/sir20145149.

Lewicki, J.L., Bergfeld, D., Cardellini, C., Chiodini, G., Granieri, D., Varley, N., and Werner, C., 2005, Comparative soil CO2 flux measurements and geostatistical estimation methods on Masaya volcano, Nicaragua: Bulletin of Volcanology, v. 68, p. 76–90, doi:10.1007/s00445-005-0423-9.

Lewicki, J.L., and Oldenburg, C.M., 2005, Near-Surface CO2 Monitoring and Analysis To Detect Hidden Geothermal Systems, in Thirtieth Workshop on Geothermal Reservoir Engineering, Stanford University, Stanford, California, January 31-February 2, p. 8.

Liu, F., Bales, R.C., Conklin, M.H., and Conrad, M.E., 2008, Streamflow generation from snowmelt in semi-arid, seasonally snow-covered, forested catchments, Valles Caldera, New Mexico: Water Resources Research, v. 44, p. 1–13, doi:10.1029/2007WR006728.

Lowell, R.P., 1975, Circulation in Fractures, Hot Springs, and Convective Heat Transport on Mid-ocean Ridge Crests: Geophysical Journal International, v. 40, p. 351–365, doi:10.1111/j.1365-246X.1975.tb04137.x.

Lowenstern, J.B., Bergfeld, D., Evans, W.C., and Hunt, A.G., 2015, Origins of geothermal gases at Yellowstone: Journal of Volcanology and Geothermal Research, v. 302, p. 87–101, doi:10.1016/j.jvolgeores.2015.06.010.

Lowenstern, J.B., Bergfeld, D., Evans, W.C., and Hurwitz, S., 2012, Generation and evolution of hydrothermal fluids at Yellowstone: Insights from the Heart Lake Geyser Basin: Geochemistry, Geophysics, Geosystems, v. 13, p. 1–20, doi:10.1029/2011GC003835.

Lowenstern, J.B., Evans, W.C., Bergfeld, D., and Hunt, A.G., 2014, Prodigious degassing of a billion years of accumulated radiogenic helium at Yellowstone.: Nature, v. 506, p. 355–8, doi:10.1038/nature12992.

Lowenstern, J.B., and Hurwitz, S., 2008, Monitoring a Supervolcano in Repose: Heat and Volatile Flux at the Yellowstone Caldera: Elements, v. 4, p. 35–40, doi:10.2113/GSELEMENTS.4.1.35.

Lupton, J. et al., 2006, Submarine venting of liquid carbon dioxide on a Mariana Arc volcano: Geochemistry, Geophysics, Geosystems, v. 7, doi:10.1029/2005GC001152.

Martini, M., 1996, Chemical Characters of the Gaseous Phase in Different Stages of Volcanism: Precursos and Volcanic Activity, in Scarpa, R. and Tilling, R. eds., Monitoring and mitigation of volcano hazards, Berlin, Heidelberg, Springer, p. 199–219, doi:10.1007/978-3-642-80087-0.

Millot, R., Hegan, A., and Négrel, P., 2012, Geothermal waters from the Taupo Volcanic Zone, New Zealand: Li, B and Sr isotopes characterization: Applied Geochemistry, v. 27, p. 677–688, doi:10.1016/j.apgeochem.2011.12.015.

Parnell, A.C., Inger, R., Bearhop, S., and Jackson, A.L., 2010, Source partitioning using stable isotopes: coping with too much variation.: PloS one, v. 5, p. e9672, doi:10.1371/journal.pone.0009672.

Pearce, J.M., 2012, Building Research Equipment with Free, Open-Source Hardware: Science, v. 337, p. 1303–1304, doi:10.1126/science.1228183.

Phillips, D.L., and Gregg, J.W., 2001, Uncertainty in source partitioning using stable isotopes: Oecologia, v. 127, p. 171–179, doi:10.1007/s004420000578.

Phillips, D.L., and Koch, P.L., 2002, Incorporating concentration dependence in stable isotope mixing models: Oecologia, v. 130, p. 114–125.

Ratouis, T.M.P., and Zarrouk, S.J., 2016, Factors controlling large-scale hydrodynamic convection in the Taupo Volcanic Zone (TVZ), New Zealand: Geothermics, v. 59, p. 236–251, doi:10.1016/J.GEOTHERMICS.2015.09.003.

Reyes, A.G., and Trompetter, W.J., 2012, Hydrothermal water–rock interaction and the redistribution of Li, B and Cl in the Taupo Volcanic Zone, New Zealand: Chemical Geology, v. 314–317, p. 96–112, doi:10.1016/j.chemgeo.2012.05.002.

Rogie, J.D., Kerrick, D.M., Sorey, M.L., Chiodini, G., and Galloway, D.L., 2001, Dynamics of carbon dioxide emission at Mammoth Mountain, California: Earth and Planetary Science Letters, v. 188, p. 535–541, doi:10.1016/S0012-821X(01)00344-2.

Saar, M.O., 2011, Review: Geothermal heat as a tracer of large-scale groundwater flow and as a means to determine permeability fields: Hydrogeology Journal, v. 19, p. 31–52, doi:10.1007/s10040-010-0657-2.

Schütze, C., Sauer, U., Beyer, K., Lamert, H., Bräuer, K., Strauch, G., Flechsig, C., Kämpf, H., and Dietrich, P., 2012, Natural analogues: A potential approach for developing reliable monitoring methods to understand subsurface CO2 migration processes: Environmental Earth Sciences, v. 67, p. 411–423, doi:10.1007/s12665-012-1701-4.

Scott, S., Driesner, T., and Weis, P., 2015, Geologic controls on supercritical geothermal resources above magmatic intrusions.: Nature communications, v. 6, p. 7837, doi:10.1038/ncomms8837.

Simmons, S.F., and Brown, K.L., 2006, Gold in Magmatic Hydrothermal Solutions and the Rapid Formation of a Giant Ore Deposit: Science, v. 314, p. 288–291, doi:10.1126/science.1132866.

Stefánsson, A., Sveinbjörnsdóttir, Á.E., Heinemeier, J., Arnórsson, S., Kjartansdóttir, R., and Kristmannsdóttir, H., 2016, Mantle CO2 degassing through the Icelandic crust: Evidence from carbon isotopes in groundwater: Geochimica et Cosmochimica Acta, v. 191, p. 300–319, doi:10.1016/j.gca.2016.06.038.

Stewart, M.K., 2012, A 40-year record of carbon-14 and tritium in the Christchurch groundwater system, New Zealand: Dating of young samples with carbon-14: Journal of Hydrology, v. 430–431, p. 50–68, doi:10.1016/j.jhydrol.2012.01.046.

Svensen, H., Hammer, Ø., Mazzini, A., Onderdonk, N., Polteau, S., Planke, S., and Podladchikov, Y.Y., 2009, Dynamics of hydrothermal seeps from the Salton Sea geothermal system (California, USA) constrained by temperature monitoring and time series analysis: Journal of Geophysical Research, v. 114, p. B09201, doi:10.1029/2008JB006247.

Szynkiewicz, A., Goff, F., Vaniman, D., and Pribil, M.J., 2019, Sulfur cycle in the Valles Caldera volcanic complex, New Mexico – Letter 1: Sulfate sources in aqueous system, and implications for S isotope record in Gale Crater on Mars: Earth and Planetary Science Letters, v. 506, p. 540–551, doi:10.1016/j.epsl.2018.10.036.

Thomas, D.L., Bird, D.K., Arnórsson, S., and Maher, K., 2016, Geochemistry of CO2-rich waters in Iceland: Chemical Geology, v. 444, p. 158–179, doi:10.1016/j.chemgeo.2016.09.002.

Tóth, J., 1999, Groundwater as a geologic agent: An overview of the causes, processes, and manifestations: Hydrogeology Journal, v. 7, p. 1–14, doi:10.1007/s100400050176.

Truesdell, A.H., Haizlip, J.R., Armannsson, H., and D'Amore, F., 1989, Origin and transport of chloride in superheated geothermal steam: Geothermics, v. 18, p. 295–304, doi:10.1016/0375-6505(89)90039-4.

Truesdell, A.H., and Janik, C.J., 1986, Reservoir processes and fluid origins in the Baca Geothermal System, Valles Caldera, New Mexico: Journal of Geophysical Research, v. 91, p. 1817–1833, doi:10.1029/JB091iB02p01817.

Truesdell, A.H., Nathenson, M., and Rye, R.O., 1977, The effects of subsurface boiling and dilution on the isotopic compositions of Yellowstone thermal waters: Journal of Geophysical Research, v. 82, p. 3694–3704, doi:10.1029/JB082i026p03694.

Truesdell, A.H., Thompson, J.M., Coplen, T.B., Nehring, N.L., and Janik, C.J., 1981, The origin of the Cerro Prieto geothermal brine: Geothermics, v. 10, p. 225–238, doi:10.1016/0375-6505(81)90006-7.

Umeda, K., Ninomiya, A., and Negi, T., 2009, Heat source for an amagmatic hydrothermal system, Noto Peninsula, Central Japan: Journal of Geophysical Research: Solid Earth, v. 114, p. 1–10, doi:10.1029/2008JB005812.

Waite, G.P., 2002, Seismic evidence for fluid migration accompanying subsidence of the Yellowstone caldera: Journal of Geophysical Research, v. 107, p. 2177, doi:10.1029/2001JB000586.

Werner, C., Brantley, S.L., and Boomer, K., 2000, CO 2 emissions related to the Yellowstone volcanic system: 2. Statistical sampling, total degassing, and transport mechanisms: Journal of Geophysical Research: Solid Earth, v. 105, p. 10831–10846, doi:10.1029/1999JB900331.

You, C.F., Gieskes, J.M., Lee, T., Yui, T.F., and Chen, H.W., 2004, Geochemistry of mud volcano fluids in the Taiwan accretionary prism: Applied Geochemistry, v. 19, p. 695–707, doi:10.1016/j.apgeochem.2003.10.004.

Chapter 2: Br-Cl mixing relations in the Taupo Volcanic Zone, New Zealand: Insights and open questions

This chapter is composed of the publication:

Blackstock, J.M., Hays, P.D., Horton, T.W., Brown, K.L., in preparation, Br-Cl mixing relations in the Taupo Volcanic Zone, New Zealand: Insights and open questions: Journal of Hydrology

Abstract

Tracing fluids in hydrothermal systems provides critical information to underlying factors controlling fluid flow paths and groundwater evolution. Assessment of groundwater mixing is paramount to further understanding these factors and their effects on hydrothermal ore-genesis, volcanogenic hazards, and planetary geochemical cycles. However, knowledge on the degree of mixing between hydrothermal fluids and non-thermal waters near Earth's surface remains difficult to constrain, particularly at low temperatures. In the Taupo Volcanic Zone (TVZ), New Zealand, inventory of the occurrence and distribution of hydrothermal waters is abundant; however, application of end-member mixing is limited. Exploratory analysis of newly collected and previously available Cl-Br and Cl-δ^2H data among non-thermal groundwater, hydrothermal surface discharge (e.g. hot springs, hot pools), and hydrothermal wells were used to develop simple end-member mixing models at selected geothermal areas in the TVZ. To determine low-temperature end-member values, the study developed statistically significant empirical spatial relations between Cl-Br ratio ($r^2 = 0.80$, $p <<< 0.05$) and Cl concentrations ($r^2 = 0.76$, $p <<< 0.05$) with distance from the North Island coastline, which allowed estimation of non-thermal Cl-Br end-members. Calculated mixing ratios for hydrothermal surface discharge values exhibited a

wide range of dilution amounts from less than 10 % to over 50 % of respective hydrothermal well end-members. Notably, hydrothermal surface discharge Cl/Br ratios and concentrations were typically between end-member ratios within respective geothermal areas. Excluding significant Cl/Br fractionation from phase-separation, hydrothermal surface features having elevated Cl concentrations (i.e. greater than low-temperature groundwater) but intermediate Cl/Br ratios were interpreted to be resultant from recirculation of groundwater in the hydrothermal system. While the extent of recirculation remains enigmatic, it is postulated that recirculation is likely pervasive in liquid-dominated hydrothermal systems. A conceptual model of Cl-Br and Cl-δ^2H evolution was developed to provide broader interpretation of groundwater flow paths and groundwater mixing related to recirculation.

Introduction

Heat and mass fluxes associated with hydrothermal groundwater circulation within the lithosphere have profound impacts on the physical and chemical evolution of Earth's crust and related components of Earth's hydrosphere and atmosphere (Ague, 2014). Hydrothermal circulation facilitates a number of hydromechanical and hydrochemically coupled processes linked with ore-deposits (Hedenquist and Lowenstern, 1994; Simmons and Brown, 2006, 2007), greenhouse-gas emissions (Gerlach et al., 1997; Mörner and Etiope, 2002; Chiodini et al., 2005; Svensen et al., 2009; Burton et al., 2013), geologic hazards (Lowenstern and Hurwitz, 2008; Liuzzo et al., 2013; Hurwitz and Lowenstern, 2014; Caracausi et al., 2015), and renewable energy sources (Williams et al., 2008; Sanyal, 2010; Moore and Simmons, 2013; Scott et al., 2015). Despite their importance, detailed characterization of hydrothermal fluid-flow paths and mixing with shallow, low-temperature groundwater remain difficult to constrain (Ingebritsen et al., 1989; Martini, 1996; Goff and Janik, 2002; Fehn and Snyder, 2003; Caracausi et al., 2005; Marini and Gambardella, 2005; Lowenstern et al., 2014).

The highly soluble and nonreactive, or 'conservative', nature of Cl and Br render these elements useful tracers in many complex geologic environments, regardless of their solute origin (Davis et al., 1998; Vengosh and Pankratov, 1998; Villemant and Boudon, 1999; Freeman, 2007; Horner et al., 2017) (Davis et al., 1998; Hurwitz et al., 2005; Reyes and Trompetter, 2012). In hydrothermal systems, this conservative behavior, along with common formation of Cl and Br complexes facilitates dissolution and transport of economic metal ions (Cole and Drummond, 1986; Krupp and Seward, 1987; Goff and Gardner, 1994; Fournier et al., 1994; Simmons and Brown, 2007; Blamey, 2012; Nadeau et al., 2016) critical to the genesis of large epithermal ore-deposits. Therefore, by understanding the evolution of Cl and Br chemistry in hydrothermal

groundwater systems, furthers understanding of geologic processes involving Cl-rich fluids (Evans et al., 2004; Ingebritsen et al., 2013).

Application of paired Cl and Br to develop mixing relations in terrestrial, liquid-dominated hydrothermal systems has been limited compared to other Cl pairs, such as Cl-B, Cl-δ^2H, or Cl-HCO_3 (Fehn and Snyder, 2003; Hurwitz et al., 2005; Bernal et al., 2014). Moreover, previous studies that have reported on the variation of Br and Cl among hydrothermal wells and hydrothermal surface discharge were most concerned with the origins of Br and Cl (Millot et al., 2012; Bernal et al., 2014). In the TVZ, no previous research has implemented a Cl and Br mixing model approach to assess mixing relations between non-thermal waters and ascending hydrothermal fluids. However, if abundant hydrochemical data are available for non-thermal waters, hydrothermal surface discharge, and hydrothermal wells from the last half century, development and application of end-member mixing analysis (EMMA) should be possible within the TVZ to estimate groundwater mixing ratios.

This study uses both new analyses and compiled Cl, Br, and water isotope (δ^2H and δ^{18}O) data from recent sampling, publicly available data repositories, and published sources and examined Cl-Br and δ^2H-Cl relations and mixing ratios among low-temperature groundwater, hydrothermal surface discharge, and hydrothermal wells. As part of defining end-members for EMMA in the TVZ, estimation of Cl-Br concentrations and Cl/Br ratios was developed using empirical analysis of spatial distributions of non-thermal groundwater sites. Variability of Cl and Br compositions, δ^2H-Cl relations, and calculated mixing ratios presented provide dilution trends in TVZ hydrothermal systems. Combination of these findings with a global survey of available numerical modeling and geophysical observations within geothermal areas resulted in

development of a conceptual model of groundwater flow paths and Cl-Br and δ^2H-Cl evolution for liquid-dominated magmatic geothermal systems, such as the TVZ.

Research Questions and Hypotheses

The primary objective of this study sought to investigate three main research questions and associated empirical hypotheses related to the development, application, and implications of Cl-Br mixing models in TVZ.

Research Question I

Where low-temperature data are scant, could Cl/Br ratios and Cl and Br concentrations be predicted using empirical models?

Hypothesis I

Based on previous analysis that demonstrated decreasing of Cl/Br ratios and Cl-Br concentrations with distance from coastlines (Davis et al., 2004; Short et al., 2017), if low-temperature groundwater are not available, Cl and Br concentrations can be empirically modeled based spatial location from the North Island, New Zealand coastline.

Research Question II

From available measurements of dissolved Cl and Br for low-temperature and high-temperature groundwater in the TVZ, are end-member compositions between low- and high-temperature groundwater distinguishable? Is EMMA a viable method to ascertain dilution trends and mixing ratios between end-members? Moreover, do calculated mixing trends present in the TVZ hydrothermal systems corroborate with a conservative assumption of Cl and Br behavior for high-temperature groundwater?

Hypothesis II

Among low- and high-temperature groundwater measurements, concentrations of Cl and Br will be greater in high-temperature groundwaters systems, even if Cl-Br ratios are similar. Furthermore, hydrothermal surface discharge concentrations should be between low-temperature and high-temperature groundwater. If boiling is present, concentrations may be similar to hydrothermal well concentrations and will evident from higher δ^2H values relative to low-temperature groundwater. If one to one mixing is present between low- and high-temperature groundwater end-members in the TVZ hydrothermal systems, hydrothermal surface discharge values should plot along or near modeled mixing curves.

Research Question III

At deeper depths in the TVZ hydrothermal system, contributions from magmatic degassing and water-rock interaction may imbue changes to Cl-Br and δ^2H-Cl relations, but conceptually, what are physical flow paths and locations of these changes in hydrothermal systems? Moreover, what are the possible end-member values that could be expected, if data were available?

Hypothesis III

Based on ancillary data from an extensive survey of observed and predicted trends in Cl-Br and δ^2H-Cl compositions, development of a generalized conceptual model of flow paths and correspondent changes in chemical compositions should be possible. In turn, this model would not only be representative of the TVZ, but other high-temperature, liquid dominated hydrothermal systems, globally (e.g. Norris Geyser Basin, Yellowstone, USA).

Background

Moisture sources for groundwater systems

Moisture for groundwater recharge to the geothermal areas of the Taupo Volcanic Zone, North Island, New Zealand is dominated by westerly circulation comprising anticyclones and troughs (Salinger and Salinger, 1980; Lorrey et al., 2008). Precipitation patterns across New Zealand are highly localized and affected by orographic effects, distance from coastlines, and intensity of prevailing westerlies (Watts, 1947; Garnier and 1917-, 1950; Lorrey et al., 2008; Dravitzki and McGregor, 2011). However, of the total rainfall amounts across the TVZ, only 2 percent is needed to account for geothermal groundwater circulation (Kissling and Weir, 2005).

Investigation of the spatial distributions of Cl and Br in rainfall and groundwater is particularly interesting as studies have noted that coastal areas and continental settings exhibit distinct differences in Cl and Br concentrations (Davis et al., 2004). Near the coast, Br and Cl compositions generally plot on or near the seawater ratio of 660 (Short et al., 2017). Slightly lower ratios of Cl/Br in precipitation and groundwater compared to seawater results from the chemical fractionation associated with the formation of sea salts (i.e. aerosols), bubble bursting at the ocean surface due to wave action, and rainout (Bloch et al., 1966; Blanchard and Syzdek, 1972; Wetherbee et al., 2018).

As larger aerosols are preferentially rained out first in air masses due to gravitational forces, sites on land further from the coast tend to exhibit lower Cl/Br ratios (Zhou et al., 1990; Virkkula et al., 1999). This stems from higher polarizability of Br resultant from the combination of: 1, the larger anion size of Br whereby covalent bonding is favored due to easier cation distortion of outer Br electrons; and 2, smaller aerosols typically contain smaller cations which

having an increased charge per surface area ratio, which more readily covalently bond with Br (Fajans, 1923; Davis et al., 1998; Pavel Jungwirth† and Douglas J. Tobias*, 2001). Therefore, sites inland from the North Island coastline are likely to exhibit a decrease in Cl/Br ratios. Further variation of Cl and Br concentrations and ratios may occur in the vadose zone due to evapotranspiration and halite precipitation (Horner et al., 2017), but are more pronounced in more arid climatic conditions not characteristic of the North Island except for the central portions of the North Island.

The Taupo Volcanic Zone

The Taupo Volcanic Zone is an actively rifting arc (up to 15 mm/yr) that spans approximately 250 km from Whakaari/White Island volcano in the north to Ruapehu in the south (Figure 2) (Wilson et al., 1995; Darby et al., 2000). The central portion of the TVZ is predominately composed of several large calderas and represents the most active silicic-volcanism on Earth for the past 340,000 years (Wilson et al., 1995) while the northern and southern margins of the TVZ are dominated by typical arc-andesitic volcanism (Houghton et al., 1995).

Elevated heat flow in the underlying TVZ results in a shallow brittle-ductile transition depth (Bibby et al., 1995; Hochstein, 1995) and interpreted partial melt at approximately 7 to 8 km (Bertrand et al., 2012). With abundant groundwater recharge (Kissling and Weir, 2005) and high-heat flow at depth, over 20 major geothermal fields have been delineated from shallow, low-resistivity surveys (Bibby et al., 1995). Combined heat flow from conductive and convective heat transfer in the TVZ is estimated to be ~ 4,500 MW (Bibby et al., 1995; Rowland and Sibson, 2004).

Hydrothermal circulation in the TVZ

Circulating groundwater in the TVZ systems is estimated to travel to the zone of estimated partial melt at approximately 7 to 8 km depth (Bannister et al., 2007; Heise et al., 2010; Bertrand et al., 2012), which is inferred to coincide with the brittle-ductile transition. While meteoric water incursion in to ductile regions of the crust have been reported (Menzies et al., 2014, 2016), groundwater circulation important for development of hydrothermal reservoirs, ore-genesis, and discharge of hydrothermal fluids at the surface is primarily related to groundwater circulation above the brittle-ductile transition and is the main focus of this study (Ingebritsen et al., 2010; Weis et al., 2014).

Remarkably, while hydrothermal systems exist in a wide variety of tectonic settings and host rock lithologies, a common hydrochemical composition and fluid evolution has been noted globally (Arnorsson et al., 2007) and observed to be present in the TVZ (Lyon and Hulston, 1984; Giggenbach et al., 1994; Giggenbach, 1995). From the base of the hydrothermal convection cell (i.e. at or near the heat source), an acidic, high salinity, gas-rich hydrothermal fluids migrate upwards in the TVZ through permeable zones associated with faulting and fracturing (Bibby et al., 1995; Caine et al., 1996; Rowland and Sibson, 2004; Ratouis and Zarrouk, 2016). As hydrothermal groundwater ascends, fluids adiabatically boil and become a two-phase solutions. Moreover, interactions with host-rocks and exsolution of gases yield a slightly more diluted, NaCl-rich, neutral-pH fluid (i.e. neutral-chloride). Hydrothermal reservoirs throughout the TVZ are primarily neutral-chloride groundwater with varying gas contents.

Ascending fluids from hydrothermal reservoirs continue to migrate along permeable networks and mix with convecting non-thermal groundwater becoming more diluted, in most cases (Truesdell et al., 1977; Arnórsson and Andrésdóttir, 1995; Giggenbach, 1995; Martini,

1996; Arnorsson et al., 2007). While several studies in the TVZ have characterized hydrothermal fluid dilution using dissolved species like Cl, B, and Li, use of Cl and Br may allow for more accurate quantification of hydrothermal dilution at smaller mixing ratios whereas B and Li are removed from solution by low-temperature water-rock interactions, inhibiting their use in mixing ratio calculations at low-temperatures.

Materials and methods

Data collection, analysis, and data sources

Compiled data for non-thermal groundwater, hydrothermal surface discharge, and hydrothermal wells were drawn from samples collected as part of the Waikato Regional Council Regional Geothermal Geochemistry Monitoring Programme (REGEMP) data repository (Golder Associates, 2013 and references therein), the GNS Science Geothermal and Groundwater Database (Moreau-Fournier et al., 2010), and assimilated from previously published values (Hedenquist et al., 1990; Daughney and Randall, 2009; Millot et al., 2012; Bernal et al., 2014). In this study, geothermal-energy production wells and non-producing, but geothermal wells where high-temperature groundwater was collected are collectively referred to as hydrothermal wells. Water samples collected in 2013 and 2018 as part of the REGEMP sampling campaigns were analyzed for water stable isotope compositions at the University of Canterbury Stable Isotope Facility in 2013 and University of Arkansas Stable Isotopic Laboratory in 2018. In both cases, analytical determination of δ^2H and $\delta^{18}O$ were similarly done using a Thermo Scientific TC/EA (Thermo-Combustion Elemental Analyser). Analyses were conducted using similar methods outlined in (Sharp et al. 2001) whereby samples are converted to $H_2(g)$ and CO(g) at 1400ºC in a ultra-high purity helium stream. This mixed gas is then separated into discrete

phases by a 5Aºmol sieve gas chromatography column. Sample gas was introduced to a Delta V Plus IRMS through a CONFLOIII split. δ-values were obtained from the integration of peaks recorded by the mass spectrometer and referenced to two IAEA standards (V-SMOW and SLAP) using a two-point calibration (Coplen, 1996).

In total, this study compiled 1,058 analyses of thermal (> 20° C) and non-thermal surface water and groundwater analyses within the TVZ. As an initial screening, this study included only those analyses that measured dissolved Cl concentration. Measurements that included paired δ^2H-Cl and Cl-Br values were less in total number. Geothermal areas where EMMA was applied required at least one measured value for Cl and Br in one hydrothermal well and one HS feature.

Measured water temperatures for surface water and groundwater above 20 °C were considered hydrothermally influenced. This temperature was selected based on early analysis indicating a larger range in Cl values above approximately 20° C (Figure 3). As mean annual temperature over much of the TVZ are approximately 14 °C, categorization of data as non-thermal up to 20° C allows some account for seasonally warmer surface waters and groundwater recharge.

Modeling spatial distribution of Cl and Cl/Br ratio of non-thermal groundwater and water isotope values

Cl and Br data from non-thermal groundwater wells were not available for low-temperature end-members at the eight geothermal fields selected for EMMA. In turn, Cl concentrations and Cl/Br ratios were estimated using empirical relations determined from the relation between the distances of geothermal fields from the North Island coastline and available Cl concentration and Cl/Br ratio data at groundwater sites dispersed in throughout the TVZ.

Low-temperature groundwater data used to derive the empirical relations were median values from the New Zealand National Groundwater trends database (Daughney and Randall, 2009). These median values are derived from groundwater samples collected from 1985 to 2010 and are assumed to be representative of: 1, Cl-Br composition of downward migrating, low-temperature groundwater for respective hydrothermal convection cells between geothermal areas; and 2, Cl-Br composition of mixing with high-temperature groundwater near the surface.

Seasonal differences of Cl-Br and influence from land use-land cover may deviate from long-term, low-temperature groundwater values (Davis et al., 1998; Katz et al., 2011). Considering the typical two to three orders of magnitude difference in concentration between low- and high-temperature groundwater concentrations, seasonal or land use-land cover variability is therefore increasingly important for hydrothermal surface discharge with lesser amounts of the hydrothermal groundwater end-member. While not directly assessed, uncertainties stemming from empirical spatial analyses including in EMMA are likely to capture some component of natural Cl-Br variability, but is an open question.

Distances from the North Island coastline were determined using ESRI (Redlands, CA) ArcMap GIS software platform. Inward buffer polylines were generated at 0.1, 1, 10, 20, and additional increments of 10 km from the coast up to 110 km and were interpolated using the *Topo to Raster* function (Figure 4). This generated a continuous raster image of distances from the surrounding coastline at ~ 800 m resolution.

Geothermal field association and individual hydrothermal feature associations

Not all hydrothermal surface features in the TVZ lie within previously defined geothermal area boundaries determined by Bibby et al. (1995). In this study, association

hydrothermal features to geothermal areas was done by incorporating the geothermal catchment (or recharge) areas generated by Dempsey et al. (2012). Specifically, spatially located features were associated with geothermal areas based on overlap of the hydrothermal feature point and catchment polygons. As two catchment polygon areas were generated by Dempsey et al. (2012) using two heat flow models (Figure 5), associations were also compared to determine if hydrothermal surface discharge features and non-thermal groundwater sites were shared between overlapping modeled catchments areas. No features were observed to be shared given the sites used.

In collating data, identification and association of hydrothermal wells, hydrothermal surface discharge, and non-thermal groundwater sites between the assimilated datasets was problematic. Specifically, site identification schemes (i.e. site name or site/spring/well number) and spatial references, if provided, were often inconsistent in nomenclature, location datums, and spatial accuracy. In turn, assessment of long-term variability for individual hydrothermal features has been excluded at this time. However, previous investigation of chemical variability in hydrothermal wells from the TVZ found Cl concentrations to be more stable and hydrothermal surface features to be more variable (Pope et al., 2004; Pope and Brown, 2014). While some Cl/Br ratio variability may also result from analytical uncertainty, the magnitude of this uncertainty is not well understood (Bernal et al., 2014).

Hydrothermal surface discharge concentration variability originates primarily from variable mixing between the low- and high-temperature groundwater near the surface. Mixing arises from there being increased permeability near the surface and incursion of low-temperature groundwater into hydrothermal plumes (Arnórsson and Andrésdóttir, 1995; Lowenstern and Hurwitz, 2008; Kresse and Hays, 2009; Ingebritsen et al., 2013; Scott et al., 2015). The degree of

mixing between low- and high-temperature end-members typically varies between individual discharge locations and is dependent upon localized hydraulic gradients, flow paths, and permeability near discharge locations (Kresse and Hays, 2009). Even though the variability of mixing is unknown for individual features, observation of whether hydrothermal surface discharge values plot along or near predicted mixing curves provides critical evidence if groundwater mixing is occurring between low- and high-temperature end-members.

End-member mixing analysis

To assess relative mixtures between hydrothermal wells (HW) and non-thermal groundwater (LGW), a simple, two-endmember linear mixing model, modified from Phillips and Gregg (2001) was adopted. Following a mass-balance approach where X_m equals the mixture concentration (presented here as molality), mixing curves were generated for Cl and Br from the following equations:

$$X_m = fX_{LGW} + fX_{HW} \quad (1)$$

$$1 = f_{LGW} + f_{HW} \quad (2)$$

where X_{HW} equals the concentration of the hydrothermal well component, f_{HW} equals the fraction of the hydrothermal well component in the mixture, X_{LGW} equals the concentration of low-temperature groundwater, and f_{LGW} equals the fraction of low-temperature groundwater. Where multiple hydrothermal well values existed for a geothermal area, the Euclidean, or geometric median (Lewis, 2010), among Cl and Br values was used to estimate the end-member value:

$$S_{error} = \sum_{i=1}^{n} \sqrt{(X_i - X_M)^2 + (Y_i - Y_M)^2} \quad (3)$$

where estimated median values for Cl, X_M, and Br, Y_M, were incrementally adjusted using EXCEL Solver (Microsoft, Redmond, WA, USA) as to minimize S_{error}. Reduction of S_{error} was calculated using a least-sum-square error procedure and Generalized Reduced Gradient method (Gadagkar and Call, 2015). While not ideal, for sites having only one hydrothermal well Cl-Br paired measurement, these value was used as the end-member value.

Evidence for boiling, dilution, and Cl-Br interactions

If a large fraction of ascending water is boiled, a corresponding shift in δ^2H will yield higher values in the residual liquid (Truesdell et al., 1977). Furthermore, concentrations of Cl and Br will also increase in the residual liquid if boiling is present (Truesdell et al., 1977, 1981; Lowenstern et al., 2012), but whether Cl/Br partitioning is 1:1 during phases separation is debated (Lüders et al., 2002; Rodríguez et al., 2016). Other factors that may also affect dissolved Br and Cl concentrations include the presence of halite or other Cl-rich minerals (e.g. sylvite), loss of Cl due to mineralization, or from Br loss by adsorption to organics (Fuge, 1988; Davis et al., 1998; Horner et al., 2017). However, halite saturation and deposition is relatively rare near the surface in terrestrial, liquid-dominated hydrothermal environments, and in general, where active fluid circulation is present. However, halide fronts may be present at depth during the lifespan of a geothermal system in deeper, hyper saline portions of the hydrothermal reservoir (Truesdell et al., 1981; Weis et al., 2014; Weis, 2015).

Data analysis

Descriptive statistics and assessment of relations observed in this study were carried out using multiple correlation and regression analyses using PAST, version 3.25 (Hammer et al., 2001). Sample distributions among low- and high-temperature groundwater and hydrothermal

surface discharge for both concentrations and ratios were represented using box and whisker plots, which included kernel density distributions (or continuous histograms), and individual data points. Determination of bivariate relations were assessed using linear regression models and associated correlation statistics, which included the analysis of residuals using the Durbin-Watson and Breusch-Pagan tests for autocorrelation and homoskedasticity, respectively.

Results

Variability of Cl and Br across the Taupo Volcanic Zone

Br and Cl compositions measured for non-thermal and thermal waters across the TVZ exhibit a range of concentrations covering four orders of magnitude (Figure 6). Using a logarithmic transformation, values of log micromoles Br/kg and millimoles Cl/kg exhibit significant linear covariation ($r^2 = 0.94$, $p <<< 0.05$). From general assessment, the lowest concentrations are observed for low-temperature groundwater with markedly greater concentrations among hydrothermal surface discharge and hydrothermal wells. At concentrations less than 0.5 millimoles Cl/kg for low-temperature groundwater, Br concentrations deviated from linear covariation and ranged over an order of magnitude (0.1 to 5.6 micromoles Br/kg).

Distributions and medians of Cl concentrations and Cl/Br ratios markedly increased from low-temperature groundwater to hydrothermal surface features to hydrothermal wells (Figure 7). Comparatively, median Cl concentrations were 0.21, 9.8, and 40.9 millimoles Cl/kg among low-temperature groundwater, hydrothermal surface discharge, and hydrothermal well, respectively. Ratios of Cl/Br were 823, 815, and 884 among low-temperature groundwater, hydrothermal surface discharge, and hydrothermal wells, respectively. Important to general application of EMMA, Cl/Br ratios may be similar, but concentrations among the three sample types varied by

orders of magnitude. Kernel density distributions of Cl concentrations among site types exhibit bimodal distributions. However, kernel density distributions of Cl/Br ratios among site types exhibited unimodal distributions. While having the lowest Cl concentrations, low-temperature groundwater exhibited the greatest range in Cl/Br ratios.

Empirical modeling of low-temperature groundwater Cl and Cl/Br values

From north to south in the TVZ, Cl concentrations and Cl/Br ratios decrease progressively inland from the coast (Figure 8A-B) with significant linear covariation and correlation observed between: 1, log10 of Cl concentrations, millimoles Cl/kg and log10 of distance from the coastline, km ($r^2 = 0.76$, $p <<< 0.05$); and 2, square root of Cl/Br ratios versus square root of distance from the coastline, km ($r^2 = 0.88$, $p <<< 0.05$). For the Cl concentration and Cl/Br regressions residuals versus distance from the coastline, tests for autocorrelation and homoskedasticity resulted in acceptance of the null hypotheses that no positive autocorrelation was present (p = 0.86 and 0.88 for Cl concentration and Cl/Br, respectively) and residuals were homoscedastic (p = 0.66 and 0.30 for Cl concentration and Cl/Br, respectively).

Non-thermal end-member distances were estimated using the centroid location of individual geothermal areas and distance values were extracted from the distance from coastline raster output. Using relations between Cl/Br and Cl concentrations, Br was estimated for mixing-curve models as Br exhibited a complex pattern with distance from the coast to which linear, exponential, and power functions did not adequately explain observed variation. Uncertainty was incorporated into the Br calculation by propagating prediction interval values at the 95th percentile for respective Cl and Cl/Br concentrations and ratios. As geothermal areas where EMMA was applied lie between 50 and 100 km inland from the coast, incorporation of

calculation uncertainty is important as paired Cl and Br measurements are limited at these distances from the coastlines within the TVZ.

Variability of Cl and Br in hydrothermal fluids among geothermal areas

Considerable variation was observed for Cl/Br ratios and Cl concentrations both within and among geothermal areas (Figure 9). At Kawerau, Mokai, Ohaaki, Rotokawa, and Wairakei where multiple hydrothermal-well measurements are available, hydrothermal well data do not necessarily covary linearly as evidenced by the range of Cl/Br ratios and concentrations. However, in all investigated geothermal areas, a general linear trend is observed between hydrothermal well and hydrothermal surface discharge features.

Within individual geothermal areas, Cl concentrations and Cl/Br ratios generally decrease from hydrothermal wells to hydrothermal surface features to modeled non-thermal groundwater values. The highest hydrothermal-well Cl values were observed in wells at Mokai (99 mmol/kg) while the lowest values observed were at Rotokawa (5.8 mmol/kg). The highest Cl/Br ratios were observed in Mokai (1664) and the lowest (577) were observed in Ohaaki. Overlap between hydrothermal surface discharge and hydrothermal wells is also present. At Waiotapu and Ohaaki. extensive overlap is observed between hydrothermal surface and hydrothermal wells Cl/Br ratios more so than other geothermal areas investigated with similar hydrothermal well and hydrothermal surface discharge median values. At Waiotapu, concentrations in hydrothermal surface discharge exceed hydrothermal well values in some cases and at Ohaaki, a number of hydrothermal wells are lower in Cl concentrations of hydrothermal surface discharge.

Br-Cl mixing relations

Hydrothermal surface discharge values generally plotted along or close to mixing curves generated using estimated low-temperature groundwater concentrations (Figure 10). In order to address variability stemming from small variations in Br concentrations, additional modeled curves were generated by modeling Br end-member values ± 10 and 30 %. Mixing ratios showed considerable range among selected areas with estimated hydrothermal dilutions less than 10% of the hydrothermal end-member to over 100 % (i.e. concentrating of hydrothermal end-member).

In typical, low-temperature applications, having over 100% of an end-member would be considered an infeasible solution and suggest an invalid end-member assumption. However, concentration of solutes through boiling is a well-established phenomena and, for hydrothermal systems, does not immediately invalidate the hydrothermal well end-members at depth. As observed at Waiotapu, several values are in exceedance of the hydrothermal end-member value, but are similar in ratio. In geothermal areas where hydrothermal surface discharge Cl values were approaching less than 1 millimoles/kg or approximately 10 % of the hydrothermal end-member, these data consistently plotted below the mixing curve.

δ^2H-Cl relations

From the data compiled, δ^2H-Cl paired measurements for hydrothermal wells and hydrothermal surface discharge were only available for Mokai, Ngatamariki, Waiotapu, and Wairakei. Non-thermal groundwater data for Cl and δ^2H was only available for Mokai whereas nonthermal Cl and δ^2H values for Ngatamariki, Waiotapu, and Wairakei were estimated. The majority of hydrothermal surface features plot between the low-temperature and hydrothermal well end-member values of δ^2H and Cl (Figure 11) with the exception of Waiotapu. Modeled

δ^2H values using the Online Isotopes in Precipitation Calculator (Bowen, 2019) were similar to compiled measured values where available. Similarly, available Cl-δ^2H paired data for low-temperature groundwater from Hedenquist et al. (1990) plotted close to modeled Cl and δ^2H values.

At Mokai, differences in δ^2H were minimal between non-thermal groundwater, hydrothermal surface discharge, and hydrothermal well values. However, higher δ^2H values were observed for hydrothermal wells at Ngatamariki (+ 3 ‰), Waiotapu (~ + 8 ‰), and Wairakei (+ 3 ‰) versus the low-temperature groundwater values. At Waiotapu, higher δ^2H values were observed for both sites that have greater Cl concentrations than the hydrothermal wells and all but two of the hydrothermal discharge values with Cl concentrations less than the hydrothermal wells. At Ngatamariki, δ^2H of hydrothermal surface discharge ranged from values similar to non-thermal groundwater value to more values slightly higher than the hydrothermal well. At both Waiotapu and Wairakei, where the lowest Cl values were less than 10 millimoles/kg, no difference in δ^2H was observed.

Discussion

Of the numerous geothermal fields in the TVZ, only a limited number of geothermal areas contain paired Br and Cl data and δ^2H-Cl data that encompass both the hydrothermal wells and related hydrothermal surface discharge. Nonetheless, several important observations and interpretations can be made regarding: 1) modeling the distribution of Cl and Br for non-thermal groundwater; 2) Br and Cl EMMA and recirculation in the TVZ; and 3) incorporating these observations with broader numerical and geophysical models of hydrothermal circulation.

Cl-Br spatial variation of shallow groundwater end-members in the TVZ

Distributions of non-thermal Cl/Br ratios and Cl concentrations observed in the TVZ are similar in magnitude and spatial trends compared to previous investigations across North America (Davis et al., 1998; Vengosh and Pankratov, 1998; Freeman, 2007; Katz et al., 2011; Horner et al., 2017). Near the coastline in the TVZ, Cl/Br ratios approach typical coastal values (~ 600) (Katz et al., 2011), but both Cl/Br and Cl concentrations decrease with distance from the coastline (Figure 8) and are interpreted to be resultant of preferential rainout of Cl and retention Br in circulating air masses over the TVZ (Figure 1).

From the derived empirical relations, the respective square root and log transformed relations between distance from the North Island coastline and the Cl/Br ratio and Cl Br concentrations were significantly correlated ($p <<< 0.05$) and relatively successful in explaining over 70 % variation for both Cl/Br ratio ($r^2 = 0.76$) and Cl concentration ($r^2 = 0.88$) of observed variability. Given the shape of the North Island (Figure 4) and high spatial variability of moisture delivery to groundwater systems (Watts, 1947; Dravitzki and McGregor, 2011), the distance from coastline parameter was, seemingly, inclusive of air flow patterns from any direction around the North Island. These findings added evidence that Cl concentrations and Cl/Br ratios in rainfall and groundwater both decrease away from coastlines and, in some cases, may be empirically modeled (Davis et al., 2004; Wetherbee et al., 2018) in the absence of more continental Cl and Br emissions sources (Short et al., 2017; Wetherbee et al., 2018).

However, a greater degree of uncertainty exists in those regions of the TVZ where observational constraints are limited. As such, more diluted hydrothermal surface discharge that plot below the calculated mixing curves may be resultant of poor model constraint in the empirical relation at these locations. Specifically, observational data between 80 and 100 km

distance from the coast are limited (Figure 8). Although, this is the distance bracket where the majority of the sites investigated in this study are located. As there is nearly a three orders of magnitude difference in concentration between Cl and Br (Figure 6), small differences in Cl and Br concentrations will yield large differences in Cl/Br ratios. In turn, improving the accuracy of Br estimations from Cl and Cl/Br relations hinges upon additional Cl-Br analyses from non-thermal groundwater at distances greater than 80 km from the coast.

Even with noted limitations estimating low-temperature end-members, basic empirical modeling has yielded statistically significant and usable empirical relations enabling estimation of low-temperature end-members and the application of EMMA to the TVZ hydrothermal systems.

End-member mixing analysis in TVZ hydrothermal systems

Mixing ratios determined in this study exhibited a wide range of traceable dilution pathways and hydrologic connectivity between hydrothermal reservoirs and low-temperature groundwater. Specifically, Cl concentrations and Cl/Br ratios in hydrothermal surface discharge that are similar to hydrothermal wells reflected more direct connection to respective reservoirs at depth as interpreted at Kawerau, Rotokawa, and Waiotapu (Figures 9 and 10). Conversely, lower Cl and lower Cl/Br ratios are indicative of greater dilution by low-temperature groundwater for some hydrothermal surface discharge (e.g. Ohaaki).

Both among and within geothermal areas, hydrothermal surface discharge showed considerable variation along mixing curves ranging from less than 10% of the hydrothermal end-member at Ngatamariki, Ohaaki, Orakeikorako, Wairakei to greater than 100% of the hydrothermal end-member at Waiotapu. Hydrothermal surface discharge that plotted along or

near modeled mixing curves were inferred to represent 1:1 mixing, as observed at Kawerau and some of the hydrothermal surface discharge at Mokai, Ngatamariki, Orakeikorako, Waiotapu, and Wairakei (Figure 10). However, hydrothermal surface discharge did plot exactly along mixing curves at Ohaaki, Rotokawa, and portion of sites at Ngatamariki, Orakeikorako, Waiotapu, and Wairakei. For these hydrothermal surface discharge that plot close to or below approximately 15% dilution of the hydrothermal end-member, this is likely resultant from overestimation of Br in the low-temperature end-member due to less observational constraint of changes in Cl/Br and Cl with distances greater than ~ 25 km inland.

At Mokai, Ngatamariki, and Rotokawa, Cl/Br ratios are lower than modeled mixing curves (i.e. values plot above the mixing line) by up to ratio values of 1000 (Figure 10). Assuming Cl was not removed from the hydrothermal fluid (Truesdell et al., 1977; Reyes and Trompetter, 2012; Cullen et al., 2015), Br was considered enriched rather than Cl-depleted. However, no significant Br sources exist in the shallower portions of the TVZ hydrothermal systems. Therefore, deviation from modeled mixing curves with lower Cl/Br ratios may be representative non-conservative behavior of Br possibly via phase separation or recirculation of hydrothermal fluids.

Phase separation and enrichment

Investigation of the degree of Cl/Br fractionation in shallow liquid-dominated hydrothermal systems with similar pressure, temperature, and vapor-brine ratios to the TVZ hydrothermal systems is limited (Liebscher, 2007). Investigation of variable Cl/Br fractionation simulating hydrothermal sea vents (i.e. “black smokers”), magma-hydrothermal interfaces, and acidic volcanic lakes have generated contradictory results as to causes and extent of Br enrichment and depletion due to preferential retention liquid and vapor phases (Lüders et al.,

2002; Liebscher et al., 2006; Foustoukos and Seyfried, 2007; Liebscher, 2007; Seo and Zajacz, 2016; Rodríguez et al., 2016, 2018). Review of experimental findings related to Cl/Br variability in hydrothermal sea vents presented by Foustoukos and Seyfried (2007) and magma-hydrothermal interfaces by Seo and Zajacz (2016) suggest the primary factor which affects the degree of Cl/Br fractionation to be brine to vapor density ratio differences whereby Br preferentially goes to the vapor phase (Seo and Zajacs, 2016). However, both field observations and experimental work by (Rodríguez et al., 2016, 2018) suggest preferential retainment of Br in acidic volcanic lakes. While not perfectly analogous, fluid-fluid interactions within hydrothermal systems in the TVZ are considered here to be more similar to hydrothermal sea vent fluids than acidic volcanic lakes. Under this assumption, liquid phase separation would yield Br enrichment.

Evidence for boiling and distilling of solutes

Quantitative assessment of boiling and resultant brine-vapor densities for hydrothermal surface discharge was not undertaken as part of this study. However, determination of whether phase separation was present was made from analysis of δ^2H-Cl relations among low-temperature groundwater, hydrothermal surface discharge, and hydrothermal wells.

Fractionation of oxygen and hydrogen isotopes resulting from phase separation will yield higher δ^2H values in the residual liquid phase in hydrothermal wells and hydrothermal surface discharge relative to low-temperature groundwater (Truesdell et al., 1977). Higher δ^2H values and concentrations of Cl and Br in hydrothermal surface discharge compared to the low-temperature groundwater and hydrothermal well end-member are indicative of extensive boiling and concentrating (i.e. distilling) (Figure 10 and 11). At Waiotapu for example, δ^2H values of hydrothermal surface discharge are nearly 20 ‰ higher than the low-temperature end-member.

Moreover, concentrations of Cl were nearly 100 millimoles/kg greater than the hydrothermal well end-member for some samples.

Excluding Mokai, nearly all of the hydrothermal surface discharge having concentrations greater than 10 millimoles/kg indicated boiling near the surface as δ^2H values were typically 5 to 10 ‰ higher than low-temperature end-member values for respective geothermal areas (Figure 11). Conversely, hydrothermal surface discharge having concentrations less than 10 millimoles/kg do not indicate boiling.

Whether or not boiling as shown from δ^2H-Cl relations affects Cl/Br ratios along mixing curves at Ngatamariki, Wairakei, and Waiotapu remains an open question. However, δ^2H-Cl relations do not indicate boiling in subsurface at Mokai as previously interpreted by Hedenquist et al. (1990). However, Br enrichment was observed relative to modeled mixing curves. Restating the assumptions of no significant source of Br in the subsurface, no Cl depletion due to mineral uptake, explaining Br enrichment in Mokai hydrothermal surface discharge can be done so via hydrothermal fluid recirculation.

Recirculation

Contrary to a strictly 'Neptunist' (i.e. rock-leaching) and 'Plutonist' (i.e. magmatic source) model of Cl and Br origins (Hedenquist and Lowenstern, 1994), recirculated fluids and meteoric-derived Cl and Br distillation could be substantial in hydrothermal systems. As discharge totals of hydrothermal surface discharge at the surface do not always comprise the full hydrothermal plume volume (i.e. single-pass system), the fraction of hydrothermal fluids not discharged at the surface will form lateral migrating hydrothermal plumes in near-surface, shallow aquifers (Elder, 1966).

Along the plume flow path, fluids undergo further mixing and dilution with low-temperature groundwater leading to decreasing lower mixing ratios (Figure 10). However, as hydrothermal plumes laterally migrate near the surface, hydrothermal groundwater conductively cools. Relatively colder hydrothermal fluids will then migrate downward and eventually re-enter hydrothermal circulation at some depth or multiple depths.

If recirculation continues for some time, Cl concentrations in recirculating hydrothermal fluids will remain greater than low-temperature groundwater typically by over an order of magnitude, but Cl/Br will decrease due to concentrating of Br from low-temperature groundwater. This concentrating (or distillation) of Br would then lower the Cl/Br ratio of the hydrothermal fluid. The recirculation process as described here is interpreted to be occurring at Mokai for the two hydrothermal discharge sites associated with Mokai, these ratios have been lowered by over 100. Therefore, it is possible that a proportion of recirculated hydrothermal fluids and meteoric derived Cl and Br that return to hydrothermal circulation via 'recirculation' may be underestimated not only in the TVZ hydrothermal systems, but liquid-dominated hydrothermal systems, globally. From Cl isotopic investigations, recirculated 'near surface' groundwater has been previously interpreted in Icelandic hydrothermal systems to be a significant contributor to hydrothermal Cl fluxes (Stefánsson and Barnes, 2016).

Conceptual model of Cl-Br and δ^2H-Cl evolution

Groundwater circulation and associated hydrochemical evolution within hydrothermal systems consists not only hydrothermal reservoirs and associated hydrothermal wells, but initial downward migration of relatively cold groundwater to the base of hydrothermal convection, heating and chemical transformation of groundwater, and subsequently, migration of hydrothermal fluids to relatively more shallow depths to the form of hydrothermal reservoirs

(Ingebritsen and Sanford, 1999; Ingebritsen et al., 2010). Drawing from an array of previous geophysical, geological, and hydrogeological investigation of hydrothermal groundwater circulation, flow paths and hydrochemical evolution was conceptualized (Figure 12).

Cl and Br values of downward migrating low-temperature groundwater on the periphery of a hydrothermal convection cell are not likely to undergo any subsurface interactions that would alter their Cl/Br ratios and are effectively conservative (Davis et al., 1998). Upon 'entry' into the saturated portion of the groundwater system, stable isotope values are also isotopically 'conservative' given low, initial temperatures where no fractionation from phase separation is present (Figure 13).

As groundwater migrates downward further in the crust, groundwater heats with depth accelerating rock-water interaction (Newton and Manning, 2010; Bucher and Stober, 2011). These reaction pathways are not static in time and 'evolve' based on both internal and external factors in the crust, which include groundwater recharge rates, permeability, mineralogy, and stress field changes from local and distal deformation (see Newton and Manning, 2011). Specifically, if groundwater flow rates are high, time needed for water-rock exchange may not be possible. Meaning, Cl and Br concentrations, Cl/Br ratios, and δ^2H values will be similar to initial groundwater values (Figure 13A-B; positions 1 and 2).

Where downward propagation is slower, mobile elements (e.g. Cl, Br) may be incorporated into groundwater circulation increasing salinity. This expediates development of brine formation, increasing Cl and Br concentrations and potentially altering Cl/Br ratios (Figure 13A; position 3). Unless hydrogen or oxygen isotope exchange is prevalent from interactions with clay or silicate minerals, respectively, water isotopes are likely unaffected. Evolution of salinity and water isotope compositions in the distal portion of the hydrothermal convection are

likely transient owing to changes in heat flow and permeability over time (Weis, 2015) as evidenced in geochemical and isotope variability of fluid inclusions (Newton and Manning, 2010).

At the base of convection, particularly in the presence of an intrusion or zone of partial melt as predicted in the TVZ, groundwater is likely to undergo substantial changes in salinity increasing orders of magnitude greater than initial groundwater recharge for Cl/Br ratios (Figure 13A; position 4). Changes arise from equilibration of groundwater with exsolved fluids associated with magmatic intrusions and zones of partial melt, which may exsolve HCl, HBr, H_2S, HCL, and HF forming an acidic, saline brine near the interface of the intrusion and circulating groundwater (Henley and Ellis, 1983; Giggenbach, 1995; Villemant and Boudon, 1999; Arnorsson et al., 2007; Bégué et al., 2015; Scott et al., 2015, 2017; Weis, 2015). Such salinity increases may lead to halite saturation and a magmatic halide 'front'.

In numerical simulation, the presence of halite saturated zones are typically 'flushed out' from continued hydrothermal circulation over time (Weis et al., 2012). Formation of halogen-metal complexes (Cole and Drummond, 1986; Simmons and Brown, 2006; Blamey, 2012) and further water-rock interaction may remove some amount of Cl and Br with alteration of mineral phases (Heinrich et al., 1993; Reyes and Trompetter, 2012). However, changes in Cl/Br ratios beyond experimental simulation are unclear and predicted to be highly dependent on both water-rock and halogen-metal ratios (Hurwitz et al., 2005; Bernal et al., 2014; Cullen et al., 2015; Seo and Zajacz, 2016).

Water isotope compositions in equilibrium with exsolved magmatic fluids are predicted to be highly enriched in $\delta^{18}O$; however, $\delta^{2}H$ compositions for (-10 to -50 ‰) overlap with those in meteoric, surface, and shallow groundwater environments (Figure 13B; position 4) (Friedman,

1953; Craig and Gordon, 1965; Hedenquist and Lowenstern, 1994; Giggenbach, 1995). Experimental studies suggest Cl/Br fractionation and phase separation (leading to isotopic fractionation of δ^2H) at the depths of geothermal systems are dynamic and persistent (Villemant and Boudon, 1999; Fekete et al., 2016; Seo and Zajacz, 2016; Scott et al., 2017), but the amount of magmatic water in circulating hydrothermal systems is debated (Giggenbach, 1995; Sharp, 2007).

Phase separation and mixing at the base of hydrothermal convection (Scott et al., 2017) will undoubtedly incorporate some meteoric Cl and Br, but the amount and degree that this alters Cl/Br ratios beneath hydrothermal reservoirs at more shallow depths is unknown. If mixing of groundwater is continuous from the base of convection upwards through the hydrothermal plume, a significant fraction of meteoric CI and Br may be incorporated. Meaning, Cl/Br ratios in hydrothermal reservoirs may not be indicative of Cl/Br ratios in the deeper portion of the hydrothermal system (Figure 13A; position 10). Overall, specific chemical evolution trajectories for the Cl-Br-δ^2H system at P-T conditions in the crust at depths not currently penetrated by geothermal production companies or scientific drilling operations remain elusive. Modeling of ascending fluid compositions must, nonetheless, converge on observed values in hydrothermal wells currently observed (Figure 13; positions 5-10).

Conclusions

Development and application of EMMA was used to interpret mixing ratios between low- and high-temperature groundwater present in the Taupo Volcanic Zone, New Zealand, which included estimation of low-temperature end-members from empirical spatial analysis. While the paucity of available data limits more specific spatiotemporal analysis of individual features,

application of EMMA for exploratory analysis of differences among geothermal areas provided preliminary ranges of mixing ratios and potential recirculation evidence in TVZ hydrothermal systems. Key future objectives related to application of EMMA in the TVZ reside on reducing uncertainties related to end-member determination of both non-thermal groundwater and hydrothermal end-members. Moreover, while deviations along modeled Br-Cl mixing curves could be potentially explained by Cl/Br fractionation, knowledge on Cl/Br partitioning at lower temperatures and pressures is needed.

Use of EMMA has immediate applications in ongoing monitoring efforts in the TVZ associated with geothermal energy regulations and volcanogenic hazards. Recirculation processes described in the conceptual model suggest that meteoric solutes in hydrothermal systems may be underestimated, but more in-depth analysis and potential inclusion of Br within NaCl multiphase models is needed.

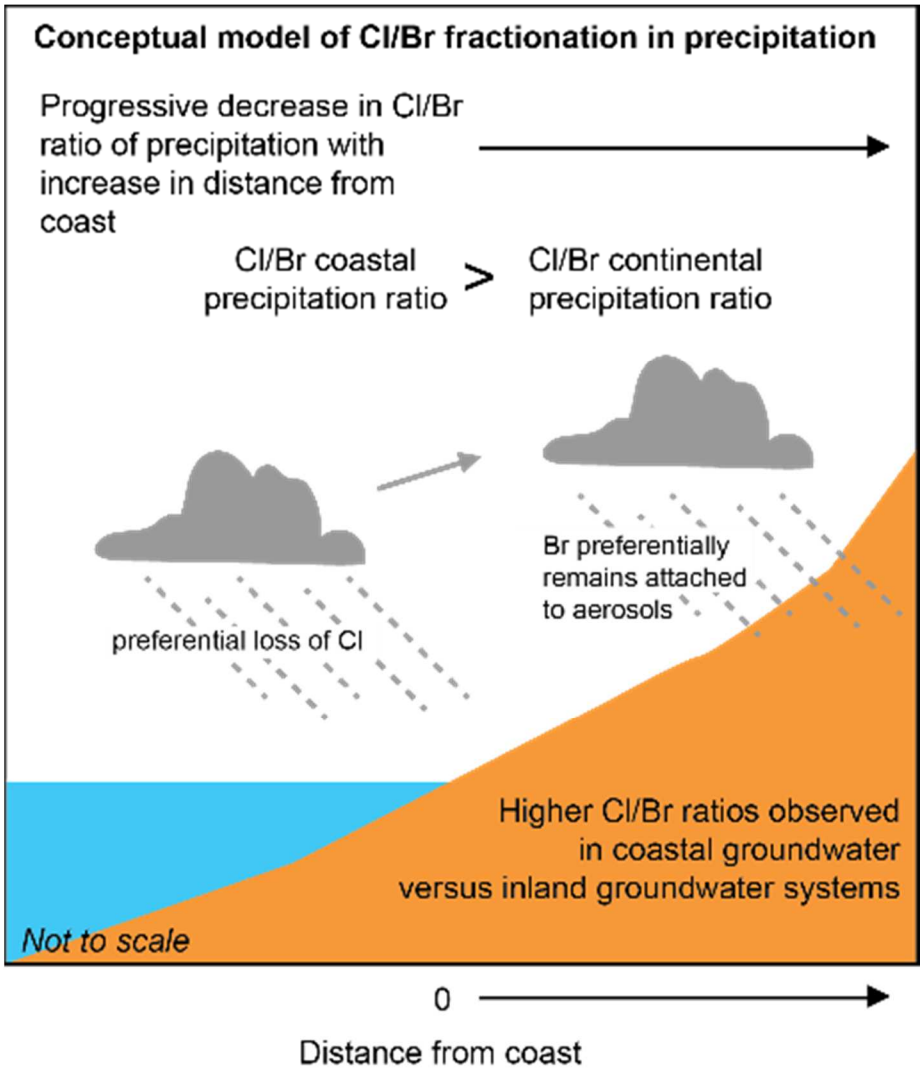

Figure 1. Conceptual model of Cl/Br evolution from coastal to inland sites. Cl/Br decreases from coastal sites to inland sites as Cl is preferentially lost versus preferential retainment of residual Br in air masses (Davis et al. 1998; Short et al., 2017).

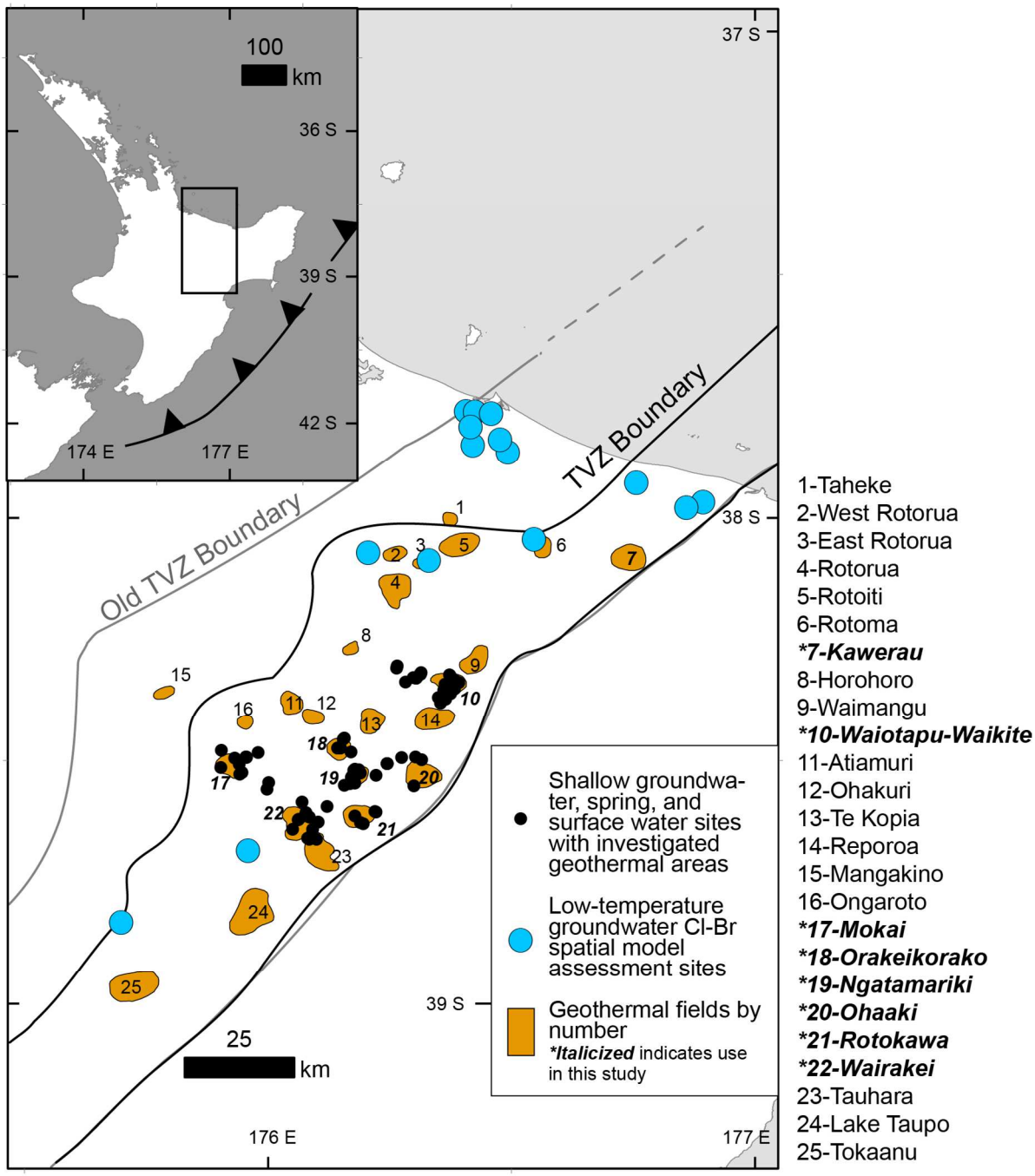

Figure 2. Location of Taupo Volcanic Zone study area within the North Island, New Zealand (inset). 'Old' and 'Modern' TVZ boundaries are shown (Wilson et al., 1995). Geothermal areas delineated by 30 Ωm resistivity boundary (modified from Rowland et al., 2011) and enumerated. Geothermal areas in this study, hydrothermal surface discharge, and non-thermal groundwater sites are indicated.

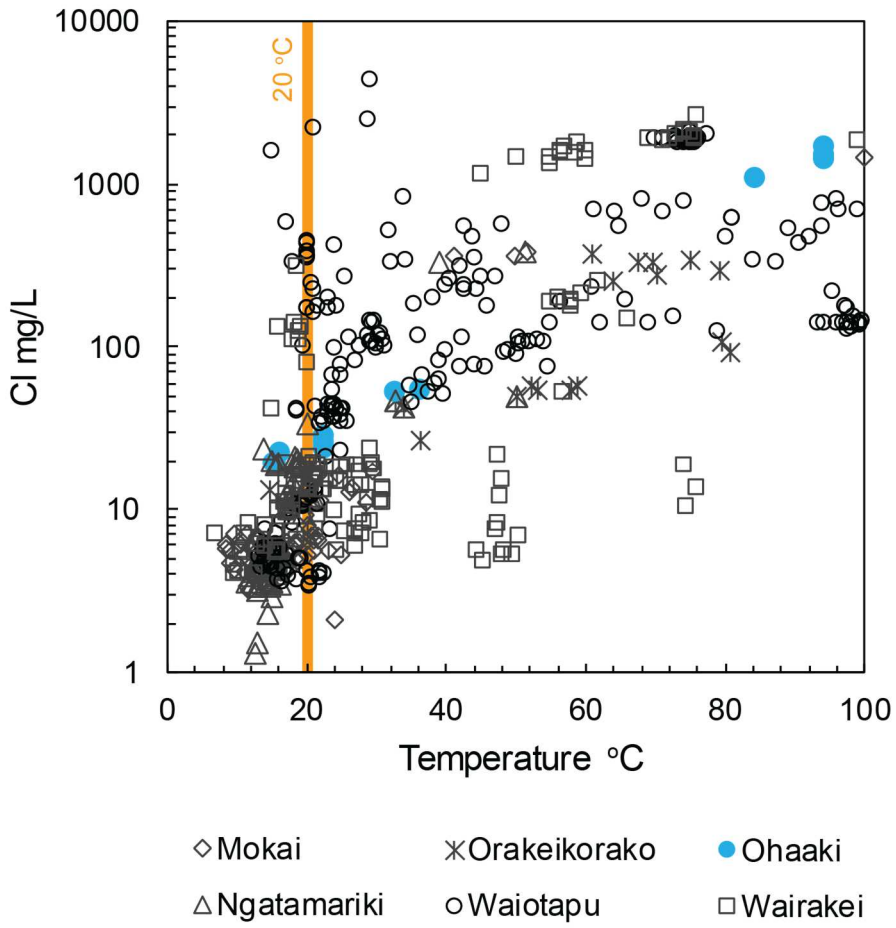

Figure 3. Temperature and Cl concentrations for groundwater and surface waters within the TVZ from available data in selected geothermal areas. The 20 °C thermal/non-thermal 'cutoff' is labeled. While a general increase in Cl concentration is observed with temperature, conductive cooling of high-temperature fluids may also yield greater Cl concentrations at lower temperatures as observed for Cl concentrations greater than 100 mg/L less than and equal to 20 °C (Truesdell et al., 1977; Hedenquist and Browne, 1989; Hedenquist et al., 1990; Giggenbach et al., 1994).

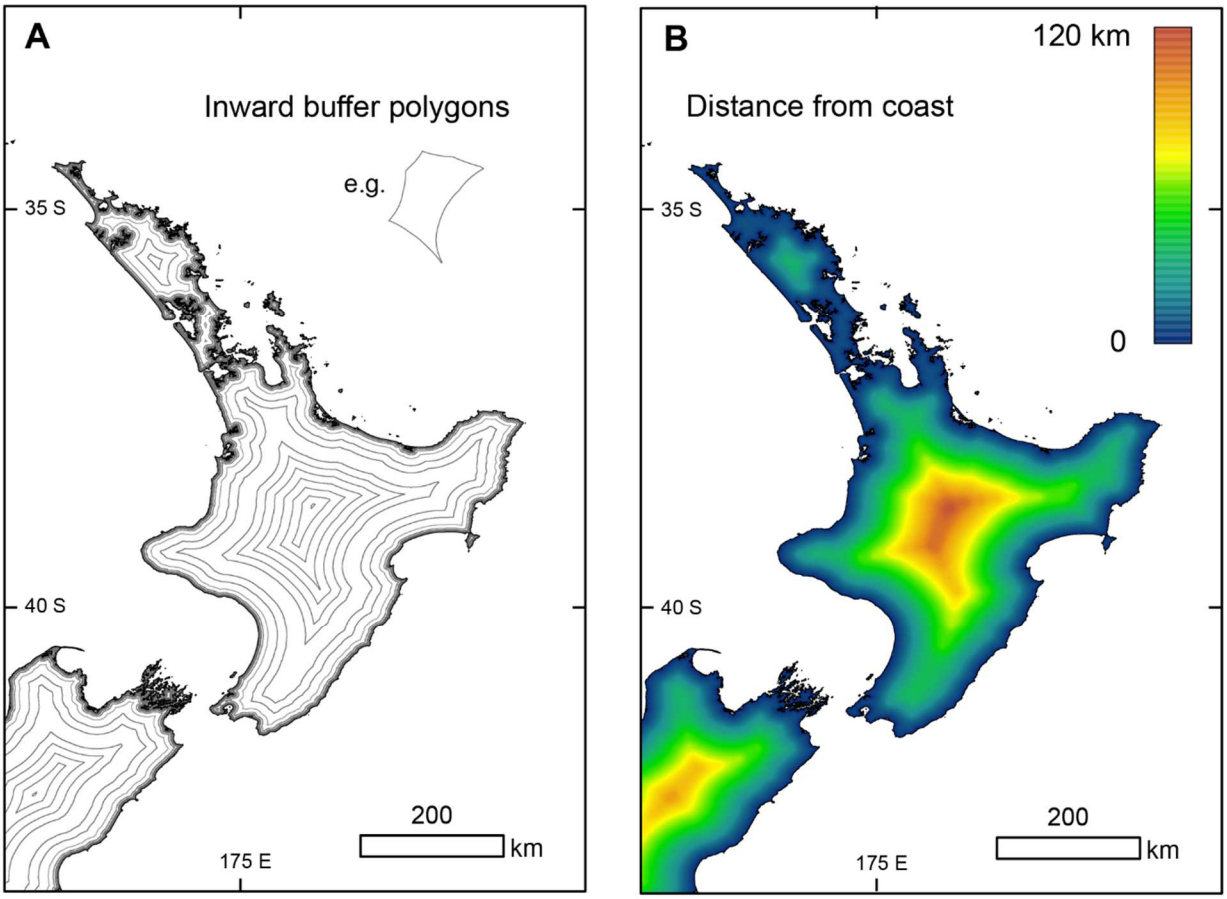

Figure 4. A) Inward buffer polygons generated at incremental distances inward from the New Zealand coastline. **B)** Distance from coast interpolation using *Topo to Raster* (ESRI, 2019).

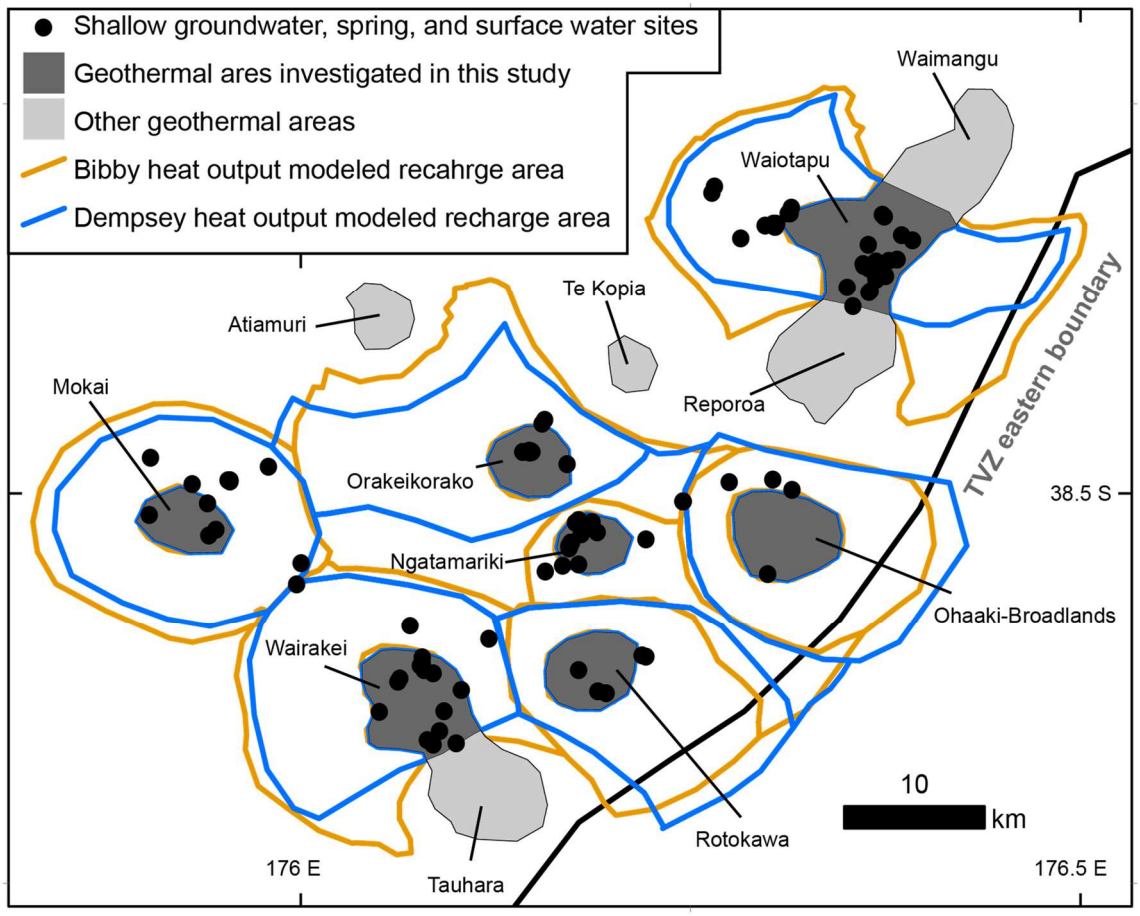

Figure 5. Geothermal catchment areas derived from Bibby heat output and modeled output values from Dempsey et al. (2012). Geothermal areas and groundwater and surface water sites are indicated.

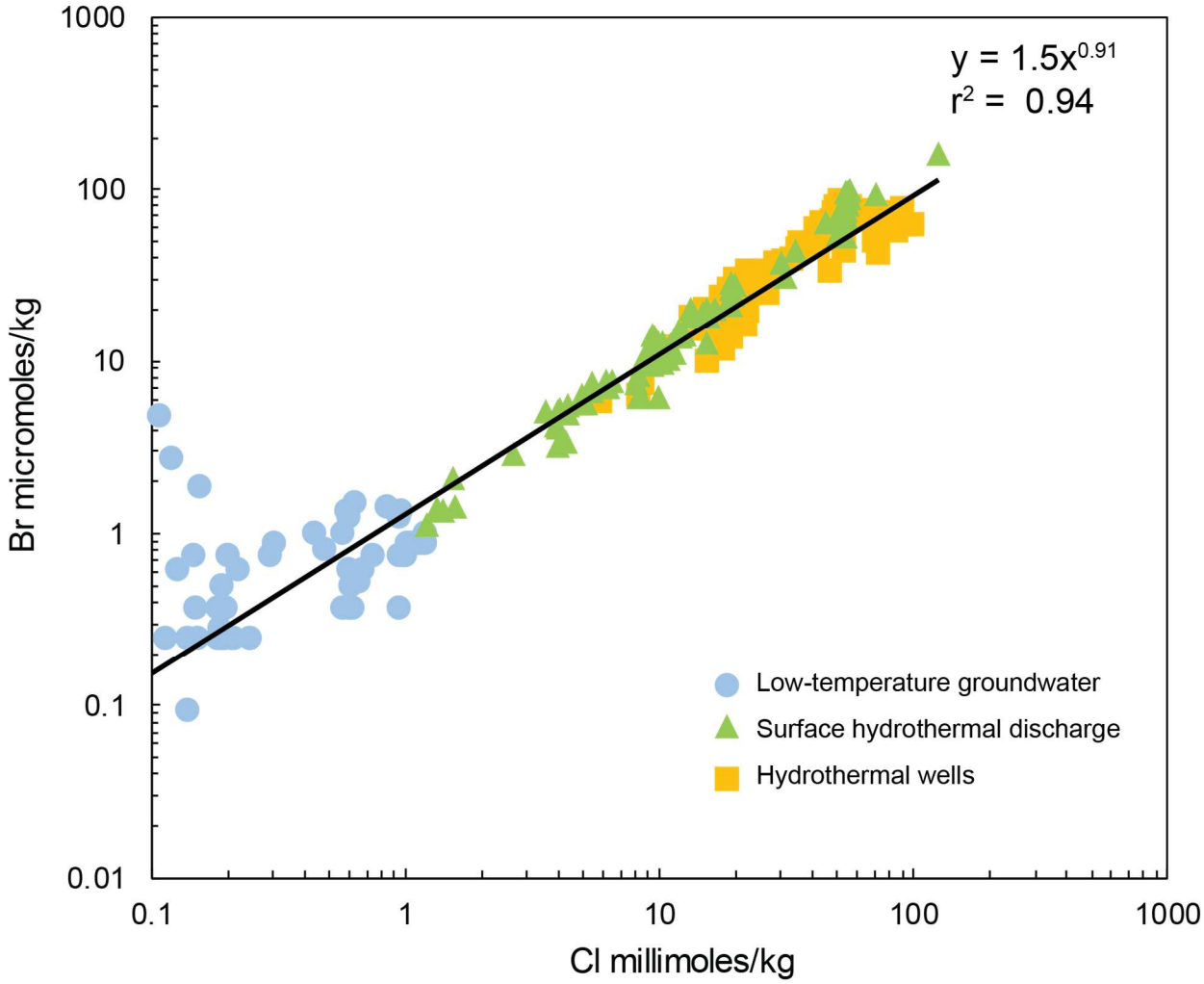

Figure 6. Cl (millimoles/kg) versus Br (micromoles/kg) for non-thermal groundwater, surface hydrothermal discharge, and hydrothermal wells for compiled data in the Taupo Volcanic Zone.

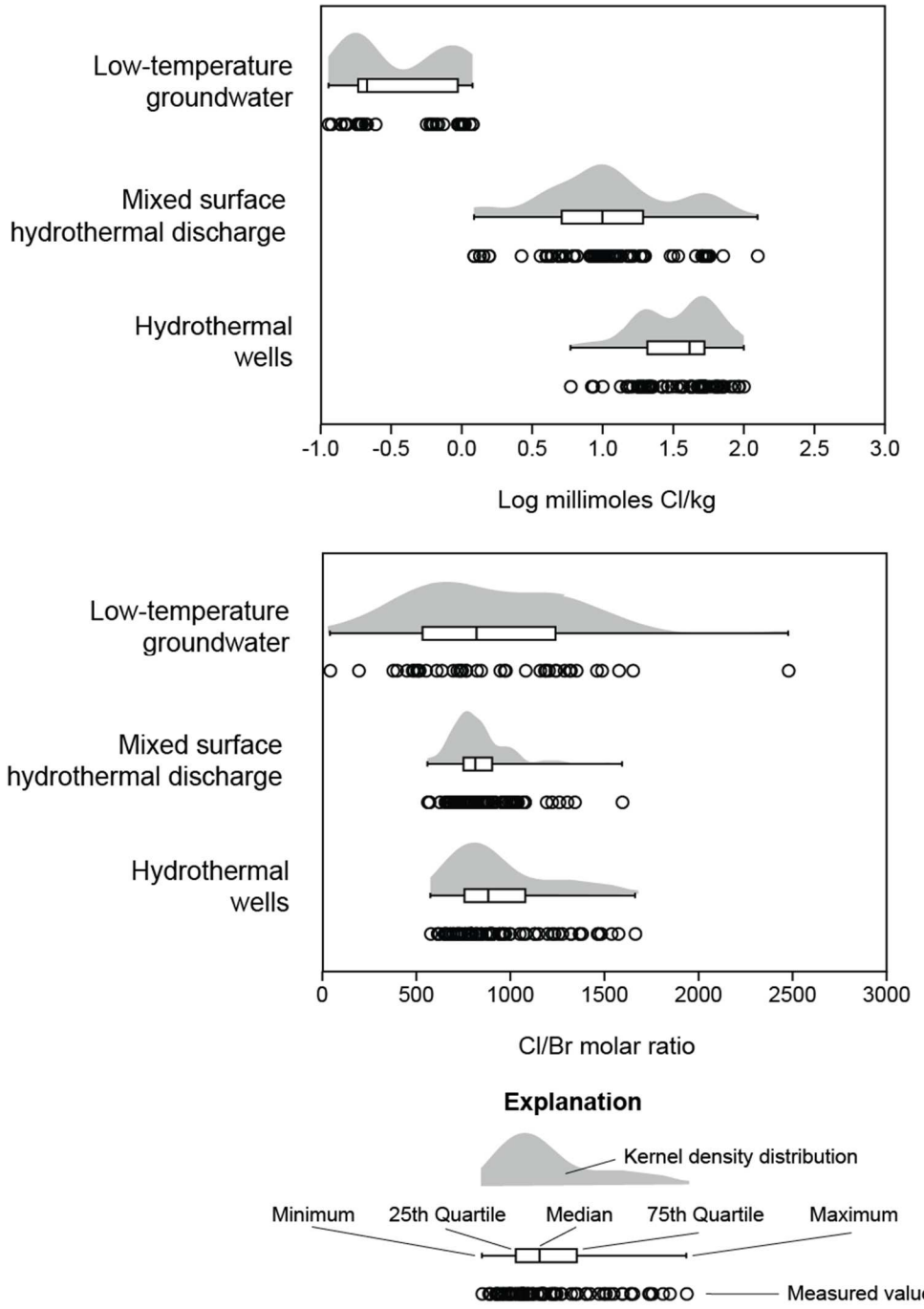

Figure 7. Box plots, kernel density distributions, and individual data for Cl concentrations, log10(millimoles Cl/kg), and Cl/Br ratios among low-temperature, hydrothermal surface discharge, and hydrothermal wells in the TVZ.

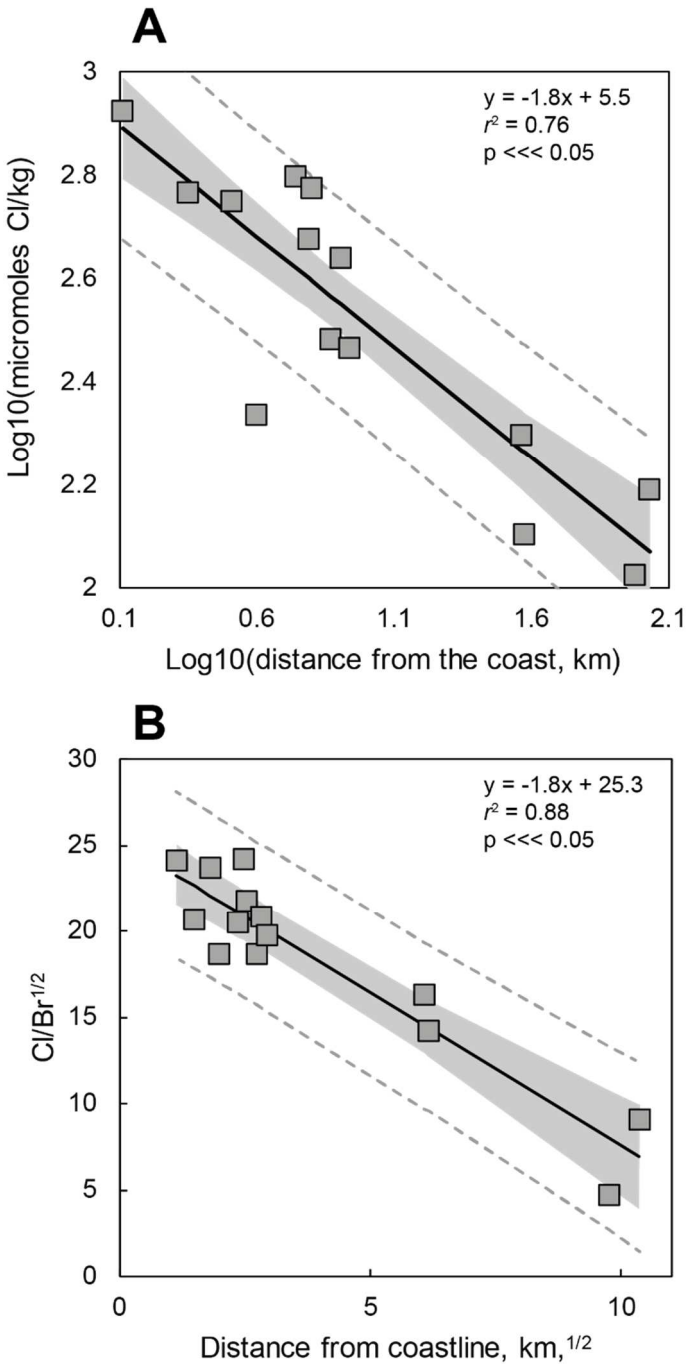

Figure 8A. Log10(millimoles Cl/kg) versus log10(distance from the coast, km) and **B.** Square root of Cl/Br ratio versus square root of distance from the coast, km.

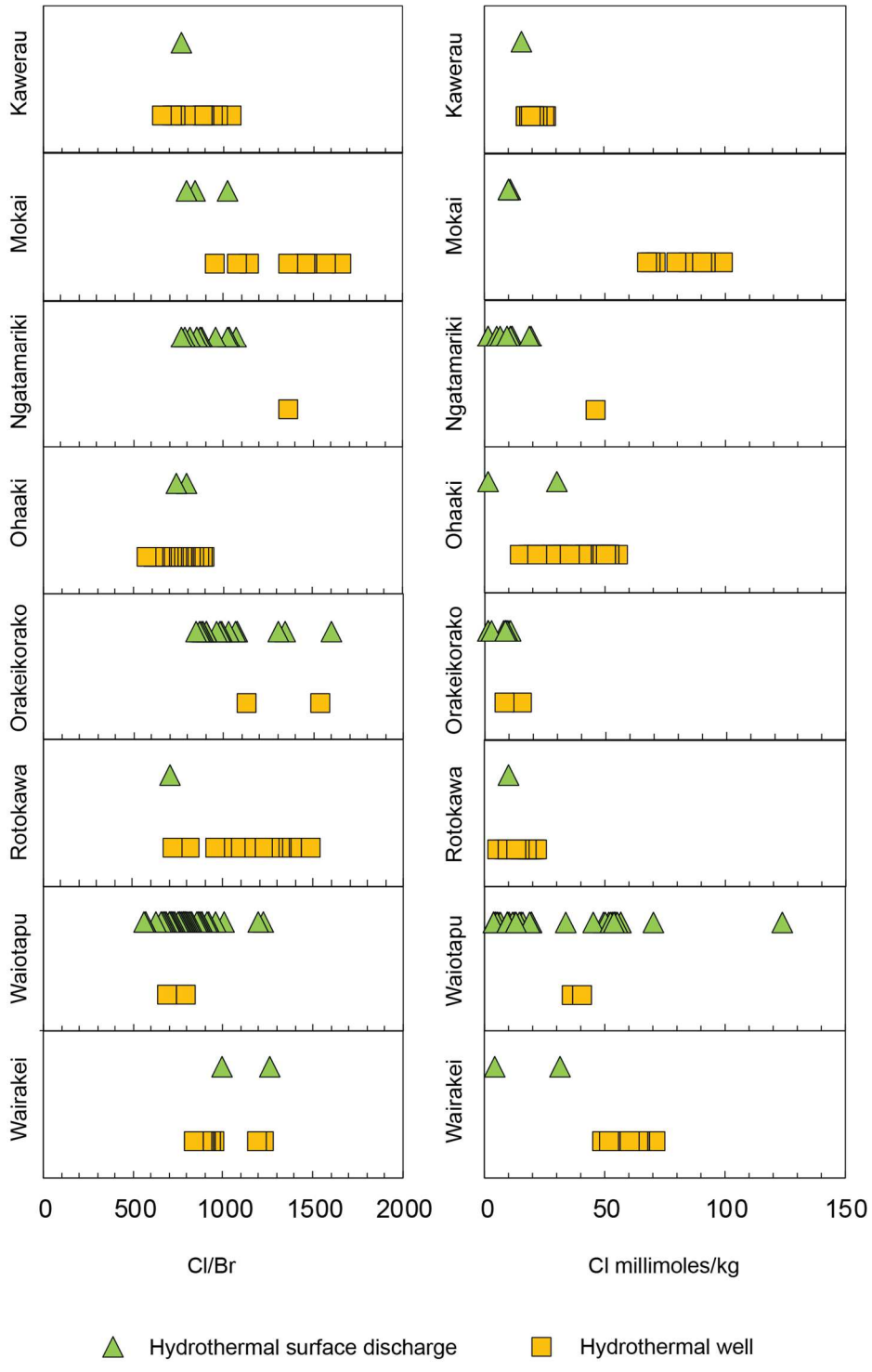

Figure 9. Compiled Cl/Br ratios and Cl concentrations for eight selected geothermal areas.

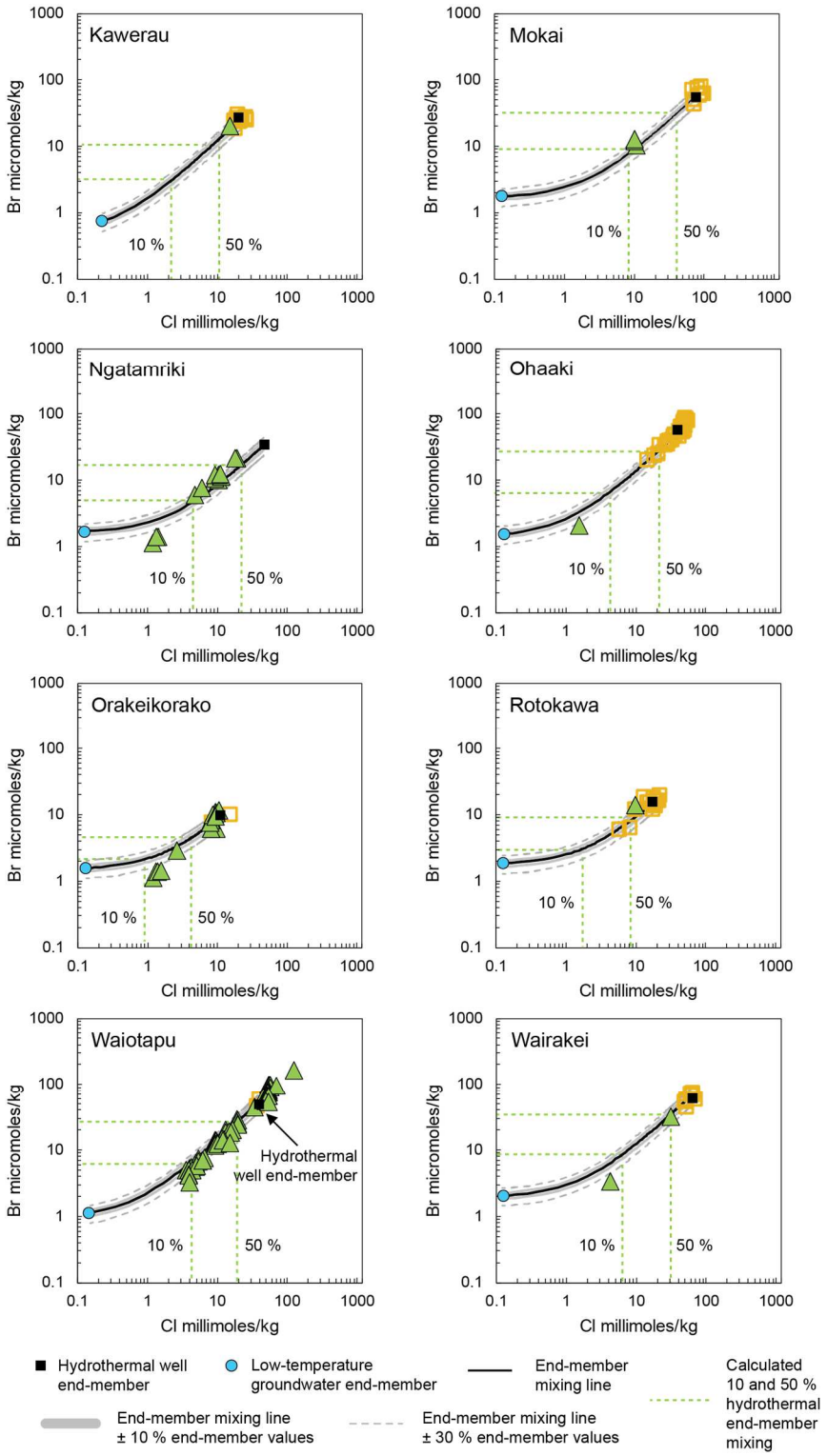

Figure 10. Mixing curves generated for eight geothermal areas. Hydrothermal well end-member and estimated non-thermal end-members are indicated. Estimated mixing ratio of 10 and 50 % hydrothermal end-member remaining are also labeled (dashed green lines). End-members are varied ±10 and 30 %.

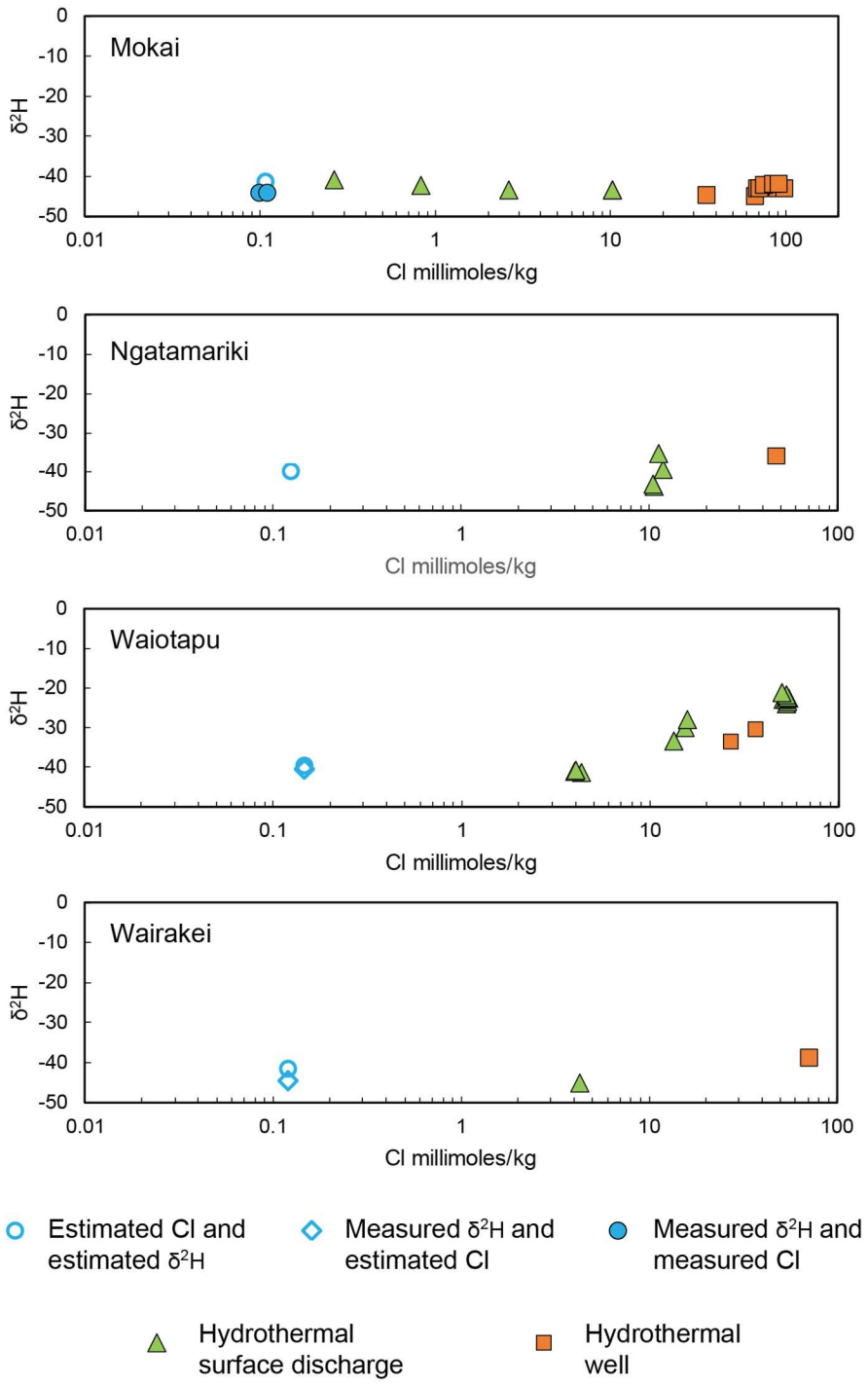

Figure 11. δ^2H-Cl values are shown for selected sites containing available data. Non-thermal values constitute purely estimated from empirical relations and δ^2H values from the Online Isotope Precipitation Calculator (Bowen, 2008), measured δ^2H and estimated Cl, and measured δ^2H and measured Cl (from Hedenquist et al., 1990b).

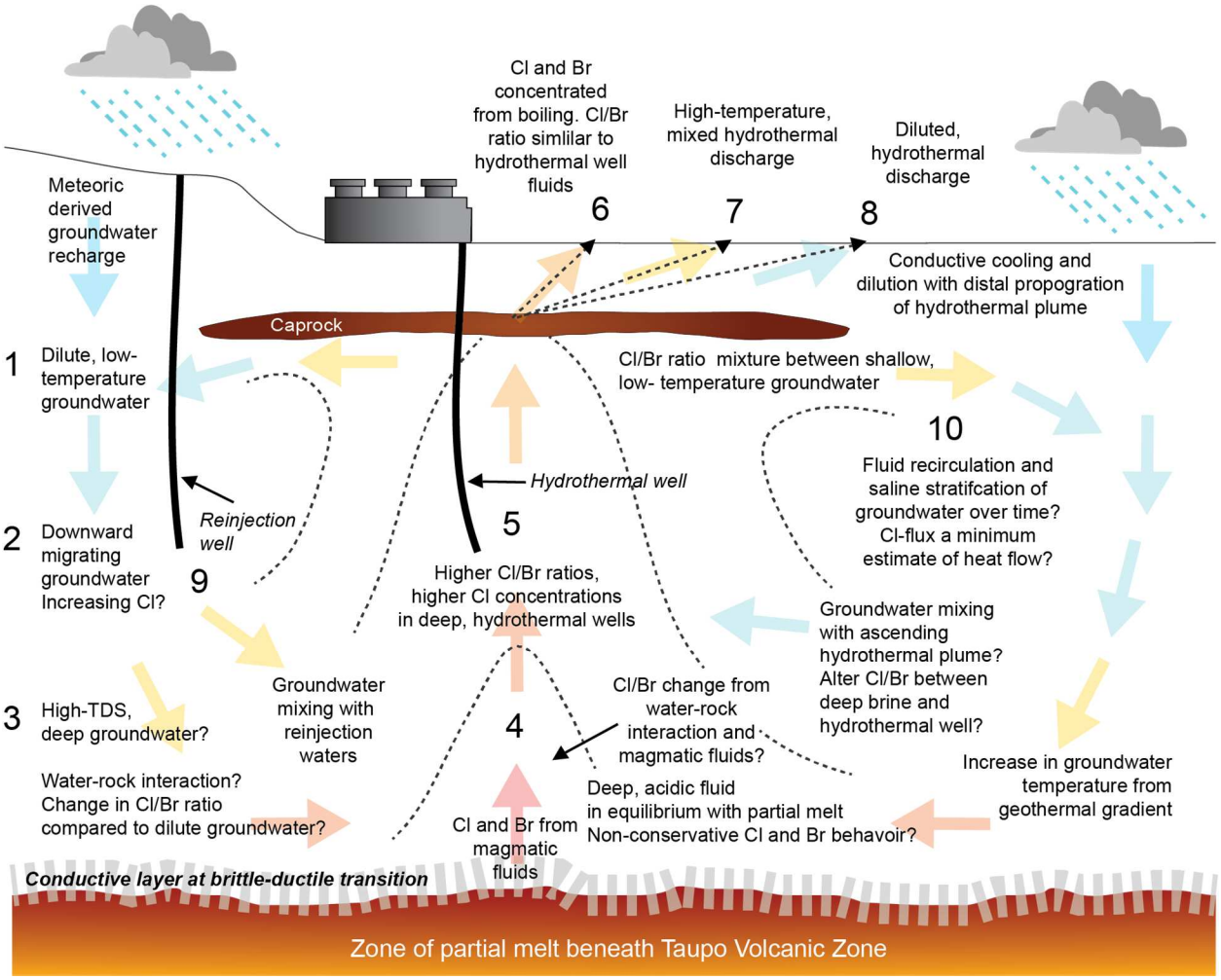

Figure 12. Conceptual schematic of potential fluid-fluid and fluid-rock chemical exchange pathways and groundwater flow paths within a liquid-dominated hydrothermal system similar to the TVZ. Numbers correspond to labels in subsequent figures.

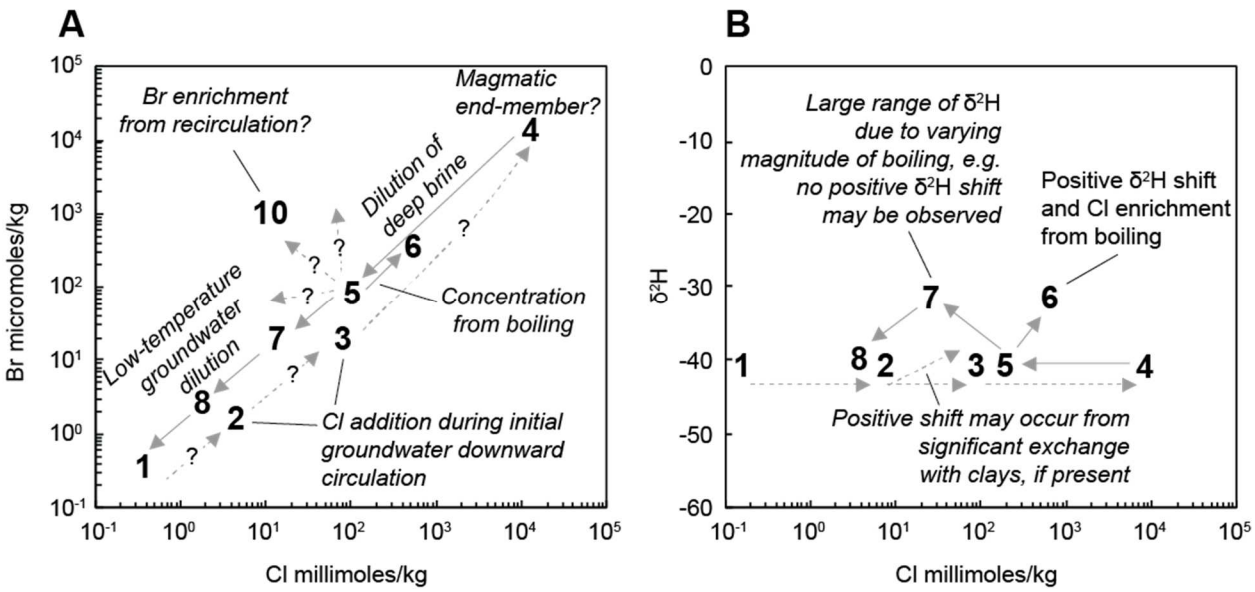

Figure 13A-B, Corresponding geochemical evolution of fluids within a liquid dominated hydrothermal system similar to those in the TVZ denoted by numbered positions (referenced in text).

References Cited

Ague, J.J., 2014, Fluid Flow in the Deep Crust, in Treatise on Geochemistry, Elsevier, v. 4, p. 203–247, doi:10.1016/B978-0-08-095975-7.00306-5.

Arnórsson, S., and Andrésdóttir, A., 1995, Processes controlling the distribution of boron and chlorine in natural waters in Iceland: Geochimica et Cosmochimica Acta, v. 59, p. 4125–4146, doi:10.1016/0016-7037(95)00278-8.

Arnorsson, S., Stefansson, A., and Bjarnason, J.O., 2007, Fluid-Fluid Interactions in Geothermal Systems: Reviews in Mineralogy and Geochemistry, v. 65, p. 259–312, doi:10.2138/rmg.2007.65.9.

Bannister, S., Reyners, M., Stuart, G., and Savage, M., 2007, Imaging the Hikurangi subduction zone, New Zealand, using teleseismic receiver functions: crustal fluids above the forearc mantle wedge: Geophysical Journal International, v. 169, p. 602–616, doi:10.1111/j.1365-246X.2007.03345.x.

Bégué, F., Deering, C.D., Chambefort, I., Gravley, D.M., and Kennedy, B.M., 2015, Link Between Magmatic Degassing and Geothermal Systems ; Taupo Volcanic Zone , New Zealand: Proceedings World Geothermal Congress 2015, Melbourne, Australia, p. 19–25.

Bernal, N.F., Gleeson, S.A., Dean, A.S., Liu, X.-M., and Hoskin, P., 2014, The source of halogens in geothermal fluids from the Taupo Volcanic Zone, North Island, New Zealand: Geochimica et Cosmochimica Acta, v. 126, p. 265–283, doi:10.1016/j.gca.2013.11.003.

Bertrand, E.A. et al., 2012, Magnetotelluric imaging of upper-crustal convection plumes beneath the Taupo Volcanic Zone, New Zealand: Geophysical Research Letters, v. 39, p. n/a-n/a, doi:10.1029/2011GL050177.

Bibby, H.M., Caldwell, T.G., Davey, F.J., and Webb, T.H., 1995, Geophysical evidence on the structure of the Taupo Volcanic Zone and its hydrothermal circulation: Journal of Volcanology and Geothermal Research, v. 68, p. 29–58, doi:10.1016/0377-0273(95)00007-H.

Blamey, N.J.F., 2012, Composition and evolution of crustal, geothermal and hydrothermal fluids interpreted using quantitative fluid inclusion gas analysis: Journal of Geochemical Exploration, v. 116–117, p. 17–27, doi:10.1016/j.gexplo.2012.03.001.

Blanchard, D.C., and Syzdek, L.D., 1972, Concentration of bacteria in jet drops from bursting bubbles: Journal of Geophysical Research, v. 77, p. 5087–5099, doi:10.1029/JC077i027p05087.

Bloch, M.R., Kaplan, D., Kertes, V., and Schnerb, J., 1966, Ion separation in bursting air Bubbles: an explanation for the irregular ion ratios in atmospheric precipitations: Nature, v. 209, p. 802–803, doi:10.1038/209802a0.

Bowen, G., 2008, OPIC: The online isotopes in precipitation calculator: Waterisotopes.org,.

Bowen, G., 2019, The online isotopes in precipitation calculator, version 2.2: Downloaded from http://www. waterisotopes. org on, v. 16.

Bucher, K., and Stober, I., 2011, Fluids in the Upper Continental Crust: Frontiers in Geofluids, p. 241–253, doi:10.1002/9781444394900.ch17.

Burton, M.R., Sawyer, G.M., and Granieri, D., 2013, Deep Carbon Emissions from Volcanoes: Reviews in Mineralogy and Geochemistry, v. 75, p. 323–354, doi:10.2138/rmg.2013.75.11.

Caine, J.S., Evans, J.P., and Forster, C.B., 1996, Fault zone architechture and permeability structure: Geology, v. 24, p. 1025–1028, doi:10.1130/0091-7613(1996)024<1025.

Caracausi, A., Ditta, M., Italiano, F., Longo, M., Nuccio, P.M., Paonita, A., and Rizzo, A., 2005, Changes in fluid geochemistry and physico-chemical conditions of geothermal systems caused by magmatic input: The recent abrupt outgassing off the island of Panarea (Aeolian Islands, Italy): Geochimica et Cosmochimica Acta, v. 69, p. 3045–3059, doi:10.1016/j.gca.2005.02.011.

Caracausi, A., Paternoster, M., and Nuccio, P.M., 2015, Mantle CO2 degassing at Mt. Vulture volcano (Italy): Relationship between CO2 outgassing of volcanoes and the time of their last eruption: Earth and Planetary Science Letters, v. 411, p. 268–280, doi:10.1016/j.epsl.2014.11.049.

Chiodini, G., Granieri, D., Avino, R., Caliro, S., Costa, A., and Werner, C., 2005, Carbon dioxide diffuse degassing and estimation of heat release from volcanic and hydrothermal systems: Journal of Geophysical Research B: Solid Earth, v. 110, p. 1–17, doi:10.1029/2004JB003542.

Cole, D.R., and Drummond, S.E., 1986, The effect of transport and boiling on Ag/Au ratios in hydrothermal solutions: a preliminary assessment and possible implications for the formation of epithermal precious-metal ore deposits: Journal of Geochemical Exploration, v. 25, p. 45–79, doi:10.1016/0375-6742(86)90007-5.

Craig, H., and Gordon, L.I., 1965, Deuterium and oxygen 18 variations in the ocean and marine atmosphere, in Tongiorgi, E. ed., Stable Isotopes in Oceanographic Studies and Paleotemperatures, Pisa, V. Lishi e F., p. 9–130.

Cullen, J.T., Barnes, J.D., Hurwitz, S., and Leeman, W.P., 2015, Tracing chlorine sources of thermal and mineral springs along and across the Cascade Range using halogen concentrations and chlorine isotope compositions: Earth and Planetary Science Letters, v. 426, p. 225–234, doi:10.1016/j.epsl.2015.06.052.

Darby, D.J., Hodgkinson, K.M., and Blick, G.H., 2000, Geodetic measurement of deformation in the Taupo Volcanic Zone, New Zealand: The north Taupo network revisited: New Zealand Journal of Geology and Geophysics, v. 43, p. 157–170, doi:10.1080/00288306.2000.9514878.

Daughney, C.J., and Randall, M., 2009, National groundwater quality indicators update : state and trends 1995-2008.:

Davis, S.N., Fabryka-Martin, ;, Wolfsberg, J.T.;, and Laura E, 2004, Variations of Bromide in Potable Ground Water in the United States: Ground Water, v. 42, p. 902–909, doi:10.1111/j.1745-6584.2004.t01-8-.x.

Davis, S.N., Whittemore, D.O., Fabryka-Martin, J., Fabryka-Martin, ;, Wolfsberg, J.T.;, and Laura E, 1998, Uses of Chloride/Bromide Ratios in Studies of Potable Water: Ground Water, v. 36, p. 338–350, doi:10.1111/j.1745-6584.1998.tb01099.x.

Dempsey, D.E., Simmons, S.F., Archer, R.A., and Rowland, J. V., 2012, Delineation of catchment zones of geothermal systems in large-scale rifted settings: Journal of Geophysical Research: Solid Earth, v. 117, p. 1–19, doi:10.1029/2012JB009515.

Dravitzki, S., and McGregor, J., 2011, Extreme precipitation of the Waikato region, New Zealand: International Journal of Climatology, v. 31, p. 1803–1812, doi:10.1002/joc.2189.

Elder, J.W., 1966, Heat and Mass Transfer in the Earth: Hydrothermal Systems: Wellington, New Zealand Department of Scientific and Industrial Research, v. 169, 115 p., https://catalogue.nla.gov.au/Record/1865431 (accessed June 2019).

ESRI, 2019, ArcGIS Desktop:

Evans, W.C., van Soest, M.C., Mariner, R.H., Hurwitz, S., Ingebritsen, S.E., Wicks, C.W., and Schmidt, M.E., 2004, Magmatic intrusion west of Three Sisters, central Oregon, USA: The perspective from spring geochemistry: Geology, v. 32, p. 69, doi:10.1130/G19974.1.

Fajans, K., 1923, Struktur und Deformation der Elektronenhüllen in ihrer Bedeutung für die chemischen und optischen Eigenschaften anorganischer Verbindungen: Die Naturwissenschaften, v. 11, p. 165–172, doi:10.1007/BF01552365.

Fehn, U., and Snyder, G.T., 2003, Chapter 9 Origin of Iodine and 129 I in Volcanic and Geothermal Fluids from the North Island of New Zealand : Implications for Subduction Zone Processes: Society of Economic Geologists, v. 10, p. 159–170.

Fekete, S., Weis, P., Driesner, T., Bouvier, A.S., Baumgartner, L., and Heinrich, C.A., 2016, Contrasting hydrological processes of meteoric water incursion during magmatic–hydrothermal ore deposition: An oxygen isotope study by ion microprobe: Earth and Planetary Science Letters, v. 451, p. 263–271, doi:10.1016/j.epsl.2016.07.009.

Fournier, R.O., Kennedy, B.M., Aoki, M., and Thompson, J.M., 1994, Correlation of gold in siliceous sinters with 3He/4He in hot spring waters of Yellowstone National Park: Geochimica et Cosmochimica Acta, v. 58, p. 5401–5419, doi:10.1016/0016-7037(94)90238-0.

Foustoukos, D.I., and Seyfried, W.E., 2007, Fluid Phase Separation Processes in Submarine Hydrothermal Systems: Reviews in Mineralogy and Geochemistry, v. 65, p. 213–239, doi:10.2138/rmg.2007.65.7.

Freeman, J.T., 2007, The use of bromide and chloride mass ratios to differentiate salt-dissolution and formation brines in shallow groundwaters of the Western Canadian Sedimentary Basin: Hydrogeology Journal, v. 15, p. 1377–1385, doi:10.1007/s10040-007-0201-1.

Friedman, I., 1953, Deuterium content of natural waters and other substances: Geochimica et Cosmochimica Acta, v. 4, p. 89–103, doi:10.1016/0016-7037(53)90066-0.

Fuge, R., 1988, Sources of halogens in the environment, influences on human and animal health: Environmental Geochemistry and Health, v. 10, p. 51–61, doi:10.1007/BF01758592.

Gadagkar, S.R., and Call, G.B., 2015, Computational tools for fitting the Hill equation to dose–response curves: Journal of Pharmacological and Toxicological Methods, v. 71, p. 68–76, doi:10.1016/J.VASCN.2014.08.006.

Garnier, B.J. (Benjamin J., and 1917-, 1950, New Zealand weather and climate:, http://agris.fao.org/agris-search/search.do?recordID=US201300655710 (accessed May 2019).

Gerlach, T.M., Delgado, H., McGee, K.A., Doukas, M.P., Venegas, J.J., and Cárdenas, L., 1997, Application of the LI-COR CO 2 analyzer to volcanic plumes: A case study, volcán Popocatépetl, Mexico, June 7 and 10, 1995: Journal of Geophysical Research: Solid Earth, v. 102, p. 8005–8019, doi:10.1029/96JB03887.

Giggenbach, W.F., 1995, Variations in the chemical and isotopic composition of fluids discharged from the Taupo Volcanic Zone, New Zealand: Journal of Volcanology and Geothermal Research, v. 68, p. 89–116, doi:10.1016/0377-0273(95)00009-J.

Giggenbach, W.F., Sheppard, D.S., Robinson, B.W., Stewart, M.K., and Lyon, G.L., 1994, Geochemical structure and position of the Waiotapu geothermal field, New Zealand\r[Monograph] Waimangu, Waiotapu, and Waikite geothermal systems, New Zealand: Geothermics, v. 23, p. 599–644.

Goff, F., and Gardner, J.N., 1994, Evolution of a mineralized geothermal system, Valles Caldera, New Mexico: Economic Geology, v. 89, p. 1803–1832, doi:10.2113/gsecongeo.89.8.1803.

Goff, F., and Janik, C.J., 2002, Gas geochemistry of the Valles caldera region, New Mexico and comparisons with gases at Yellowstone, Long Valley and other geothermal systems: Journal of Volcanology and Geothermal Research, v. 116, p. 299–323, doi:10.1016/S0377-0273(02)00222-6.

Golder Associates, 2013, REGEMP II 2013 interpretation of geochemical data: Waikato Regional Council Technical Report 2013/30, p. 32.

Hammer, Ø., Harper, D.A.T., Ryan, D.D., and Ryan, P.D., 2001, PAST : Paleontological statistics software package for education and data analysis: Palaeontologia Electronica, v. 4, p. 9, doi:10.1016/j.bcp.2008.05.025.

Hedenquist, J.W., and Browne, P.R.., 1989, The evolution of the Waiotapu geothermal system, New Zealand, based on the chemical and isotopic composition of its fluids, minerals and rocks: Geochimica et Cosmochimica Acta, v. 53, p. 2235–2257, doi:10.1016/0016-7037(89)90347-5.

Hedenquist, J.W., Goff, F., Phillips, F.M., Elmore, D., and Stewart, M.K., 1990, Groundwater Dilution and Residence Times, and Constraints on Chloride Source, in the Mokai Geothermal System, New Zealand, From Chemical, Stable Isotope, Tritium, and 36 Cl Data: Journal of Geophysical Research, v. 95, p. 19365–19375, doi:10.1029/JB095iB12p19365.

Hedenquist, J.W., and Lowenstern, J.B., 1994, The role of magmas in the formation of hydrothermal ore deposits: Nature, v. 370, p. 519–527, doi:10.1038/370519a0.

Heinrich, C.A., Bain, J.H.C., Fardy, J.J., and Waring, C.L., 1993, Br/Cl geochemistry of hydrothermal brines associated with Proterozoic metasediment-hosted copper mineralization at Mount Isa, northern Australia: Geochimica et Cosmochimica Acta, v. 57, p. 2991–3000, doi:10.1016/0016-7037(93)90288-8.

Heise, W., Caldwell, T.G., Bibby, H.M., and Bennie, S.L., 2010, Three-dimensional electrical resistivity image of magma beneath an active continental rift, Taupo Volcanic Zone, New Zealand: Geophysical Research Letters, v. 37, p. n/a-n/a, doi:10.1029/2010GL043110.

Henley, R.W., and Ellis, A.J., 1983, Geothermal systems ancient and modern: a geochemical review: Earth-Science Reviews, v. 19, p. 1–50, doi:10.1016/0012-8252(83)90075-2.

Hochstein, M.P., 1995, Crustal heat transfer in the Taupo Volcanic Zone (New Zealand): comparison with other volcanic arcs and explanatory heat source models: Journal of Volcanology and Geothermal Research, v. 68, p. 117–151, doi:10.1016/0377-0273(95)00010-R.

Horner, K.N., Short, M.A., and McPhail, D.C., 2017, Chloride and bromide sources in water: Quantitative model use and uncertainty: Journal of Hydrology, v. 549, p. 571–580, doi:10.1016/J.JHYDROL.2017.04.028.

Houghton, B.F., Wilson, C.J.N., McWilliams, M.O., Lanphere, M.A., Weaver, S.D., Briggs, R.M., and Pringle, M.S., 1995, Chronology and dynamics of a large silicic magmatic system: Central Taupo Volcanic Zone, New Zealand: Geology, v. 23, p. 13, doi:10.1130/0091-7613(1995)023<0013:CADOAL>2.3.CO;2.

Hurwitz, S., and Lowenstern, J.B., 2014, Dynamics of the Yellowstone hydrothermal system: Reviews of Geophysics, v. 52, p. 375–411, doi:10.1002/2014RG000452.

Hurwitz, S., Mariner, R.H., Fehn, U., and Snyder, G.T., 2005, Systematics of halogen elements and their radioisotopes in thermal springs of the Cascade Range, Central Oregon, Western USA: Earth and Planetary Science Letters, v. 235, p. 700–714, doi:10.1016/j.epsl.2005.04.029.

Ingebritsen, S.E. et al., 2013, Hydrothermal monitoring data from the Cascade Range, northwestern United States:, doi:10.5066/F72N5088.

Ingebritsen, S.E., Geiger, S., Hurwitz, S., and Driesner, T., 2010, Numerical simulation of magmatic hydrothermal systems: Reviews of Geophysics, v. 48, p. RG1002, doi:10.1029/2009RG000287.

Ingebritsen, S.E., and Sanford, W.E., 1999, Groundwater in Geologic Processes:, doi:10.2113/gseegeosci.15.1.48.

Ingebritsen, S.E., Sherrod, D.R., and Mariner, R.H., 1989, Heat flow and hydrothermal circulation in the cascade range, north-central Oregon.: Science (New York, N.Y.), v. 243, p. 1458–62, doi:10.1126/science.243.4897.1458.

Katz, B.G., Eberts, S.M., and Kauffman, L.J., 2011, Using Cl/Br ratios and other indicators to assess potential impacts on groundwater quality from septic systems: A review and examples from principal aquifers in the United States: Journal of Hydrology, v. 397, p. 151–166, doi:10.1016/j.jhydrol.2010.11.017.

Kissling, W.M., and Weir, G.J., 2005, The spatial distribution of the geothermal fields in the Taupo Volcanic Zone, New Zealand: Journal of Volcanology and Geothermal Research, v. 145, p. 136–150, doi:10.1016/j.jvolgeores.2005.01.006.

Kresse, T.M., and Hays, P.D., 2009, Geochemistry, comparative analysis, and physical and chemical characteristics of the thermal waters east of Hot Springs National Park, Arkansas, 2006-09: U.S. Geological Survey Scientific Investigations Report 2009-5263:, doi:10.3133/sir20095263.

Krupp, R.E., and Seward, T.M., 1987, The Rotokawa geothermal system, New Zealand; an active epithermal gold-depositing environment: Economic Geology, v. 82, p. 1109–1129, doi:10.2113/gsecongeo.82.5.1109.

Lewis, D., 2010, Elementary Statistics for Geographers, 3rd edn: Journal of the Royal Statistical Society: Series A (Statistics in Society), v. 173, p. 464–464, doi:10.1111/j.1467-985x.2009.00634_5.x.

Liebscher, A., 2007, Experimental Studies in Model Fluid Systems: Reviews in Mineralogy and Geochemistry, v. 65, p. 15–47, doi:10.2138/rmg.2007.65.2.

Liebscher, A., Lüders, V., Heinrich, W., and Schettler, G., 2006, Br/Cl signature of hydrothermal fluids: Liquid-vapour fractionation of bromine revisited: Geofluids, v. 6, p. 113–121, doi:10.1111/j.1468-8123.2006.00135.x.

Liuzzo, M., Gurrieri, S., Giudice, G., and Giuffrida, G., 2013, Ten years of soil CO2 continuous monitoring on Mt. Etna: Exploring the relationship between processes of soil degassing and volcanic activity: Geochemistry, Geophysics, Geosystems, v. 14, p. 2886–2899, doi:10.1002/ggge.20196.

Lorrey, A., Williams, P., Salinger, J., Martin, T., Palmer, J., Fowler, A., Zhao, J., and Neil, H., 2008, Speleothem stable isotope records interpreted within a multi-proxy framework and implications for New Zealand palaeoclimate reconstruction: Quaternary International, v. 187, p. 52–75, doi:10.1016/j.quaint.2007.09.039.

Lowenstern, J.B., Bergfeld, D., Evans, W.C., and Hurwitz, S., 2012, Generation and evolution of hydrothermal fluids at Yellowstone: Insights from the Heart Lake Geyser Basin: Geochemistry, Geophysics, Geosystems, v. 13, p. 1–20, doi:10.1029/2011GC003835.

Lowenstern, J.B., Evans, W.C., Bergfeld, D., and Hunt, A.G., 2014, Prodigious degassing of a billion years of accumulated radiogenic helium at Yellowstone.: Nature, v. 506, p. 355–8, doi:10.1038/nature12992.

Lowenstern, J.B., and Hurwitz, S., 2008, Monitoring a Supervolcano in Repose: Heat and Volatile Flux at the Yellowstone Caldera: Elements, v. 4, p. 35–40, doi:10.2113/GSELEMENTS.4.1.35.

Lüders, V., Banks, D.A., and Halbach, P., 2002, Extreme Cl/Br and δ37Cl isotope fractionation in fluids of modern submarine hydrothermal systems: Mineralium Deposita, v. 37, p. 765–771, doi:10.1007/s00126-002-0309-0.

Lyon, G., and Hulston, J., 1984, Carbon and hydrogen isotopic compositions of New Zealand geothermal gases: Geochimica et Cosmochimica Acta, v. 48, p. 1161–1171,

http://www.sciencedirect.com/science/article/pii/0016703784900528 (accessed January 2013).

Marini, L., and Gambardella, B., 2005, Geochemical modeling of magmatic gas scrubbing: Annals of Geophysics, v. 48, p. 739–753.

Martini, M., 1996, Chemical Characters of the Gaseous Phase in Different Stages of Volcanism: Precursos and Volcanic Activity, in Scarpa, R. and Tilling, R. eds., Monitoring and mitigation of volcano hazards, Berlin, Heidelberg, Springer, p. 199–219, doi:10.1007/978-3-642-80087-0.

Menzies, C.D., Teagle, D.A.H., Craw, D., Cox, S.C., Boyce, A.J., Barrie, C.D., and Roberts, S., 2014, Incursion of meteoric waters into the ductile regime in an active orogen: Earth and Planetary Science Letters, v. 399, p. 1–13, doi:10.1016/j.epsl.2014.04.046.

Menzies, C.D., Teagle, D.A.H., Niedermann, S., Cox, S.C., Craw, D., Zimmer, M., Cooper, M.J., and Erzinger, J., 2016, The fluid budget of a continental plate boundary fault: Quantification from the Alpine Fault, New Zealand: Earth and Planetary Science Letters, v. 445, p. 125–135, doi:10.1016/j.epsl.2016.03.046.

Millot, R., Hegan, A., and Négrel, P., 2012, Geothermal waters from the Taupo Volcanic Zone, New Zealand: Li, B and Sr isotopes characterization: Applied Geochemistry, v. 27, p. 677–688, doi:10.1016/j.apgeochem.2011.12.015.

Moore, J.N., and Simmons, S.F., 2013, Geophysics. More power from below.: Science (New York, N.Y.), v. 340, p. 933–4, doi:10.1126/science.1235640.

Moreau-Fournier, M., Reeves, R.R., Reshitnyk, L., and Daughney, C.J., 2010, Incorporation of New Zealand regional authority state of the environment groundwater quality data into the GNS Science Geothermal-Groundwater Database.:

Mörner, N.-A., and Etiope, G., 2002, Carbon degassing from the lithosphere: Global Planet. Change, v. 33, p. 185–203, doi:10.1016/S0921-8181(02)00070-X.

Nadeau, O., Stix, J., and Williams-Jones, A.E., 2016, Links between arc volcanoes and porphyry-epithermal ore deposits: Geology, v. 44, p. 11–14, doi:10.1130/G37262.1.

Newton, R.C., and Manning, C.E., 2010, Role of saline fluids in deep-crustal and upper-mantle metasomatism: insights from experimental studies: Geofluids, v. 10, p. 58–72, doi:10.1111/j.1468-8123.2009.00275.x.

Pavel Jungwirth†, ‡ and, and Douglas J. Tobias*, §, 2001, Molecular Structure of Salt Solutions: A New View of the Interface with Implications for Heterogeneous Atmospheric Chemistry:, doi:10.1021/JP012750G.

Phillips, D.L., and Gregg, J.W., 2001, Uncertainty in source partitioning using stable isotopes: Oecologia, v. 127, p. 171–179, doi:10.1007/s004420000578.

Pope, J., and Brown, K.L., 2014, Geochemistry of discharge at Waiotapu geothermal area, New Zealand – Trace elements and temporal changes: Geothermics, v. 51, p. 253–269, doi:10.1016/j.geothermics.2014.01.006.

Pope, J.G., McConchie, D.M., Clark, M.D., and Brown, K.L., 2004, Diurnal variations in the chemistry of geothermal fluids after discharge, Champagne Pool, Waiotapu, New Zealand: Chemical Geology, v. 203, p. 253–272, doi:10.1016/j.chemgeo.2003.10.004.

Ratouis, T.M.P., and Zarrouk, S.J., 2016, Factors controlling large-scale hydrodynamic convection in the Taupo Volcanic Zone (TVZ), New Zealand: Geothermics, v. 59, p. 236–251, doi:10.1016/J.GEOTHERMICS.2015.09.003.

Reyes, A.G., and Trompetter, W.J., 2012, Hydrothermal water–rock interaction and the redistribution of Li, B and Cl in the Taupo Volcanic Zone, New Zealand: Chemical Geology, v. 314–317, p. 96–112, doi:10.1016/j.chemgeo.2012.05.002.

Rodríguez, A., van Bergen, M.J., and Eggenkamp, H.G.M., 2018, Experimental evaporation of hyperacid brines: Effects on chemical composition and chlorine isotope fractionation: Geochimica et Cosmochimica Acta, v. 222, p. 467–484, doi:10.1016/j.gca.2017.10.032.

Rodríguez, A., Eggenkamp, H.G.M., Martínez-Cruz, M., and van Bergen, M.J., 2016, Chlorine isotope and Cl–Br fractionation in fluids of Poás volcano (Costa Rica): Insight into an active volcanic–hydrothermal system: Journal of Volcanology and Geothermal Research, v. 325, p. 70–85, doi:10.1016/j.jvolgeores.2016.05.020.

Rowland, J. V., and Sibson, R.H., 2004, Structural controls on hydrothermal flow in a segmented rift system, Taupo Volcanic Zone, New Zealand: Geofluids, v. 4, p. 259–283, doi:10.1111/j.1468-8123.2004.00091.x.

Salinger, M.J., and Salinger, M.J., 1980, New Zealand Climate: I. Precipitation Patterns: Monthly Weather Review, v. 108, p. 1892–1904, doi:10.1175/1520-0493(1980)108<1892:NZCIPP>2.0.CO;2.

Sanyal, S.K., 2010, Future of Geothermal Energy: PROCEEDINGS, Thirty-Fifth Workshop on Geothermal Reservoir Engineering, v. 24, http://pangea.stanford.edu/ERE/pdf/IGAstandard/SGW/2010/sanyal.pdf.

Scott, S., Driesner, T., and Weis, P., 2017, Boiling and condensation of saline geothermal fluids above magmatic intrusions: Geophysical Research Letters, v. 44, p. 1696–1705, doi:10.1002/2016GL071891.

Scott, S., Driesner, T., and Weis, P., 2015, Geologic controls on supercritical geothermal resources above magmatic intrusions.: Nature communications, v. 6, p. 7837, doi:10.1038/ncomms8837.

Seo, J.H., and Zajacz, Z., 2016, Fractionation of Cl/Br during fluid phase separation in magmatic–hydrothermal fluids: Geochimica et Cosmochimica Acta, v. 183, p. 125–137, doi:10.1016/j.gca.2016.04.009.

Sharp, Z., 2007, Principles of stable isotope geochemistry: Upper Saddle River, NJ 07458, Pearson Education/Prentice Hall.

Short, M.A., de Caritat, P., and McPhail, D.C., 2017, Continental-scale variation in chloride/bromide ratios of wet deposition: Science of The Total Environment, v. 574, p. 1533–1543, doi:10.1016/J.SCITOTENV.2016.08.161.

Simmons, S.F., and Brown, K.L., 2006, Gold in Magmatic Hydrothermal Solutions and the Rapid Formation of a Giant Ore Deposit: Science, v. 314, p. 288–291, doi:10.1126/science.1132866.

Simmons, S.F., and Brown, K.L., 2007, The flux of gold and related metals through a volcanic arc, Taupo Volcanic Zone, New Zealand: Geology, v. 35, p. 1099, doi:10.1130/G24022A.1.

Stefánsson, A., and Barnes, J.D., 2016, Chlorine isotope geochemistry of Icelandic thermal fluids: Implications for geothermal system behavior at divergent plate boundaries: Earth and Planetary Science Letters, v. 449, p. 69–78, doi:10.1016/j.epsl.2016.05.041.

Svensen, H., Hammer, Ø., Mazzini, A., Onderdonk, N., Polteau, S., Planke, S., and Podladchikov, Y.Y., 2009, Dynamics of hydrothermal seeps from the Salton Sea geothermal system (California, USA) constrained by temperature monitoring and time series analysis: Journal of Geophysical Research, v. 114, p. B09201, doi:10.1029/2008JB006247.

Truesdell, A.H., Nathenson, M., and Rye, R.O., 1977, The effects of subsurface boiling and dilution on the isotopic compositions of Yellowstone thermal waters: Journal of Geophysical Research, v. 82, p. 3694–3704, doi:10.1029/JB082i026p03694.

Truesdell, A.H., Thompson, J.M., Coplen, T.B., Nehring, N.L., and Janik, C.J., 1981, The origin of the Cerro Prieto geothermal brine: Geothermics, v. 10, p. 225–238, doi:10.1016/0375-6505(81)90006-7.

Vengosh, A., and Pankratov, I., 1998, Chloride/Bromide and Chloride/Fluoride Ratios of Domestic Sewage Effluents and Associated Contaminated Ground Water: Ground Water, v. 36, p. 815–824, doi:10.1111/j.1745-6584.1998.tb02200.x.

Villemant, B., and Boudon, G., 1999, H2O and halogen (F, Cl, Br) behaviour during shallow magma degassing processes: Earth and Planetary Science Letters, v. 168, p. 271–286, doi:10.1016/S0012-821X(99)00058-8.

Virkkula, A., Aurela, M., Hillamo, R., Mäkelä, T., Pakkanen, T., Kerminen, V.-M., Maenhaut, W., François, F., and Cafmeyer, J., 1999, Chemical composition of atmospheric aerosol in the European subarctic: Contribution of the Kola Peninsula smelter areas, central Europe, and the Arctic Ocean: Journal of Geophysical Research: Atmospheres, v. 104, p. 23681–23696, doi:10.1029/1999JD900426.

Watts, I.E.M., 1947, The relations of New Zealand weather and climate: an analysis of the westerlies: New Zealand Geographer, v. 3, p. 115–129, doi:10.1111/j.1745-7939.1947.tb01458.x.

Weis, P., 2015, The dynamic interplay between saline fluid flow and rock permeability in magmatic-hydrothermal systems: Geofluids, v. 15, p. 350–371, doi:10.1111/gfl.12100.

Weis, P., Driesner, T., Coumou, D., and Geiger, S., 2014, Hydrothermal, multiphase convection of H 2 O-NaCl fluids from ambient to magmatic temperatures: a new numerical scheme and benchmarks for code comparison: Geofluids, v. 14, p. 347–371, doi:10.1111/gfl.12080.

Weis, P., Driesner, T., and Heinrich, C.A., 2012, Porphyry-copper ore shells form at stable pressure-temperature fronts within dynamic fluid plumes: Science, v. 338, p. 1613–1616, doi:10.1126/science.1225009.

Wetherbee, G.A., Lehmann, C.M.B., Kerschner, B.M., Ludtke, A.S., Green, L.A., and Rhodes, M.F., 2018, Trends in bromide wet deposition concentrations in the contiguous United States, 2001–2016: Environmental Pollution, v. 233, p. 168–179, doi:10.1016/J.ENVPOL.2017.10.018.

Williams, C.F., Reed, M.J., Mariner, R.H., DeAngelo, J., and Galanis, S.P., 2008, Assessment of Moderate- and High-Temperature Geothermal Resources of the United States: Fact Sheet, https://pubs.er.usgs.gov/publication/fs20083082 (accessed March 2016).

Wilson, C.J.N., Houghton, B.F., McWilliams, M.O., Lanphere, M.A., Weaver, S.D., and Briggs, R.M., 1995, Volcanic and structural evolution of Taupo Volcanic Zone, New Zealand: a review: Journal of Volcanology and Geothermal Research, v. 68, p. 1–28, doi:10.1016/0377-0273(95)00006-G.

Zhou, M. yu, Yang, S. jin, Parungo, F.P., and Harris, J.M., 1990, Chemistry of marine aerosols over the western Pacific Ocean: Journal of Geophysical Research, v. 95, p. 1779, doi:10.1029/JD095iD02p01779.

Chapter 3. Variable carbon sources and mass fluxes in a hydrothermal watershed, Valles Caldera, New Mexico (USA): implications for tracing surface water sources and lithospheric carbon

This chapter is composed of the publication:

Blackstock, J.M., Hays, P.D., Covington, M.D., in preparation, Variable carbon sources and mass fluxes in a hydrothermal watershed, Valles Caldera, New Mexico (USA): implications for tracing surface water sources and lithospheric carbon: Journal of Geophysical Research–Solid Earth.

Abstract

Carbon dioxide variability and evasion from headwater streams remain elusive components in the terrestrial carbon budget and contribute significant uncertainty in global carbon budget models. Moreover, the mode and magnitude of CO_2 and HCO_3 exports from the lithosphere (i.e. solid-earth degassing) to shallow groundwater and surface waters compound this uncertainty, particularly in areas of known hydrothermal inflows. Longitudinal characterization of stream chemistry is often limited in hydrothermal influenced watersheds, despite the potential for drastic changes to dissolved inorganic carbon (DIC) speciation and $\delta^{13}C_{DIC}$ values related to variable end-member contributions to surface waters. In turn, groundwater contributions are often not accounted leading to an obfuscation of both DIC sources and mass fluxes to surface waters and the atmosphere. In this study, continuous measurement of dissolved PCO_2 and a longitudinal survey of DIC and $\delta^{13}C_{DIC}$ were investigated along the Jemez River and selected upstream tributaries within the Valles Caldera, New Mexico (USA). From continuous

monitoring, this study observed daily PCO_2 fluctuations, which at the Jemez River gage, typically ranged over 100 ppm. From the longitudinal survey, results found DIC chemistry to be complex and spatially varied along a ~ 40 km stream reach. Moreover, this study determined that four groundwater end-members based on DIC and $\delta^{13}C_{DIC}$ contribute to streamflow. Hydrothermal inflows were spatially discrete and altered stream DIC surface water chemistry where present with notably greater contributions of dissolved CO_2 (greatest calculated loads ~ 19 g/s). Analysis of historical data from the USGS Jemez River stream gage station in conjunction with the HCO_3-CO_2* concentrations and load relations determined from the longitudinal survey showed that DIC exports in the Jemez River watershed were not only seasonal, but with increased discharge (e.g. dissolved CO_2 loads increased up to 47 g/s). This seasonal variability was interpreted to coincide with greater groundwater recharge periods, which in turn, increased both low-temperature and high-temperature groundwater contributions to surface waters. Solid-earth degassing from the lithosphere at the Valles Caldera was thereby interpreted to be modulated by groundwater recharge and hydroclimatic variability. Globally, hydroclimatic controls on groundwater movement likely play an outsized role in the magnitude of advective transport of DIC from the lithosphere both currently and in Earth's past.

Introduction

Carbon dioxide in headwater streams has been shown to be a significant carbon source to the atmosphere across a range of ecosystems, albeit concentrations and evasion of CO_2 are highly variable (Liu et al., 2008b; Johnson et al., 2009; Davidson et al., 2010; Florea, 2015; Campeau et al., 2017; Liu and Raymond, 2018). Small spatial scale variability related to groundwater inputs and geomorphological features in headwater reaches, while important drivers of CO_2 evasion, are not well constrained (Campeau et al., 2017; Duvert et al., 2018). Despite having a relatively smaller geographic footprint in landscapes, hydrothermal groundwater inflows can have significant impacts on hydrochemical variability in natural and human-influenced environments and ecosystems (Ellis, 1977; Henley and Ellis, 1983; Bates et al., 1998; Meyer-Dombard et al., 2011; Hanson et al., 2014; Person et al., 2015; Szynkiewicz et al., 2019). , However, these inflows oftentimes go unaccounted if significant mixing and dilution occurs prior to discharge (Hurwitz et al., 2007). In turn, contributions from geogenic sources are proposed to be underestimated in the literature (Rogie et al., 2001; Kerrick, 2001; Burton et al., 2013; Campeau et al., 2017). Specifically, investigation of hydrothermally sourced CO_2* (hereafter, representing dissolved $CO_2 + H_2CO_3$) and HCO_3 exports from groundwater to surface waters in watersheds is limited compared to studies that lack hydrothermal influence (White et al., 1973; Kerrick and Caldeira, 1998; James et al., 1999; Beitler et al., 2003). Understanding not only the temporal, but also longitudinal changes in CO_2* and HCO_3 abundance and related dissolved inorganic C chemistry is critical in characterizing the sources, pathways, fate, and magnitude of carbon exported from hydrothermally influenced watersheds, globally.

Dissolved inorganic carbon speciation and variability in streams is predominately controlled by stream pH (Stumm and Morgan, 1996), stream-gas exchange (Liu and Raymond,

2018), and a myriad of biogenic and geogenic CO_2 sources, sinks, biogeochemical cycling, and stream hydraulics (Evans et al., 2002; Campeau et al., 2017; Liu and Raymond, 2018). In hydrothermal areas, significant inorganic carbon inputs may originate from focused fluid flow associated with acidic, CO_2-rich and neutral, CO_2- and HCO_3-rich springs (Henley and Ellis, 1983; Truesdell et al., 1989; Sheppard et al., 1992; Chiodini et al., 2001; Marini and Gambardella, 2005). If hydrothermal fluid inputs are significant, these inputs may overprint and dominate more typical DIC and $\delta^{13}C_{DIC}$ sources compared to non-thermal groundwater and in-stream biogeochemical cycles. While sources are often well-constrained for hydrothermal groundwater emergences (e.g. subsurface DIC sources to hot springs, hot pools), the longitudinal variability and DIC evolution of surface waters upon mixing with hydrothermal inflows remains uncertain (Evans et al., 2002; Hurwitz et al., 2007).

At the Valles Caldera, work by Trainer (1974) and Trainer et al. (2000) showed surface-water chemical variability in the Jemez River to be intimately linked with hydrothermal inflows and mixing with locally derived groundwater entering the stream. However, investigation of coupled DIC and $\delta^{13}C_{DIC}$ changes resulting from these interactions and associated carbon fluxes, specifically as CO_2* (i.e. combined $CO_{2(g)}$, $CO_{2(aq)}$, and H_2CO_3), have not been investigated. Since, the Valles Caldera systems and Jemez River watershed, collectively, host both acidic and pH-neutral hydrothermal inflows along connected stream reaches, characterization of DIC, $\delta^{13}C_{DIC}$, and mass fluxes of DIC should allow further understanding of the spatial variability, magnitude, and factors affecting hydrothermal DIC contributions to Jemez River watershed.

Data collected to characterize groundwater-surface interactions represents the first longitudinal survey of DIC and $\delta^{13}C_{DIC}$ variability along the Jemez River, New Mexico, USA. An interpretive framework using relations between CO_2*-HCO_3 concentrations and CO_2*-HCO_3

loads was developed, and findings from this study have implications to both methodological approaches and interpretive frameworks regarding interactions between high- and low-temperature groundwater systems. Using long-term available data, this study furthers understanding of the role hydroclimatic variability may have in modulating DIC exchange and export at short-term and longer timescales. This study underscores a potentially underestimated role of hydroclimate-groundwater feedbacks controlling the evolution of surface waters in hydrothermal regions.

Research Questions and Hypotheses

Specific objectives of the following research aimed to answer three main research questions and test three related empirical hypotheses regarding inorganic carbon sources and variability within surface water environments in the Jemez River watershed.

Research Question I

What is rate and magnitude of surface water chemistry change considering the inflows from acidic and pH-neutral hydrothermal inflows to surface waters?

Hypothesis I

Chemically distinct hydrothermal inflows to surface waters should have pronounced effects on stream chemistry if total volume of inflows are high. For example, if low-pH waters dominate contributions to the stream, the stream should be acidic. Conversely, if pH values are higher downstream and contributions increase, the pH of the stream should increase.

Research Question II

Are determination of groundwater end-members possible from analysis of surface water chemical variation?

Hypothesis II

Sampling was conducted during baseflow conditions and prior to the onset of high rainfall characteristic of the onset of the monsoon period in northern New Mexico (late July to September). Therefore, changes in stream chemistry should be, to a degree, coincident with groundwater chemistry to the Jemez River.

Research Question III

For a singular site, do historical streamflow data fit within an estimated end-member framework?

Hypothesis III

Firstly, historical data should be plot within an estimated end-member framework. Moreover, changes in the predominance of one end-member should be evident from changes in streamflow chemistry at a given site through time.

Background

The Valles Caldera is a 21-km wide resurgent caldera (Smith and Bailey, 1968) located at the intersection of the Rio Grande Fault and Jemez Lineament (Goff et al., 1992) (Figure 1A) which formed approximately 1.1 Mya with the eruption of the Bandelier Tuff (Smith and Bailey, 1968). Surficial geology primarily consists of volcanic and igneous lithology (i.e. tuffs, rhyolites, basalt, dacites, andesite) along with Paleozoic and Mesozoic sedimentary rocks draping the

flanks of the caldera (Goff and Gardner, 1994). Hydrothermal alteration assemblages are present in some areas of active and extinct hydrothermal upflow (Hulen et al., 1987). Structurally, a dense ring-fracture network surrounds the caldera, and normal faults are abundant within the middle and southwestern portions of the caldera (Self et al., 1986) and are believed to serve as primary conduits for low- and high-temperature groundwater circulation (Charles et al., 1986; Vuataz and Goff, 1986).

Valles Caldera hydrothermal hydrogeology

Hydrothermal features (i.e. hot springs, fumaroles) occur primarily to the western and southwestern areas of the caldera complex (Trainer, 1974; Vuataz and Goff, 1986; Gardner and Goff, 1996). Upward flow of thermal-water is facilitated by increased permeability associated with faulting (Vuataz and Goff, 1986; Hulen et al., 1987). Within the caldera, both acidic (pH < 3) and neutral (pH ~ 6 to 8) thermal discharge occurs. Acidic (or acid-sulphate) discharge results from condensation of steam- and CO_2-rich vapor at the surface (Henley and Ellis, 1983). Neutral (or neutral-chloride) thermal discharge occurs primarily along the flanks of the caldera and constitute a deep, two-phase solution where gases have not exsolved from hydrothermal groundwater. The H_2O component of hydrothermal water is of meteoric origin (Truesdell and Janik, 1986).

Hydrothermal surface features and deep geothermal well gas chemistry is reflective of a CO_2-rich geothermal reservoir fluid (> 98 mol%). Helium isotopes ($^3He/^4He$) and previous carbon isotope analyses of hot springs and fumaroles suggest a potential magmatic source ($\delta^{13}C_{DIC\text{-}CO_2}$ of ~ -2.5 to -6.8‰) (Goff and Janik, 2002 and references therein). However, distinguishing carbon sources is complicated by interaction with Paleozoic carbonates, which for

$\delta^{13}C_{CaCO_3}$ range from -4 to -8 ‰ for hydrothermally altered limestone and -1.45 ± 3.4‰ of the unaltered limestone (Goff et al., 1985; Hulen et al., 1987; Goff and Janik, 2002). Overall, the Valles gas composition relations (e.g. CH_4-Ar-He; N_2-Ar-He) are similar with magmatic emissions near hot-spot volcanism (e.g. Yellowstone, Kilauea) (Goff and Janik, 2002), but, geochemical evolution of this CO_2-rich hydrothermal fluid from the reservoir to distal portions of the caldera remains a major focus of current research (Goff et al., 1985; McGibbon et al., 2018).

Hydrothermal flow out of the Valles caldera reservoir is primarily facilitated along faults and within Paleozoic strata, specifically the Madera Group (White et al., 1992; Rao et al., 1996). Determination of total hydrothermal outflow is challenging as discharge is located at both hot springs and along seeps in the Jemez River (Trainer et al., 2000). Several estimates of discharge of the hydrothermal plume extending from the Valles Caldera have been made. These estimates range from 10.3 L/s (Erikson, 1977) to 23 L/s (Balleau, 1980)from the caldera rim to downstream of Jemez Springs and up to 25 L/s from Soda Dam, alone (Trainer, 1984). Trainer (1984) and Trainer et al (2000) both note seasonal variability among the total discharge from Soda Dam and time lags in solute fluxes. These increases in solute flux and time lags are inferred to be resultant of transient pressure effects from loading confined conduits during spring melt periods (Trainer et al., 2000). The mode and timing of groundwater recharge from Trainer et al., (2000) corroborates with more recent research from headwater catchments in the Jemez River Watershed (McIntosh et al., 2017; White et al., 2019).

Groundwater-surface water interactions in the Jemez River watershed

Sulphur Springs, Redondo Creek, San Antonio Creek, and the East Fork Jemez River comprise the four main surface water bodies draining the Valles Caldera and confluence in

southwest corner of the caldera rim (Figure 2). At the edge of the caldera rim, the East Fork Jemez River and San Antonio confluence to form the Jemez River. Collectively, these streams drain both thermal and non-thermal groundwater generated streamflow in the upstream portion of the Jemez River (Goff et al., 1985; Szynkiewicz et al., 2019; White et al., 2019). While present, seasonal snowmelt and overland runoff from summer monsoon precipitation are estimated to be relatively low in comparison to groundwater inputs (Liu et al., 2008b, 2008a; McIntosh et al., 2017).

In the upstream portion of the watershed (i.e. within the caldera and near the caldera rim), groundwater is predominately hosted in siliciclastic volcanic extrusive units (i.e. Valles Rhyolite, Bandelier Tuff) and both alluvial and colluvial quaternary deposits primarily sourced from volcanic extrusives (Goff et al., 1992, 2011; Trainer et al., 2000; McIntosh et al., 2017). Emergent springs and subsequent stream baseflow chemistry in the upper watershed within the caldera from non-thermal groundwater are dominated by solutes fluxes characteristic of silicate mineral weathering and exhibit relatively low specific conductance (< 200 μS/cm) (Liu et al., 2008b), although some carbonate derived weathering products (e.g. Ca) are observed (McIntosh et al., 2017). A value of -24.7 ‰ for $\delta^{13}C_{CO2}$ is inferred to be representative of zero order basin soil-respired CO_2 (unpublished data from Tjasa Kanduc in White et al., 2019).

Increasing interactions with limestones in the Madera Group present along the rim of the caldera and in the ring fracture zone (Trainer et al., 2000) yield both groundwater and surface water chemistry shifts towards more carbonate-buffered groundwater compositions (i.e. increased Ca, Mg, HCO3) and presumably, greater DIC loads and higher $\delta^{13}C_{DIC}$ values (Clark, 2018). The Madera Group is the principal formation hosting groundwater for both low-temperature, thermal, and mixed groundwater from the caldera rim to lower elevations (Goff et

al., 1988). Groundwater and surface waters in the ring fracture zone lacking relatively higher temperatures and lower pH values, but elevated CO_2 and SO_4 concentrations have also been interpreted to be indicative of thermal groundwater mixing from vapor upflow, albeit much less in magnitude than Sulphur Springs, comparatively (Vuataz and Goff, 1986; Trainer et al., 2000; Szynkiewicz et al., 2019). Evidence for these inflows also manifest as hydrothermally altered soils at Hummingbird Fumeroles and non-thermal, CO_2-rich springs (Vuataz and Goff, 1986; Trainer et al., 2000).

From the confluence of the East Fork Jemez River, contributions to stream flow and solute loads to the Jemez River are predominately from thermal inflows (i.e. Soda Dam hot springs, Jemez Springs) with minor contributions from artesian 'mineralized' groundwater emergence downstream of Jemez Springs (Trainer, 1974; Trainer et al., 2000). Mineralized, non-thermal artesian springs emerge from subsurface flow through alluvial deposits adjacent to the stream downstream of Jemez Springs upstream of the confluence of the Jemez River and Rio Guadalupe, but also further downstream, as well (e.g. Penasco Springs) and are likely seasonal and strongly affected by evaporative loss (Trainer, 1974).

Methods

Stream sampling and dissolved CO_2 monitoring at sites along the Jemez River and upstream tributaries overlapped with drought conditions that were persistent across the southwestern US (Elias et al., 2019). Snow water equivalent totals within basins feeding the Jemez River were were less than 25 percent 1981-2010 median values from January to May 2018 (Natural Resources Conservation Service, 2018). Discharge during spring and summer months were consistently lower than calculated median values at the Jemez River stream gage

(Station Number 08324000; https://waterdata.usgs.gov/nwis) during the dissolved CO_2 monitoring period. Stream sampling on 11 and 12 July also coincided with the seasonal low-flow period prior to late-summer onset of the North American Monsoon (NAM) in northern New Mexico (Griffin et al., 2013). Coinciding with low snow water equivalents in the basins prior and during the snowmelt runoff season and low-flow sampling prior NAM onset, observed discharge volumes were less than half of typical median values for 11 and 12 July calendar days calculated in the USGS National Water Information System web-interface (https://waterdata.usgs.gov/nwis).

Field-measurements comprised specific conductance, pH, and temperature at sites along the Jemez River and upstream sections (Figure 2). An Apera Instruments (Columbus, Ohio, USA) SX823-B was used for pH, temperature, and SC and was calibrated each morning using buffered reference standards for conductivity at 250 and 750 mS/cm and pH of 4, 7, and 10, respectively. Discrete water samples were collected at 14 of the 16 sites for analysis of DIC and $\delta^{13}C_{DIC}$ analysis. Water was collected from the stream using a peristaltic pump through silicone tubing and passing through a 0.45 micron filter. Water samples were collected into 50 mL exetainer vials capped with a butyl rubber septum and stored at the University of Arkansas Stable Isotope Facility environmental sample storage room until time of analysis. Sites are numbered sequentially from Sulphur Creek site near the National Park Service boundary for the Valles Scenic Preserve. Sites have been loosely grouped based on stream confluences, proximity to known hydrothermal spring emergence, and changes in geology and hydrogeology (Trainer, 1974, 1984; Trainer et al., 2000). These groupings consisted of: 1, upper Sulphur Creek; 2, ring fracture zone to the caldera rim; 3, just upstream of Soda Dam to the Bluffs National Forest Service Recreation Site (BNFS); and 4, San Diego Canyon National Forest Service Recreation

Site to Jemez River U.S. Geological Survey (USGS) stream gage near Jemez downstream of Rio Guadalupe confluence (USGS Station Number 08324000).

Discharge measurements were made using either: 1) simple float method for small, low-discharge streams or 2) Acoustic Doppler Current Profiler (ADCP) for higher discharge. Where discharge was lower than could be assessed using the ADCP, the float method was used following a methodology described by Lowenstern et al. (2012) where stream channel cross-section width and section length were measured using a measuring tape and depths in the stream measured using a ruler. Velocities of the stream were measured using available organic woody debris and a stopwatch. Where stream depths warranted, stream velocities were measured using the 0.6 depth method (Turnipseed and Sauer, 2010) across measured stream profiles. Stream velocity was measured using a Hach (Loveland, Colorado, USA) FH950 velocity flow meter.

Continuous in-situ PCO_2 measurements were made at sites 5, 7, and 16 and were conducted using a low-cost, dissolved CO_2 monitoring platform (CO2LAMP) (Blackstock et al., *in preparation*). Gas analysis of PCO_2 using CO2LAMP is possible by waterproofing and submerging a SenseAir (Delsbo, Sweden) K30 infrared gas analyzer (IRGA). Gas-exchange between the stream and the IRGA headspace was facilitated by a permeable membrane covering a portion of the IRGA (Figure 3). The membrane used in this study was expanded polytetrafluoroethylene, or ePTFE (Product number 1084N86, McMaster-Carr, Douglasville, Georgia, USA). The IRGA was interfaced using an Arduino Uno (https://www.arduino.cc) and data were recorded to a portable memory card using an Adafruit Data shield (Product 1141, Adafruit, New York, NY, USA). Measurements were made approximately every hour; however, operational lifetimes of deployed units varied in the study.

Combined historical hydrochemical and discharge data were downloaded from the National Water Information System from U.S. Geological Survey (USGS) (https://waterdata.usgs.gov/nwis) for site 14 at the Jemez River stream gage. Calculation of DIC, PCO_2, CO_2*, and HCO_3 concentrations were made using CO2calc from paired historical measurements of alkalinity, pH, and stream temperature data (Robbins et al., 2010).

Analysis of total dissolved inorganic carbon and $\delta^{13}C_{DIC}$ were conducted at the University of Arkansas Stable Isotope Facility. Total inorganic carbon was measured using a Shimadzu (Kyoto, Japan) TOC-VCPH/CPN. A set of five standards for instrument calibration and correction were made at 10, 50, 100, 250, and 1000 mg/L DIC through dissolution of 2.125 g of reagent grade potassium hydrogen phthalate and serially diluted. Dissolved inorganic carbon isotope ratios were measured using a Gas Bench II headspace sampler interfaced to a Delta V Advantage Isotope ratio mass spectrometer (Thermo Science, Bremen, Germany). Sample was added to a helium-purged exetainer vial containing 300 µl of H_3PO_4 and the solution was allowed to equilibrate overnight. The resulting CO_2 was sampled four times per sample. The CO_2 peak and the "air" were separated for each injection.

Calculation of CO_2, HCO_3, and CO_3*

Calculations of DIC species were performed using carbonate equilibria relations outlined in Clark (2018). From DIC, pH, and temperature, the concentrations of bicarbonate (HCO_3), CO_2*, and CO_3 can be readily calculated. As salinity for sampled waters varied widely, activity coefficients were derived and applied using the Debye-Huckel equation with the Davies Constant (Clark, 2018):

$$log\gamma_i = \frac{-0.51z^2{}_i\sqrt{I}}{1+0.33\text{å}_i\sqrt{I}} + 0.3I \quad (1)$$

Where z_i is the valence for *i*th species, *I* equals ionic strength, and å equals hydrated diameter, which given the Na-rich saline solutions in the study area (Vuataz and Goff, 1986), a value of 4.0 angstrom units was selected (Clark, 2018). Ionic strength, *I*, was estimated using an empirical relation between ionic strength and specific conductance: *I* = SC x 0.0127 (Griffin and Jurinak, 1973).

From calculated molar activities and assuming an activity of 1 for CO_2* (i.e. dissolved gases are assumed to be at unity), HCO_3, CO_2*, and CO_3 are calculated from derived equilibria relations

$$mHCO_3 = \frac{K_1 \times mDIC}{a_{H^+} \times \gamma_{HCO_3} + K_1} \quad (2)$$

$$mCO_3 = \frac{K_2 \times a_{HCO_3}}{a_{H^+}} \quad (3)$$

$$mCO_2{}^* = \frac{a_{HCO_3} \times a_{H^+}}{K_1} \quad (4)$$

where *mi* equals mol of *i*th species, K_1 is the dissociation constant for CO_2*, a*i* is the activity of *i*th species, γ*i* is the activity coefficient for *i*th species, and K_2 is dissociation constant for HCO_3. Formulation for activities and dissociation constants are adjusted for temperature (Clark, 2018). Calculation of PCO_2 was made using formulation of the Henry's Law between the dissolved concentration of CO_2* and Henry's Law Constant for CO_2 at the given measured water temperature in the field. Combining calculated DIC concentrations and $\delta^{13}C_{DIC}$ of the samples, enrichment factors relative to $CO2_{(g)}$ originally presented by Zhang et al. (1995) with formulation adapted from Campeau et al. (2017) were calculated whereby

$$\varepsilon, bg\ ‰ = HCO_{3(aq)} - CO_{2(g)} = -0.1141 \times T(C°) + 10.78 \quad (5)$$

$$\varepsilon, dg\ ‰ = \varepsilon CO_{2(aq)} - CO_{2(g)} = 0.0049 \times T(C°) - 1.31 \quad (6)$$

$$\varepsilon, dg \text{ ‰} = \varepsilon CO_{2(aq)} - HCO_{3(aq)} = \varepsilon, dg - \varepsilon, bg \quad (7)$$

$$\varepsilon, cg \text{ ‰} = \varepsilon CO_{3(aq)} - CO_{2(g)} = -0.052 \times T(C°) + 7.22 \quad (8)$$

$$\varepsilon, cb \text{ ‰} = \varepsilon CO_{3(aq)} - HCO_{3(aq)} = \varepsilon, cg - \frac{1 + \varepsilon, bg}{1 + \varepsilon, db \times 10^{-3}} \quad (9)$$

Using equations 5 through 9, stream temperature, T (C°), and stream pH, values for $\delta^{13}C_{CO2*}$, $\delta^{13}C_{HCO_3}$, and $\delta 13_{CO_3}$ were then calculated:

$$\delta^{13}C, HCO_3 = \frac{\delta^{13}C, HCO_3 \times [DIC] - (\varepsilon, db \times [CO_2] + \varepsilon, cb \times [CO_3])}{(1 + \varepsilon, db \times 10^{-3}) \times [CO_2] + [HCO_3] + (1 + \varepsilon, cb \times 10^{-3}) \times [CO_3]} \quad (10)$$

$$\delta^{13}C, CO_2 * = \delta^{13}C, HCO_3 - (1 + \varepsilon, db \times 10^{-3}) + \varepsilon, db \quad (11)$$

$$\delta^{13}C, CO_3 = \delta^{13}C, HCO_3 - (1 + \varepsilon, cb \times 10^{-3}) + \varepsilon, cb \quad (12)$$

Notable variability does exist between measured and calculated $\delta 13C_{CO2*}$ (Campeau et al., 2017 and references therein), but even so, relations between calculated $\delta 13C_{CO2*}$ and $\delta^{13}C_{DIC}$ are useful in interpreting pH effects and DIC partitioning (Mayorga et al., 2005; Campeau et al., 2017).

Data analysis

To assess the statistical significance of observed relations between calculated dissolved inorganic carbon, HCO_3, and CO_2* versus discharge, correlation and regresion analyses were carried out for historical USGS data downloaded from NWIS for the Jemez River gage site. Statistical computations were carried out using the PAST software package, version 3.25 (Hammer et al., 2001).

Results

In situ dissolved CO2 measurements

Continuously measured PCO_2 at individual sites at Sulphur Creek (site 5), the Jemez River at Camp Shaver (site 7), and the Jemez River stream gage (site 14) exhibited a relatively wide range of values (Figure 4). However, operational lifetimes of deployed sensors were limited; reliable data-accrual periods were estimated to be approximately 1 week, 3 weeks, and 6 weeks for the Sulphur Creek (site 5), Camp Shaver (site 7), and Jemez River stream gage (site 14), respectively. At all three sites, measured PCO_2 was greater than atmospheric values (~ 400 ppm) reflecting CO_2 supersaturation in the stream.

At the Jemez River stream gage site, PCO_2 and temperature varied exhibited daily fluctuations (Figure 5). Daily variability in PCO_2 at the Jemez River stream gage was typically greater than 100 ppm. PCO_2 lows were typically observed between 0200 and 0800 hours with the greatest PCO_2 values observed between 1400 and 1800 hours. Respective lows and peaks of temperature and PCO_2 were not concomitant.

Chemical variability along the Jemez River

Beginning near the NPS boundary, site 1 exhibited the lowest pH and discharge values in the survey at pH of 2.67 and discharge of 0.99 L/s (Figure 6). DIC was also the lowest of any group, on average, with all values < 3 mg/L C. However, the highest SC values were also observed at site 1 at 2.03 mS/cm and decreased by nearly a factor of 3 by site 3. While $\delta^{13}C_{DIC}$ at site 1 was relatively higher (-11.2 ‰), sites 2 and 3 were the lowest of any site surveyed (-22.7 and -19.9 ‰, respectively). Dissolved carbonate species at these three sites are nearly exclusively CO_2*.

From sites 4 to 7 through the ring fracture zone, pH increased from 4.96 to 8.71. Excluding site 5, discharge also increased nearly two orders of magnitude with the largest increase downstream of the confluence San Antonio Creek between sites 5 and 6. While the lowest DIC value of any location survey was recorded at site 5, DIC concentrations at sites 4, 6, and 7 ranged from 10.1 to 26.1 mg/L–all greater than group 1 concentrations. Correspondent with the increases in pH, DIC speciation shifted towards higher fractions of HCO_3 and CO_3 with distance downstream through the ring fracture zone and caldera rim. Moreover, DIC loads also increased compared to upper Sulphur Creek sites and were predominately HCO_3.

From just upstream of Soda Dam to BNFS (sites 8 through 13) surface waters (site 8 and 9) and hot spring inflows at Soda Dam at Jemez Springs were sampled. Relative to the Jemez River at Camp Shaver (site 7), pH decreased to 7.24 in surface waters upstream of Soda Dam and to pH of 7.04 downstream of Soda Dam. Further downstream, pH in Jemez River increased at site 10 (downstream Buddhist Spring) to 7.72. At BNFS pH further increased to 8.83. From upstream of Soda Dam to site 12, SC values also increased from 0.28 to over 1.01 mS/cm. Discharge slightly increased between upstream and downstream suggesting minor, but measurable contribution of thermal water to stream flow. No discharge measurements were made from the hot springs directly and discharge was not measured at BNFS. However, relative to measured discharge downstream of Soda Dam, discharge only increased 11.9 L/s downstream of Soda Dam and a further 3.9 L/s at Las Casitas (site 13). Similar to sites 6 and 7, DIC loads are dominated by HCO_3 species. However, total DIC and CO_2* loads increased by a nearly a factor of 2 between upstream and downstream of Soda Dam. However, at Site 14 at the Bluffs, CO_2* was much lower, but similar loads of HCO_3 were observed.

From San Diego Canyon to the Jemez River stream gage (sites 12 to 14), pH remained >8 showing a only small increase at the Jemez River stream gage from 8.71 at 8.75. SC values also remained around ~ 1 mS, but a decrease to 0.9 mS/cm downstream of the Rio Guadalupe confluence at the Jemez River stream gage was measured. DIC concentrations and $\delta^{13}C_{DIC}$ compositions remained above 70 mg/L and isotopically higher (> -5 ‰). Notably, the highest $\delta^{13}C_{DIC}$ value in the survey was observed at Las Casitas at 0.78 ‰. DIC species were predominantly HCO_3 and CO_3 and constituted the highest concentrations of CO_3 seen in the survey. DIC loads decreased slightly from downstream of Soda Dam to Las Casitas from 22.8 to 20.9 g/s despite the slight increase in discharge, but increased to 23.0 g/s after the Rio Guadalupe confluence. Calculated CO_2* loads were less than 1 g CO_2*/s with the DIC yield > 99 % HCO3 (~116 g HCO_3/s).

Relations between pH, DIC species, and $\delta^{13}C_{DIC}$

In the Keeling plot, a general pattern emerges whereby spatial groupings tended to cluster in distinctive areas; albeit with considerable overlap (Figure 7). Upper Sulphur Creek values exhibit higher 1/DIC values (i.e. low DIC concentrations) and lower $\delta^{13}C_{DIC}$ compositions. Samples along the ring fracture zone values plotted between the upper Sulphur Creek sites, Soda Dam to BNFS sites, and San Diego Canyon to Jemez River stream gage sites. Ring fracture zone sites had slightly lower DIC concentrations and lower $\delta^{13}C_{DIC}$ values than all other downstream sites, but greater DIC concentrations and higher $\delta^{13}C$ values than upstream upper Sulphur Creek sites. Significant overlap was observed among sites 8 to 14. For all sampled waters, the greatest DIC values are observed for Soda Dam and Buddhist Spring thermal waters, which plot just to the left of sites 8 to 14.

Observed concentrations between CO_2* mg/L versus HCO_3 mg/L and calculated CO_2* and HCO_3 loads yielded four distinct clusters (Figure 8). Upper Sulphur Creek sites were lower in HCO_3 (< 0.1 mg/L), but elevated in CO_2* (~ 10 mg/L), however, calculated loads of CO_2 and HCO_3 were the lowest among all site groupings. Hot springs displayed the greatest HCO_3 and CO_2* concentrations (~ 800 and 1000 mg/L for CO_2* and HCO_3, respectively). Total loads of CO_2* and HCO_3 from hydrothermal inputs were not assessed in this study. Sites that consisted of San Diego Canyon to the Jemez River gage site exhibited high HCO_3 concentrations, but relatively lower CO_2* concentrations (~ 1 mg/L). Despite lower concentrations than Upper Sulphur Creek for CO_2*, HCO_3 and CO_2 loads were higher than Upper Sulphur Creek sites. Soda Dam to BNFS sites exhibited the greatest CO_2* concentration and loads of any surface water sites. Sites associated with the ring structure and caldera rim plotted intermediary to the aforementioned clusters. Notably, sites 4 and 5 in the ring fracture were closer in concentration and calculated load values to Sulphur Creek sites. However, the caldera rim sites of 6 and 7 were most similar in CO2* and HCO3 loads as the San Diego to Jemez River stream gage sites (Figure 8B).

Relations between pH versus $\delta^{13}C_{DIC}$ and $\delta^{13}C_{DIC}$- $\delta^{13}C_{CO2}$ in surface waters are complex and best described by station to station variation. From sites 1 to 2, $\delta^{13}C_{DIC}$ decreased from -11.2 to -22.8 ‰, but pH increased slightly from 2 to 3 (Figure 9A). From sites 2 to 7 pH increases covaried with more positive $\delta^{13}C_{DIC}$ values (Figure 9B). As $\delta^{13}C_{DIC}$ becomes more positive, $\delta^{13}C_{CO2}$ values become more negative from sites 2 to 6, but a positive shift is observed in $\delta^{13}C_{CO2}$ from Site 6 to 7 (Figure 10B). From sites 8 to 10, pH decreases and values plotted near the thermal spring values (~ pH 6.5) and $\delta^{13}C_{DIC}$ values were higher. Similarly, $\delta^{13}C_{CO2}$ and $\delta^{13}C_{DIC}$ was higher from Sites 8 to 10. Downstream of BNFS, sites 13, 15, and 16 cluster between pH of

8 and 9. Values for $\delta^{13}C_{DIC}$ ranged between -3 and 1 ‰. Correspondingly, $\delta^{13}C_{CO2}$ values at sites 13, 15, and 16 ranged from -9.1 to -10.6 ‰ and overlap with site 9 and 10.

Calculated DIC loads—trends through time

Using available discharge and hydrochemical data available at the Jemez River stream gage site, CO_2* and HCO_3 concentrations and loads were calculated for 74 paired measurements spanning 1980 to 2005. Discharge at the Jemez River stream gage varied over nearly two orders of magnitude from 0.2 m^3/s to 11 m^3/s for the data available. Concentrations of HCO_3 ranged from 36.8 to 126.6 mg/L and, overall, decreased with discharge (log-log slope = -0.1, $p << 0.05$; figure 10A). However, CO_2* concentrations exhibited a small, but significant concentration increase with discharge (log-log slope = 0.23, p << 0.05; Figure 10B). Concentrations of CO_2* ranged from 0.22 to 4.7 mg/L.

Significant power law relations were observed between both DIC yield and discharge (r^2 = 0.89, p <<< 0.05; Figure 11A) and CO2* yield and discharge (r^2 = 0.76, p <<< 0.05; Figure 11B). Calculated loads varied over an order of magnitude for DIC ranging from 3.8 to 273 g/s and two orders of magnitude for CO_2* ranging from 0.1 g/s to 47 g/s.

Binning measurements by month, the greatest loads for DIC and CO_2* are observed during early spring (March to May) with a slight increase in November during some years (Figure 12). The lowest loads of calculated DIC and CO2* were observed during August, September, and February. For both DIC and CO_2*, loads sharply increased from February to March followed by another sharp decrease from May to June. Paired discharge, alkalinity, and pH measurements were not available for January at the Jemez River stream gage to estimate DIC and DIC species and calculate loads.

Discussion

Variability DIC chemistry and loads along the Jemez River

The variability of pH, DIC, $\delta^{13}C_{DIC}$ compositions and other measured parameters along the Jemez River present a complex DIC evolution reflective of variable sources, in-stream processes, and physical hydrologic variability. No one parameter from this dataset was adequate in describing potential causes of chemical variability. Moreover, observed shifts in values for individual parameters can be indicative of multiple processes (e.g. CO_2 degassing from the stream, surface-groundwater mixing). To overcome the inadequacies of individual indicator parameters, a multiple parameter approach was used to elucidate primary factors affecting stream chemistry in a 'step-wise' fashion along the Jemez River.

Sulphur Springs acid-sulphate contributions

Condensing steam and CO_2-rich gas at Sulphur Springs (~ 0.5 km upstream of site 1) form a highly acidic water with minor amounts of H_2S; this defines the acidic, hydrothermal groundwater end-member used for mixing analysis (Figure 6 and 13). Sulphur Springs water is a major source of acidity in Sulphur Creek (Goff and Janik, 2002), which becomes super saturated with CO_2* (> 90 % CO_2 near Sulphur Springs) upon mixing with the acidic-hydrothermal inflows.

From Sulphur Springs to Site 2

From Sulphur Springs to site 1, much of the hydrothermal-derived CO_2 is likely degassed. High CO_2 stream emissions have been shown to shift $\delta^{13}C_{DIC}$ to higher values due to fractionation of C at the water-air boundary (Doctor et al., 2008; Campeau et al., 2017), values equal to or higher than previously measured $\delta^{13}C_{DIC}$ at Sulphur Springs of ~ -4 ‰ (Goff and

Janik, 2002) would be expected at site 1. However, measured $\delta^{13}C_{DIC}$ at site 1 was -11.2 ‰. Furthermore, from site 1 to 2, DIC, CO_2*, and $\delta^{13}C_{DIC}$ values all decreased by nearly a factor of two (Figure 7). Stream discharge did increase from site 1 to 3, presumably from groundwater baseflow contributions (Liu et al., 2008b; McIntosh et al., 2017) as there was minimal snowpack in July 2018.

Surface waters downstream of Sulphur Springs were interpreted to be mixing with the previously described soil-CO_2 equilibrated siliciclastic-hosted groundwater (Liu et al., 2008a; McIntosh et al., 2017), which resulted in lowering of the $\delta^{13}C_{DIC}$ values from site 1 to 2 from -11.2 to -22.8 ‰. As the low-temperature groundwater inside the caldera rim proximal to Sulphur Creek is hosted primarily in siliciclastic formations with low-carbonate content, acid buffering capacity of this groundwater water is negligible. Meaning, groundwater contributions from the siliciclastic aquifers to stream flow, if present, would have minimal effect raising stream pH. However, as DIC and $\delta^{13}C_{DIC}$ of groundwater from the siliciclastic formations are primarily sourced from soil-CO_2 production (-24.7 ‰; White et al., 2019 and references therein), $\delta^{13}C_{DIC}$ will be lower resultant from siliciclastic-hosted groundwaters contributions to streamflow.

Stream chemistry evolution from Upper Sulphur Creek through the ring fracture zone

Overall, increases in pH, DIC concentrations, $\delta^{13}C_{DIC}$, discharge, and DIC loads were observed between sites 2 and 7 are interpreted to represent increasing contributions of groundwater from carbonate buffered groundwater hosted in the Madera Group aquifers (Figures 13 and 14) to surface waters. Previously reported low-temperature groundwater major ion chemistry from the ring fracture zone and caldera rim in San Diego Canyon corroborate the presence and increasing contributions of carbonate buffered groundwater from the Madera group limestones (Vuataz and Goff, 1986; Trainer et al., 2000; Szynkiewicz et al., 2019). Relations

between CO_2* and HCO_3 concentrations suggested possible contributions from a pH-neutral thermal end-member (Figure 13), but this was not apparent from the pH- $\delta^{13}C_{DIC}$ and $\delta^{13}C_{CO2}$-$\delta^{13}C_{DIC}$ relations (Figures 13 and 14).

Upstream of Soda Dam to the Jemez River stream gage: significant hot spring inflows

From upstream of Soda Dam to the Jemez River stream gage (S16), DIC loads increase by nearly a factor of 2 with this change occurring between the upstream and downstream sites relative to Soda Dam (sites 8 and 9). Notably, while HCO_3 loads are similar are among sites 6 and 7 near the caldera rim and downstream at the Las Casitas and Jemez River gage sites, CO_2* loads upstream and downstream of Soda at sites 8 and 9 are an order of magnitude greater (Figure 13).

The decrease in pH and increased CO_2* concentration and loads observed at the sampling location upstream of Soda Dam suggest potential thermal inflows are present further upstream of site 8. However, these inflows are more likely vapor dominated versus thermal water given specific conductance did not increase between site 7 and 8 (Figure 6). Hummingbird fumaroles, ~ 1 km upstream of Soda Dam and just downstream of site 6 is a potential source of CO_2 upflow to the stream as steaming ground and acidified soils resulting from focused thermal vapor upflow are noted at the site. As hydrothermal groundwater circulates to spring and seep outlets near Soda Dam, some proportion of CO_2 may exsolve from the hydrothermal plume and re-dissolve into the Jemez River, explaining the increase in DIC, specifically CO_2*, reduction in pH, but no increase in SC.

Water chemistry and discharge-measurement sampling spacing used in the study leaves CO_2* contributions to the Jemez River by Buddhist Spring in the Jemez Springs area uncertain.

At BNFS, higher CO_2* concentrations were much lower than those observed for sites 8 and 9 near Soda Dam (Figure 13A). If CO_2* was simply converted to HCO_3, similar DIC loads might be expected at site 13 at Las Casitas (Figure 13B). However, measured DIC loads slightly decreased from 22.7 downstream of Soda Dam to 20.9 g/s at Las Casitas. The decrease in DIC and CO_2*, but increase in pH from Soda Dam to Las Casitas, suggests much of the CO_2* from thermal inflows at Soda Dam and Jemez Springs are likely degassed before BNFS.

As an increase in discharge but decrease in DIC loads is observed, the Jemez River is likely diluted by a relatively lower-DIC groundwater contribution from adjacent alluvial deposits (Trainer et al., 2000). As $\delta^{13}C_{DIC}$ values recorded at sites 10, 13, and 14 do not plot outside the range of limestone $\delta^{13}C$-values (i.e. higher than -4 ‰), estimated groundwater contributions from adjacent alluvial deposits and surface water from Rio Guadalupe River are considered to be to be carbonate buffered as previously inferred from major ion chemistry by Trainer et al. (2000).

Tracing DIC sources in hydrothermal watersheds

DIC sources to the Jemez River are inferred to comprise four definitive end-member compositions. These include the two thermal components: The acidic, vapor-dominated, acid-sulphate waters (e.g. Sulphur Springs) and the pH-neutral thermal-water inflows; and two lower-temperature groundwater components: Soil-CO_2 equilibrated non-carbonate buffered groundwater and carbonate-buffered groundwater (Figures 13 and 14). Mixing between thermal and lower temperature groundwater has been reported to be prevalent in the subsurface along the rim fracture zone, caldera rim, and beneath the Jemez River (Trainer, 1974; Vuataz and Goff, 1986; Vuataz et al., 1988; Trainer et al., 2000), but estimating the degree of mixing, conductive cooling, and flow paths of thermal water in the subsurface remain uncertain except where large CO_2* concentrations and loads were measured.

In the geothermal reservoir, inorganic carbon likely comprises carbon derived from magmatic degassing and high-temperature water-rock interactions with Madera group limestone and similar carbonate-laden lithologies at depth (Truesdell and Janik, 1986; Vuataz and Goff, 1986; White, 1986; Goff and Janik, 2002). Assuming a magmatic end-member $\delta^{13}C$ value close to -7 ‰ (Gerlach, 1980; Giggenbach, 1995; Martini, 1996; Goff and Janik, 2002; Lowenstern et al., 2015) and a carbonate end-member $\delta^{13}C$ of approximately 0‰ for the Madera group (Goff et al., 1985), these fluids are compositionally distinct at their respective sources. However, subsequent mixing in the geothermal reservoir and during ascent to the surface obfuscates these 'source' signatures before fluids are discharged at the surface (Goff et al., 1985; Goff and Janik, 2002).

In the near-surface environment, DIC speciation and $\delta^{13}C_{DIC}$ values for 'mixed' hydrothermal fluids are more compositionally determined by temperature-pH equilibria, driven, in part by CO_2* (Figure 14). Deconvolving specific inputs from either magmatic and decarbonation are not possible with currently available data, but should be possible using a broader assay of gas and solute geochemistry (Crossey et al., 2009; Banerjee et al., 2011; Lowenstern et al., 2015). Collectively, export of DIC in the form of CO_2* and HCO_3 from the geothermal reservoir and dissolved from limestones in the Jemez River watershed represent a regionally important source of inorganic C, particularly HCO_3, to the downstream Rio Grande River. If the total CO_2* load is assumed to be degassed as CO_2 between downstream of Soda to Las Casitas, this constitutes a stream CO2 flux of ~ 18 g/s. Scaling this estimate up, daily CO2 emissions between Soda Dam and Las Casitas may be near 1 kton CO_2/day.

Increased hydrothermal inflows during higher groundwater recharge periods

While somewhat speculative in the absence of other geochemical indicators to distinguish between low- and high-temperature groundwater (e.g. Cl, Na, SO4, B), some general considerations and inferences are warranted regarding interrelations between climate, groundwater, and DIC transport. As groundwater recharge in the caldera is primarily restricted to winter months (McIntosh 2017), movement of water from the vadose to saturated zone (i.e. contributing to groundwater recharge) and subsequent increase in baseflow coincide with late winter and early spring (White et al., 2019). In combination with increased streamflow from snowmelt, these two sources are the primary components of streamflow along the Valles Caldera (Liu et al., 2008b, 2008a).

If thermal mixing is pervasive, higher baseflows could yield greater hydrothermal inflows to surface waters and, in turn, greater advective transport of DIC from groundwater to surface waters. As previously stated, the degree of mixing between shallow, low-temperature and high-temperature groundwater is not well understood. However, seasonally higher groundwater levels (Trainer et al., 2000) will yield higher potentiometric gradients and with increased hydraulic gradients and drive greater vertical and lateral fluid movement in hydrothermal systems (Harvey et al., 2015).

Historical data show that HCO_3 concentrations slightly decrease with discharge, but with higher discharge, CO_2* concentrations also increase (Figure 11). Meaning, CO2 loads are not chemostatic within the basin (Godsey et al., 2009). Moreover, CO_2* and HCO_3 both exhibit greater load with increased discharge at the Jemez River stream gage (Figure 12). Maximums in load are coincident with higher groundwater baseflows in spring months. Interestingly,

calculated HCO_3 and CO_2* concentrations plot within the bounding end-members of CO_2*-HCO_3 space (Figure 15A).

Discharge could, in turn, be interpreted as primarily derived from low-temperature carbonate buffered groundwater. However, historical CO2* and HCO3 loads in the Jemez River plotted between the low-temperature, carbonate buffered groundwater in an upward trend converging on values similar to those near Soda Dam (15B). While the Soda Dam loads measured in July 2018 are not considered an end-member, the highest loads of CO2* and HCO3 at the Jemez River are coincident with spring months and CO2*-HCO3 load values similar to known hydrothermal inorganic carbon sources to surface waters.

Hydroclimatic modulation of carbon fluxes

Greater baseflow contributions to streamflow are resultant from greater groundwater recharge from snowmelt and lead to greater discharge volumes in the Jemez River (Trainer, 1974; Erikson, 1977; McIntosh et al., 2017). Greater discharge is also coincident with a concomitant increase in CO_2 loads at the Jemez River stream gage (Figures 10-12). As streamflow is:1, primarily generated from groundwater contributions from hydrothermal and non-thermal sources (McIntosh et al., 2017; White et al., 2019); and 2, observed to have greater hydrothermal inflows during higher streamflow periods (Trainer, 1984; Trainer et al., 2000), it is postulated that groundwater recharge directly modulates the advective inorganic carbon flux at the Valles Caldera.

The described process may be considered analogous to 'groundwater scrubbing' on active volcanoes (Caracausi et al., 2005; Marini and Gambardella, 2005; Werner et al., 2012; de Moor et al., 2015) whereby downward migrating groundwater dissolves degassed volatiles

during circulation. Subsequently, groundwater discharges dissolved volatiles at lower elevation at spring emergences along volcanic flanks. Such an interpretation is consistent with available data but is far from unequivocal.

To illustrate this groundwater-climate feedback, where permeability in the subsurface is sufficient for CO_2 migration in the gas phase and circulating groundwater does not 'scrub' CO_2, the flux of CO_2 from lithospheric sources will be primarily through near-surface media (e.g. soil, rock fractures). However, given ample groundwater recharge and groundwater circulation rates in the crust, transport of inorganic carbon from lithospheric sources may dominantly occur as by advective transport of CO_2 and HCO_3 (converted from CO_2). As CO_2 will readily dissolved into relatively colder, high-altitude groundwater, this feedback is likely more pronounced and prevalent in high-relief environments such has calderas and stratovolcanoes. Predominance of either diffusive CO_2 emissions at the surface or advective transport of CO_2 from lithospheric sources (i.e. volcanoes, hydrothermal areas, orogenic metamorphic environments) is therefore inextricably linked not only with subsurface permeability, but long-term climatic and groundwater recharge and circulation.

Conclusions

As published $\delta^{13}C_{DIC}$ data are limited for groundwater outside Sulphur Springs and deeper geothermal wells (Goff et al., 1985; Truesdell and Janik, 1986; Goff and Janik, 2002), this study comprised the first longitudinal transect and analysis of inorganic carbon abundance and stable carbon isotope geochemistry surface waters along ~40 km stream reach of the Jemez River watershed. Considering the range of daily variability of PCO_2 in the Jemez River, future

sampling should consider the timing of water sample collection not only for DIC, but effects PCO_2 may impart on pH and other dissolved solutes (e.g. Ca).

At the watershed scale, longitudinal variability of DIC and $\delta^{13}C_{DIC}$ exhibited general trends that were explained by lithologic differences in aquifers and the presence of thermal groundwater inflows. From groundwater end-member designation and analysis of historical loads of CO_2* and HCO_3, hydrothermal DIC components have been shown to potentially constitute a large fraction of inorganic C fluxes. However, incorporation of other trace element data are needed to verify seasonality of hydrothermal inputs. Ultimately, seasonal differences and the magnitude of hydrothermal groundwater end-members contributions to surface waters may potentially be underestimated to the larger Rio Grande River watershed and in other geothermal areas, globally.

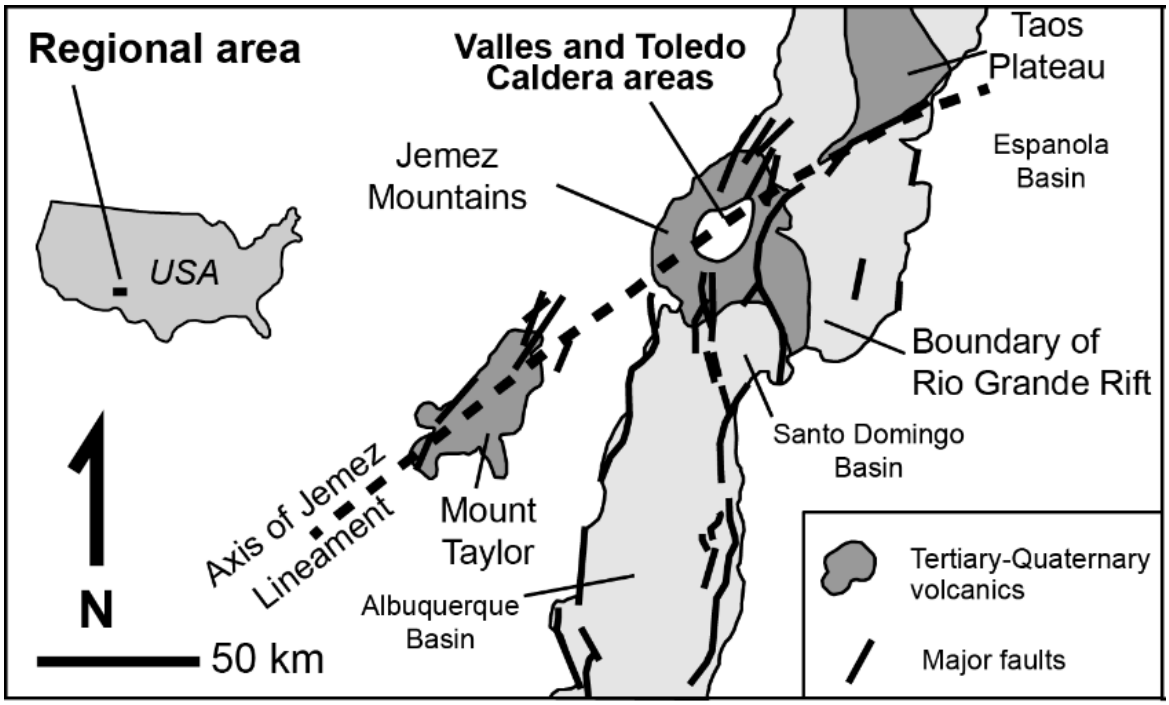

Figure 1. Regional location map of Valles Caldera (New Mexico) in relation to Jemez Lineament and Rio Grande Rift. Tertiary-Quaternary volcanics and Rio Grande associated basin are shown (Goff et al. 1994).

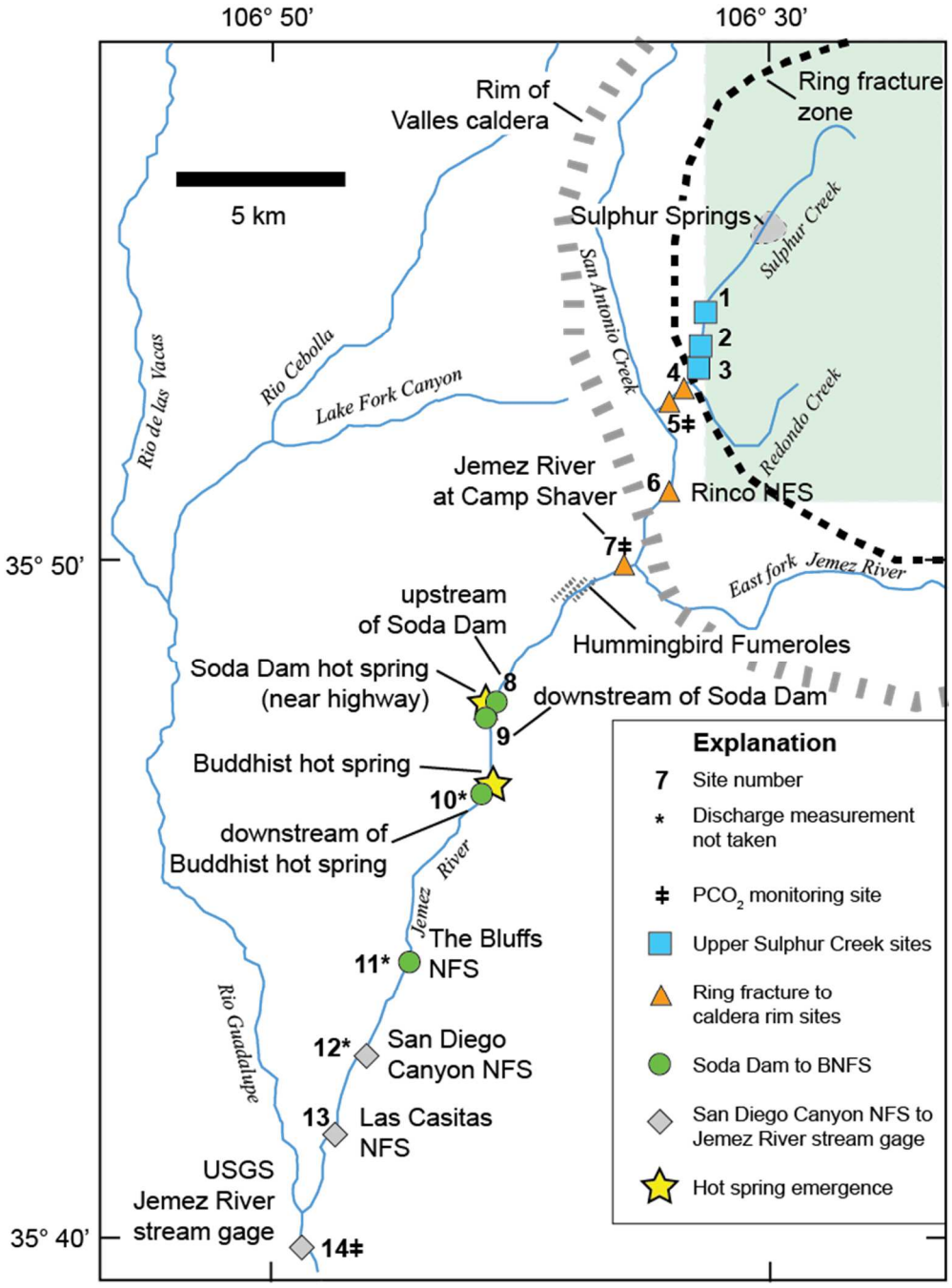

Figure 2. Site numbers and spatial groupings along the Jemez River and headwater tributaries.

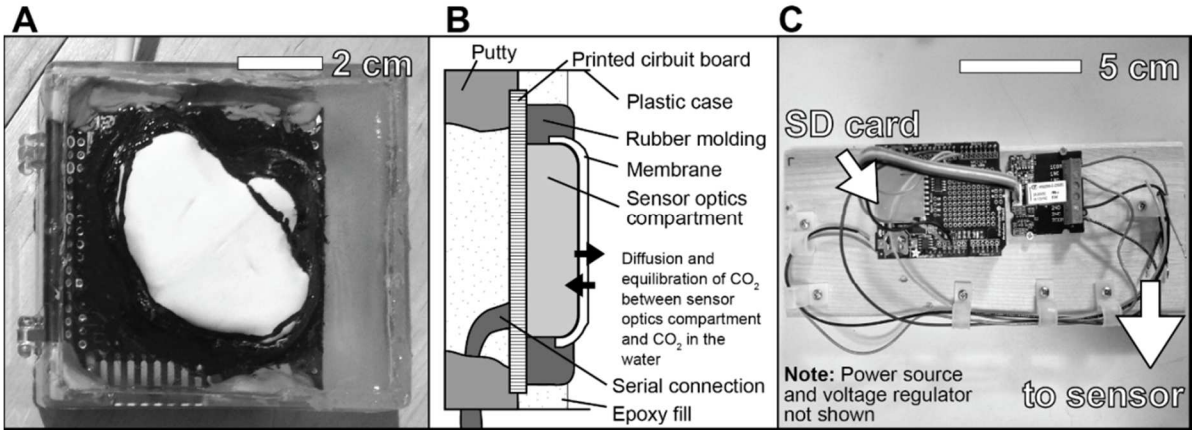

Figure 3. A) Photograph of CO_2 gas analyzer. White area is the semi-permeable membrane. **B)** Schematic cross-sectional view of waterproofing and construction components. **C)** Data logging components consisting of Arduino Uno, data logging shield, and relay switch for power cycling.

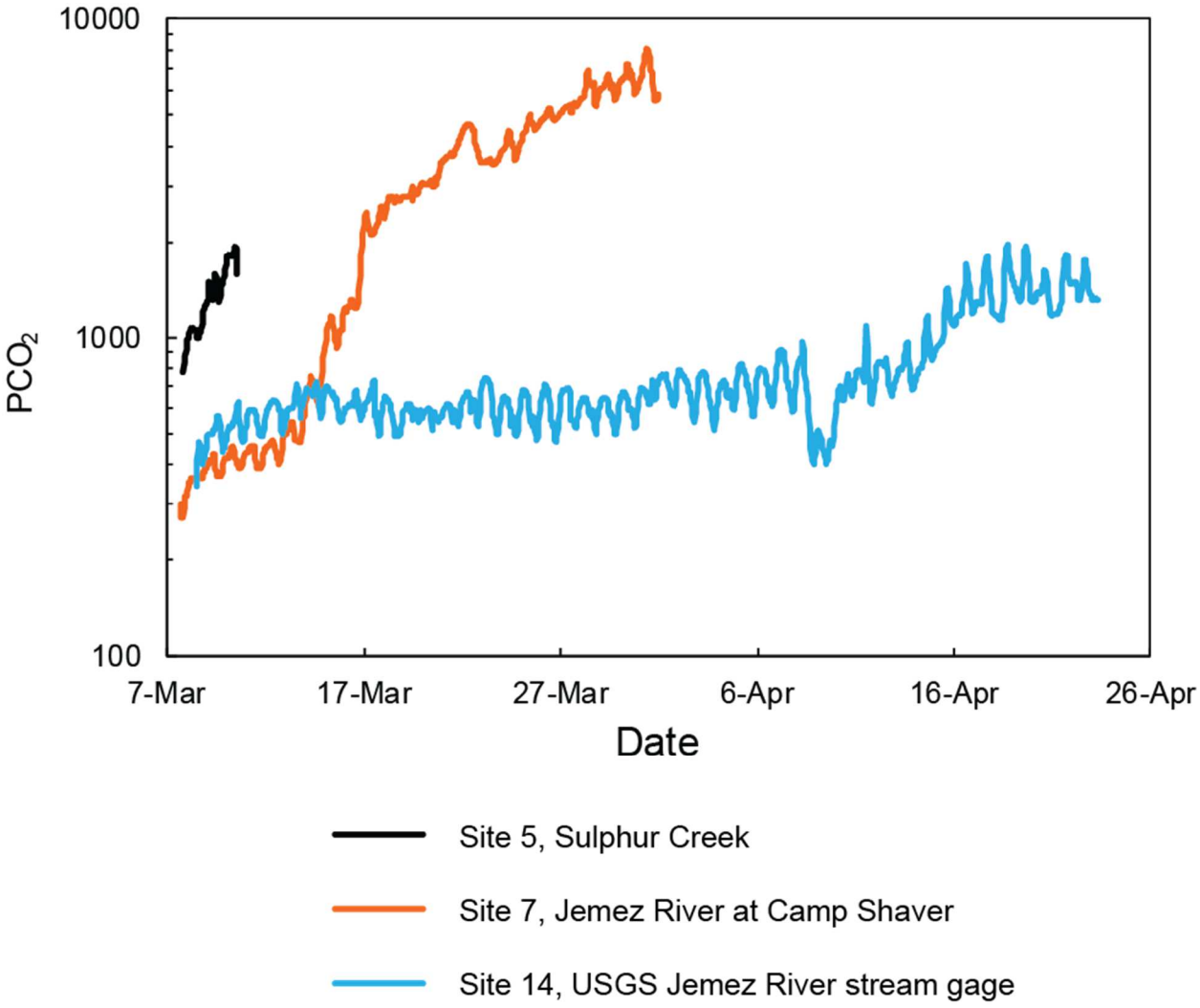

Figure 4. PCO_2 variability at sites 5, 7, and 14 along the Jemez River and upstream tributary Sulphur Creek.

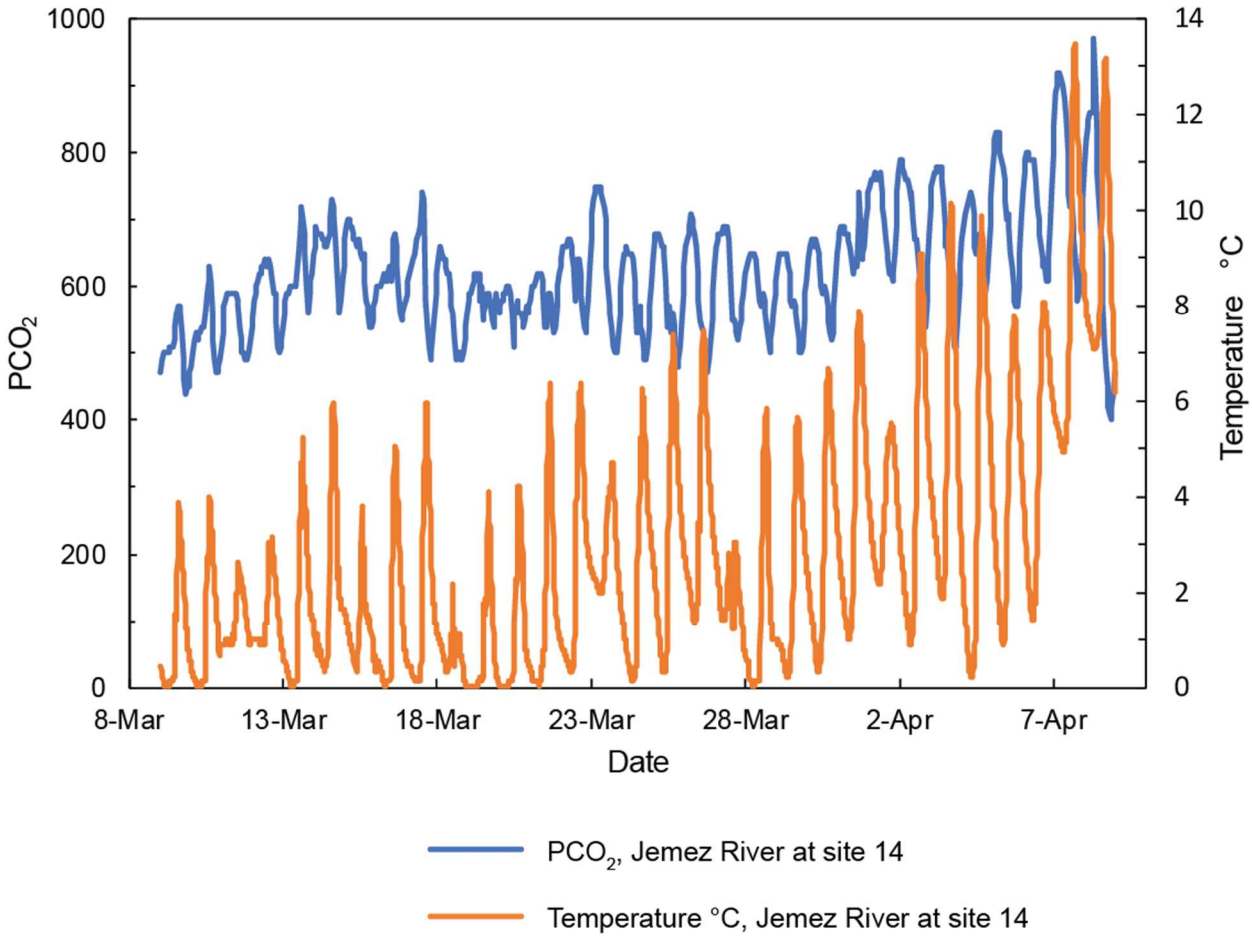

Figure 5. PCO_2 variability (blue) and temperature (orange) recorded at Jemez River stream gage (site 14) from March 9 to April 9, 2018.

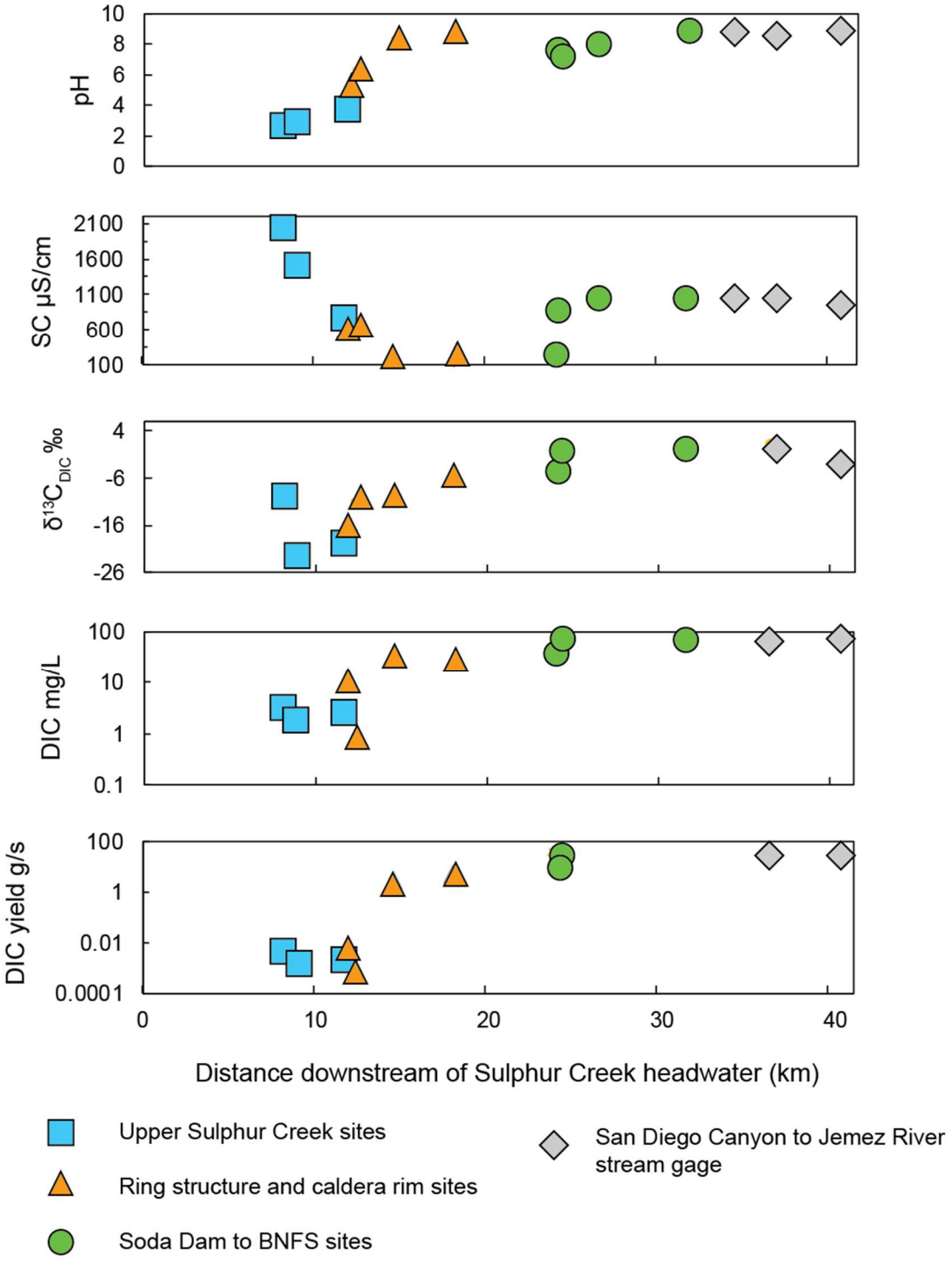

Figure 6. Longitudinal variation of pH, specific conductance (SC), $\delta^{13}C_{DIC}$, DIC concentration (mg/L), and DIC loads (g/s) downstream of Sulphur Creek headwater in Alamo Canyon (central Valles Caldera).

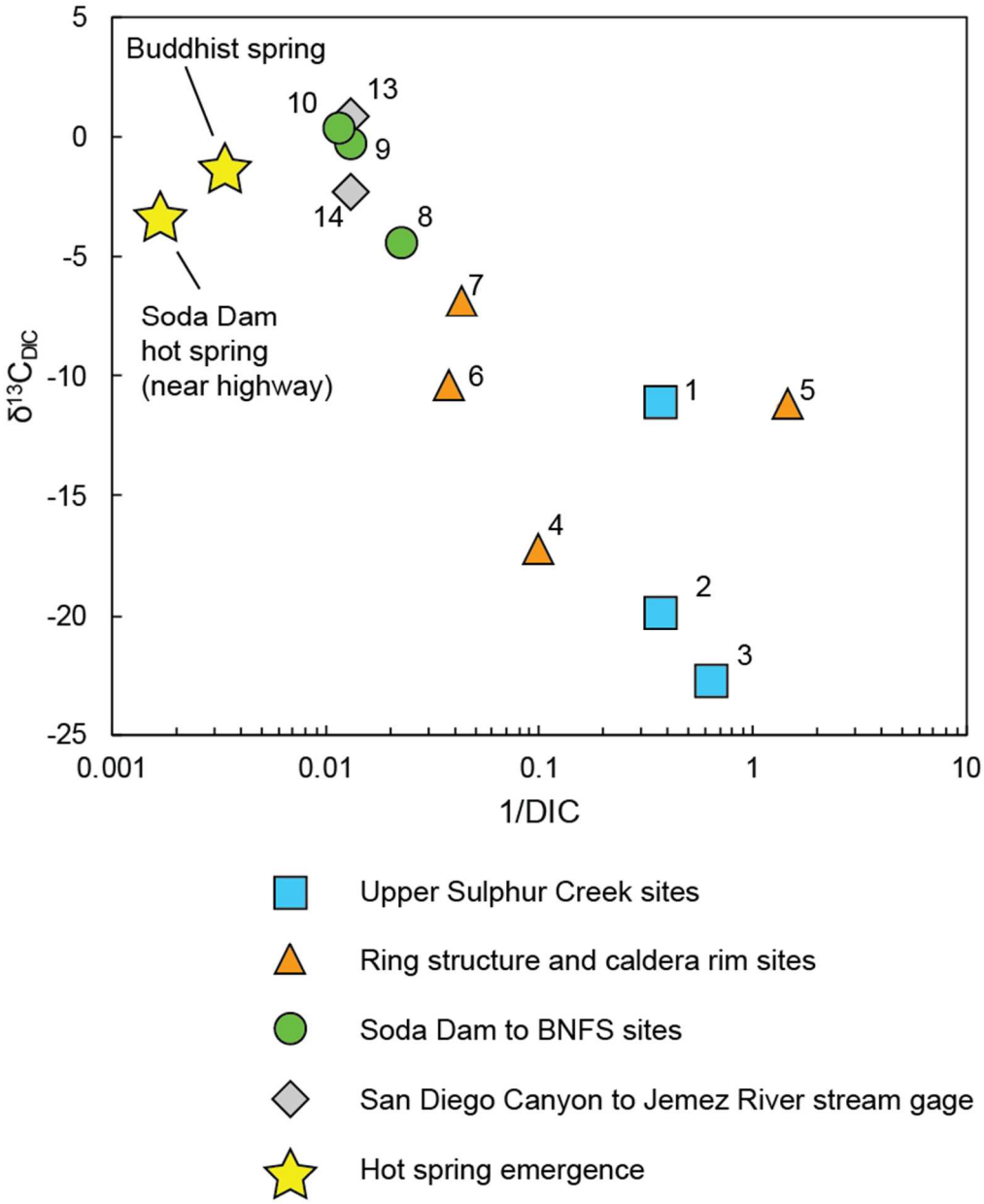

Figure 7. Keeling plot of $\delta^{13}C_{DIC}$ versus 1/DIC for upper Sulphur Creek, Ring structure to caldera rim, Soda Dam to BNFS, and San Diego Canyon to Jemez River stream gage sites. Star symbols are for roadside thermal spring at Soda Dam and Buddhist Spring at Jemez Springs.

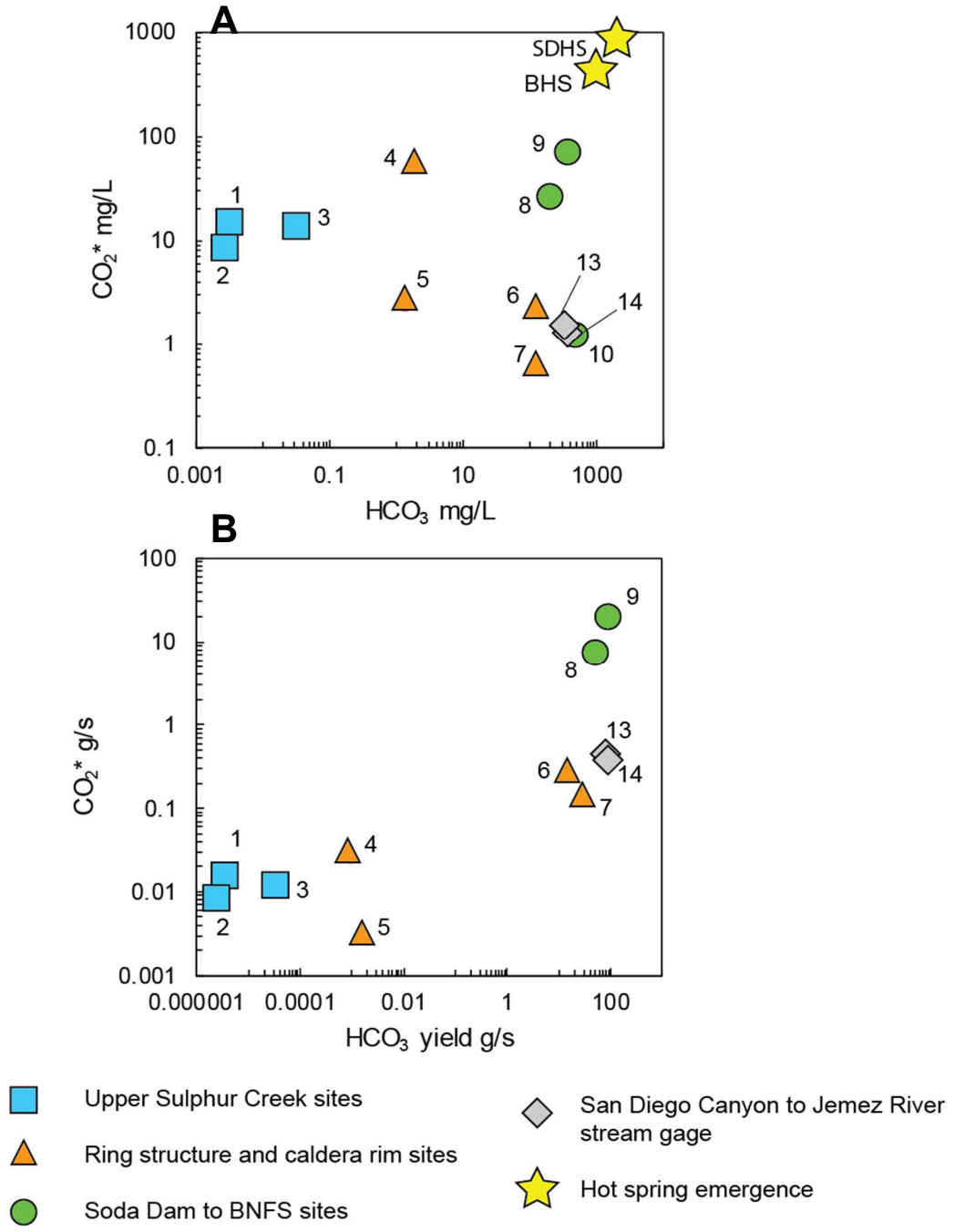

Figure 8. A) CO_2* versus HCO_3 concentrations (mg/L) and **8B)** CO_2* versus HCO_3 yield (g/s) for upper Sulphur Creek, Ring structure to caldera rim, Soda Dam to BNFS, and San Diego Canyon to Jemez River stream gage sites. Star symbols are for roadside thermal spring at Soda Dam and Buddhist Spring at Jemez Springs.

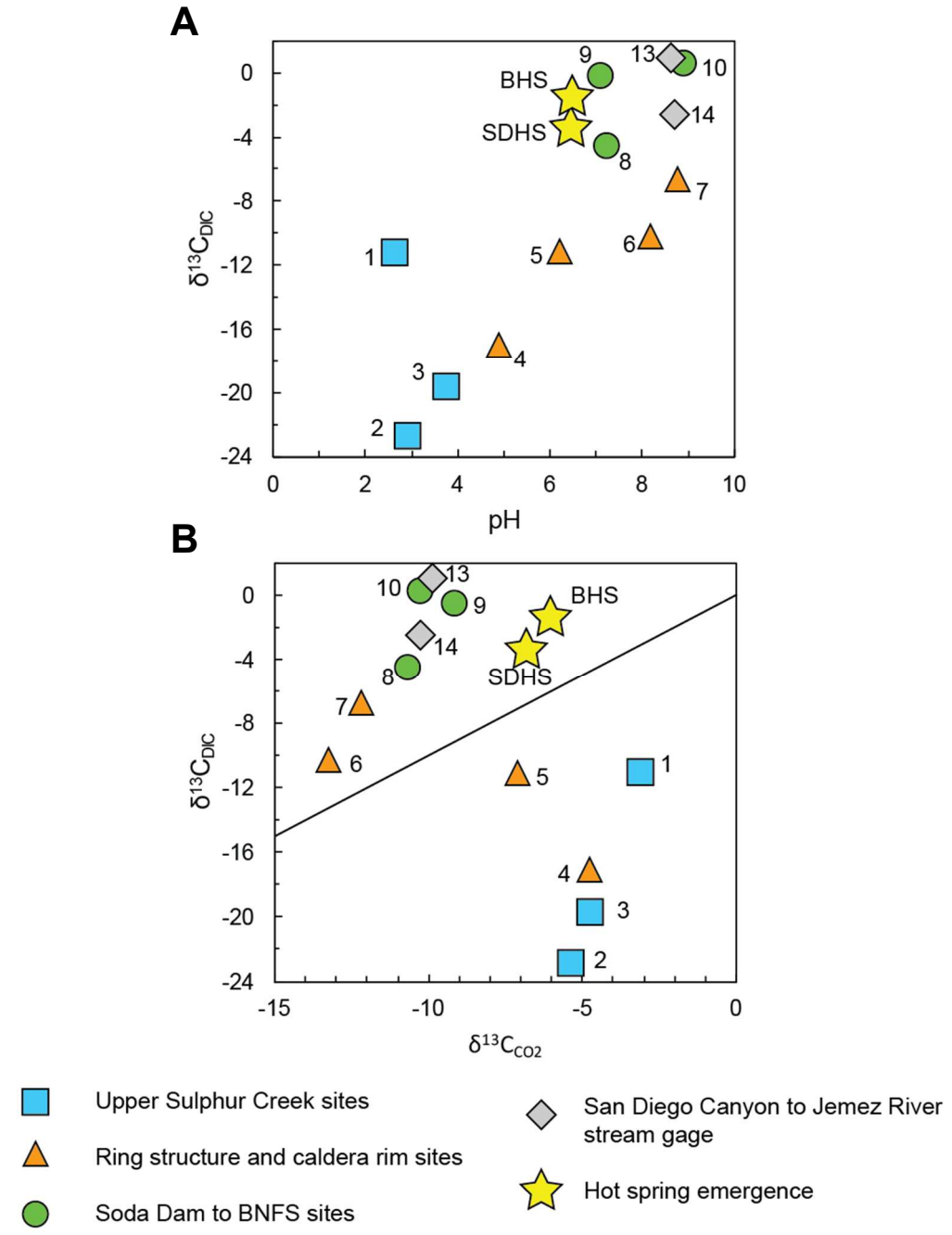

Figure 9. A) $\delta^{13}C_{DIC}$ versus pH and **9B)** $\delta^{13}C_{DIC}$ versus $\delta^{13}C_{CO2}$ for upper Sulphur Creek, Ring structure to caldera rim, Soda Dam to BNFS, and San Diego Canyon to Jemez River stream gage sites. Star symbols are for roadside thermal spring at Soda Dam and Buddhist Spring at Jemez Springs. Solid black line represents 1:1 line.

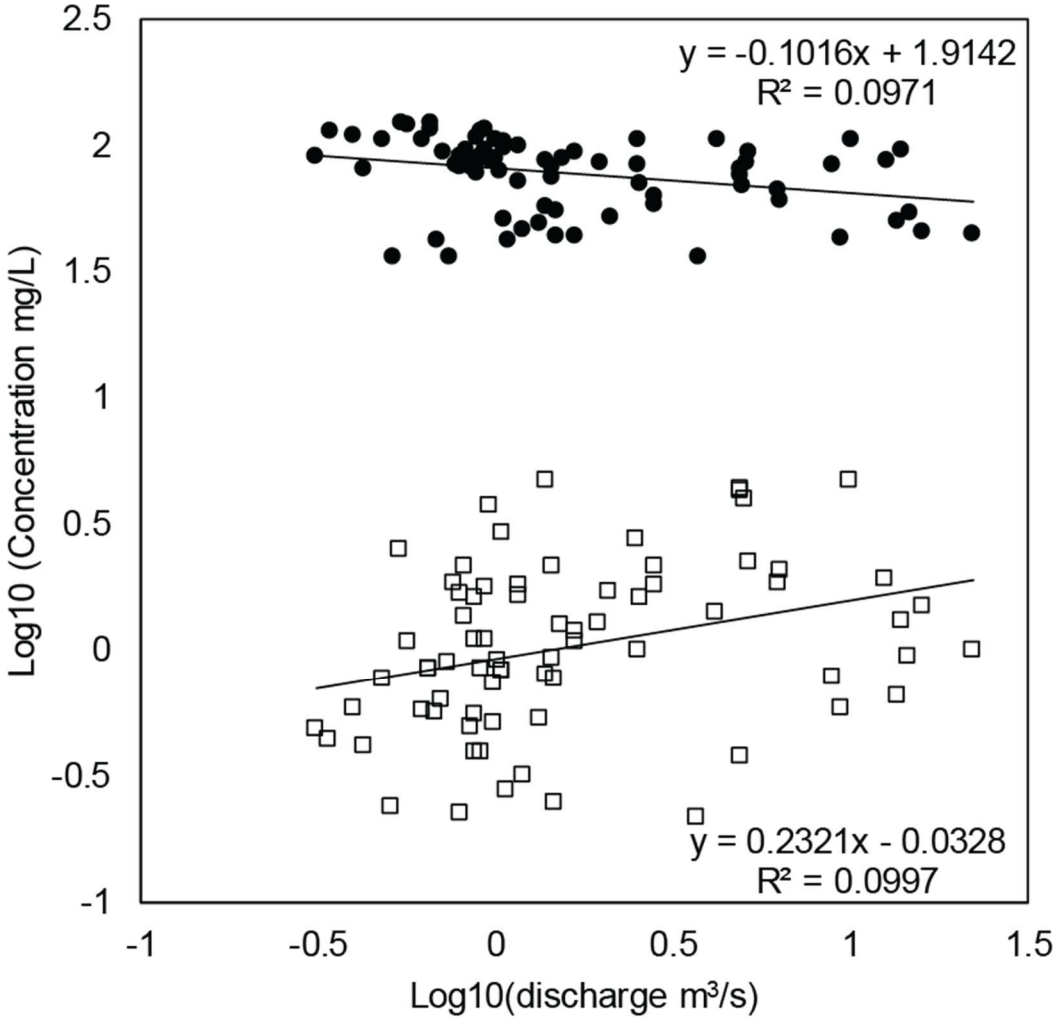

Figure 10. Log-transformed values of concentration for HCO_3 (black filled circles) and CO_2* (open-faced squares) versus discharge, m^3.

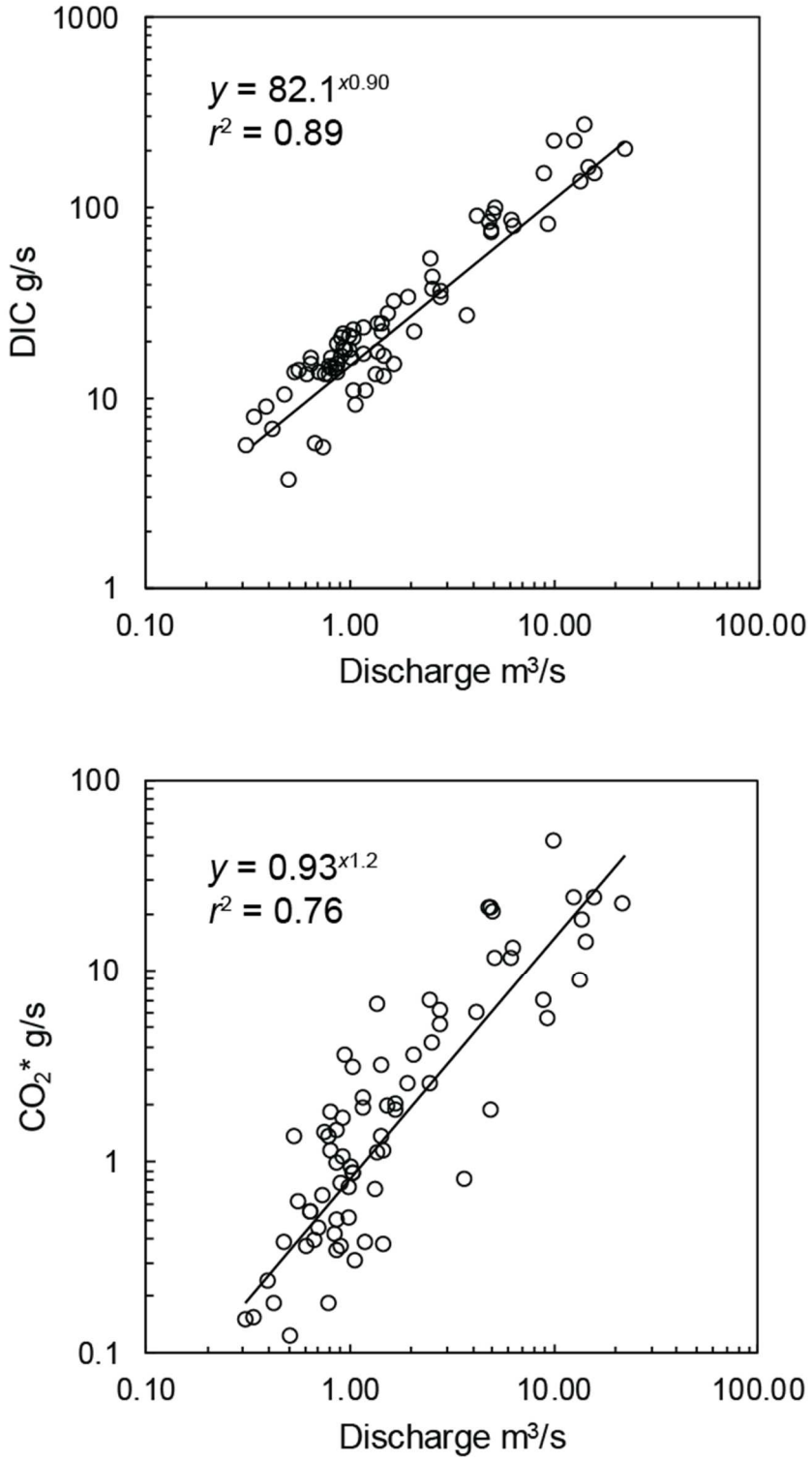

Figure 11A) DIC yield (g/s) versus measured discharge m^3/s versus calculated at Jemez River stream gage using available data from USGS-NWIS. **B)** CO_2* yield (g/s) versus discharge m^3/s versus calculated at Jemez River stream gage.

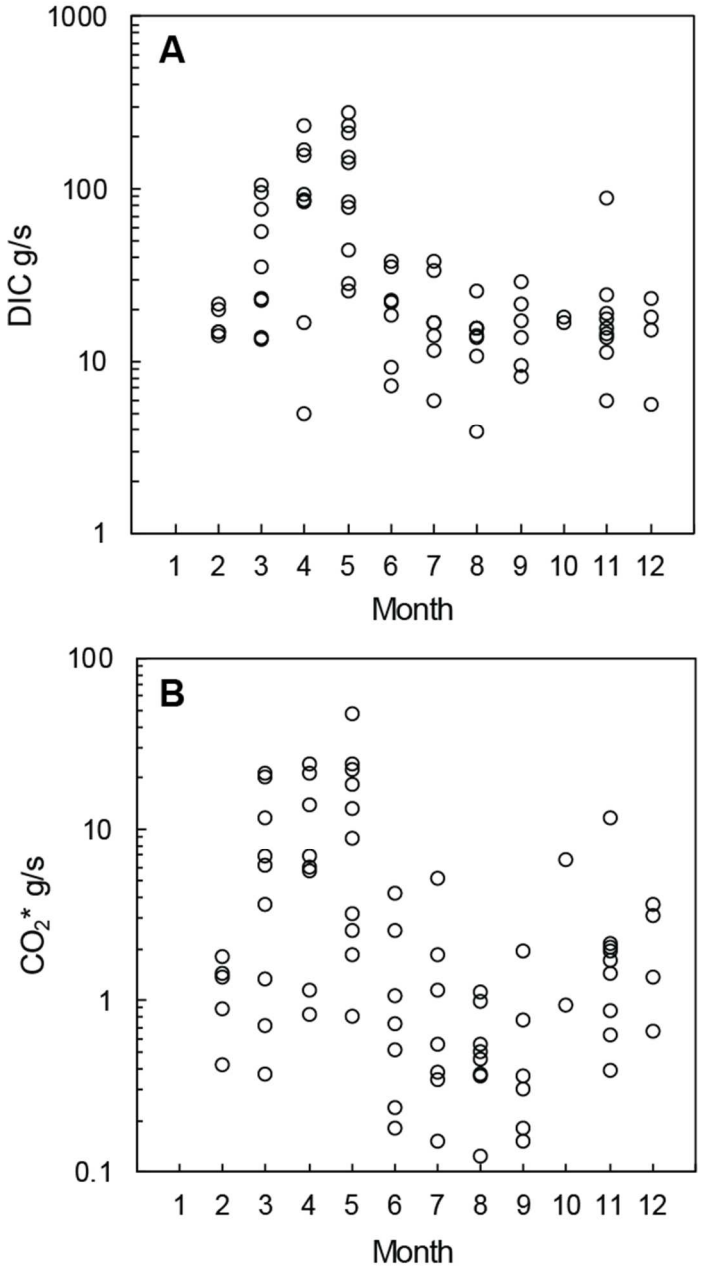

Figure 12. Discrete measurements of **A)** DIC loads (g/s) and **B)** CO_2* loads (g/s) binned by month of measurement using measured discharge and calculated DIC and CO_2* concentrations at Jemez River stream gage.

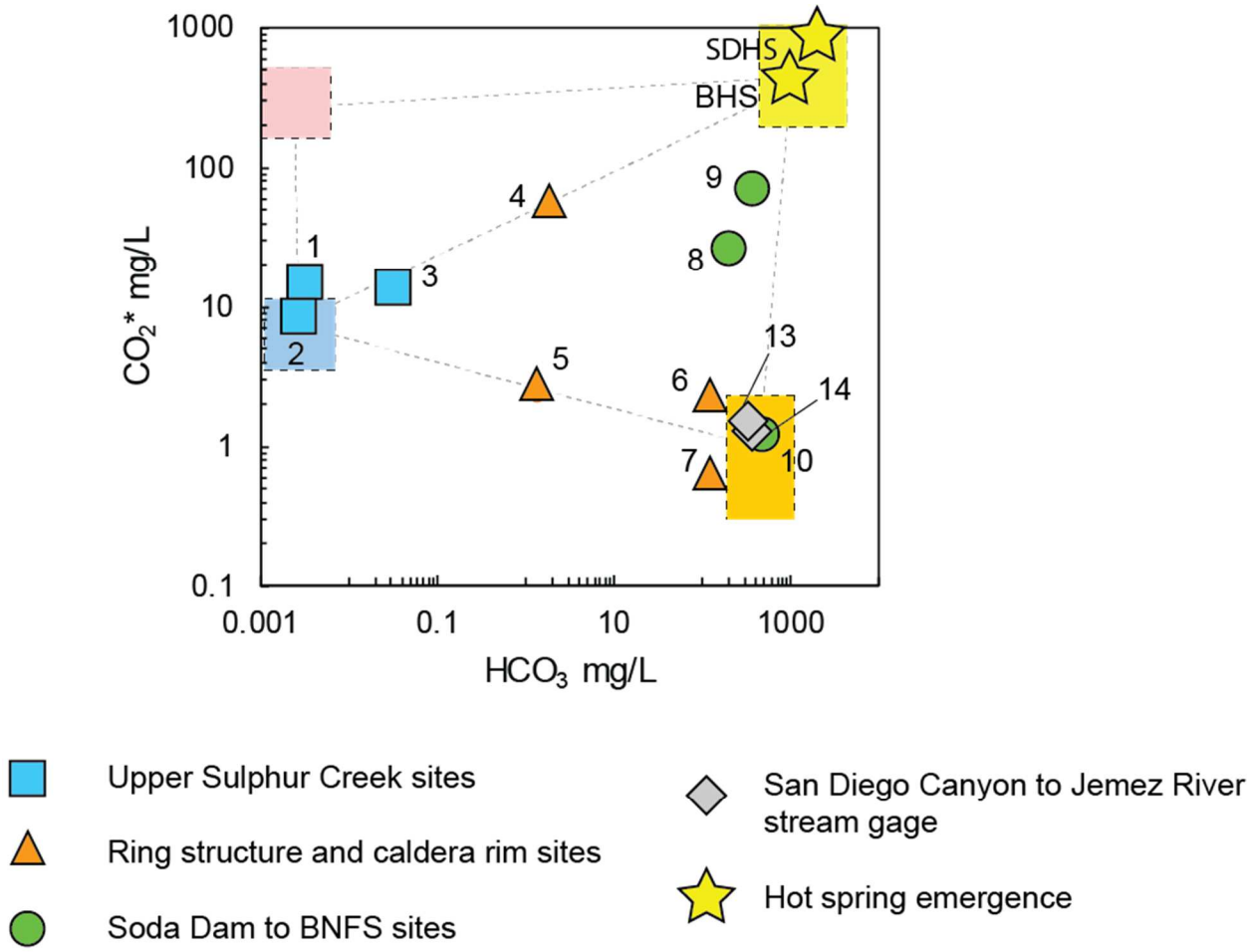

Figure 13. Estimated composition fields shown by shaded boxes for acid-sulphate thermal groundwater (salmon), non-thermal, soil-CO_2 equilibrated groundwater (blue), non-thermal, carbonate buffered groundwater (orange), and pH-neutral thermal groundwater (yellow) underlying CO_2* versus HCO_3 concentrations (mg/L)

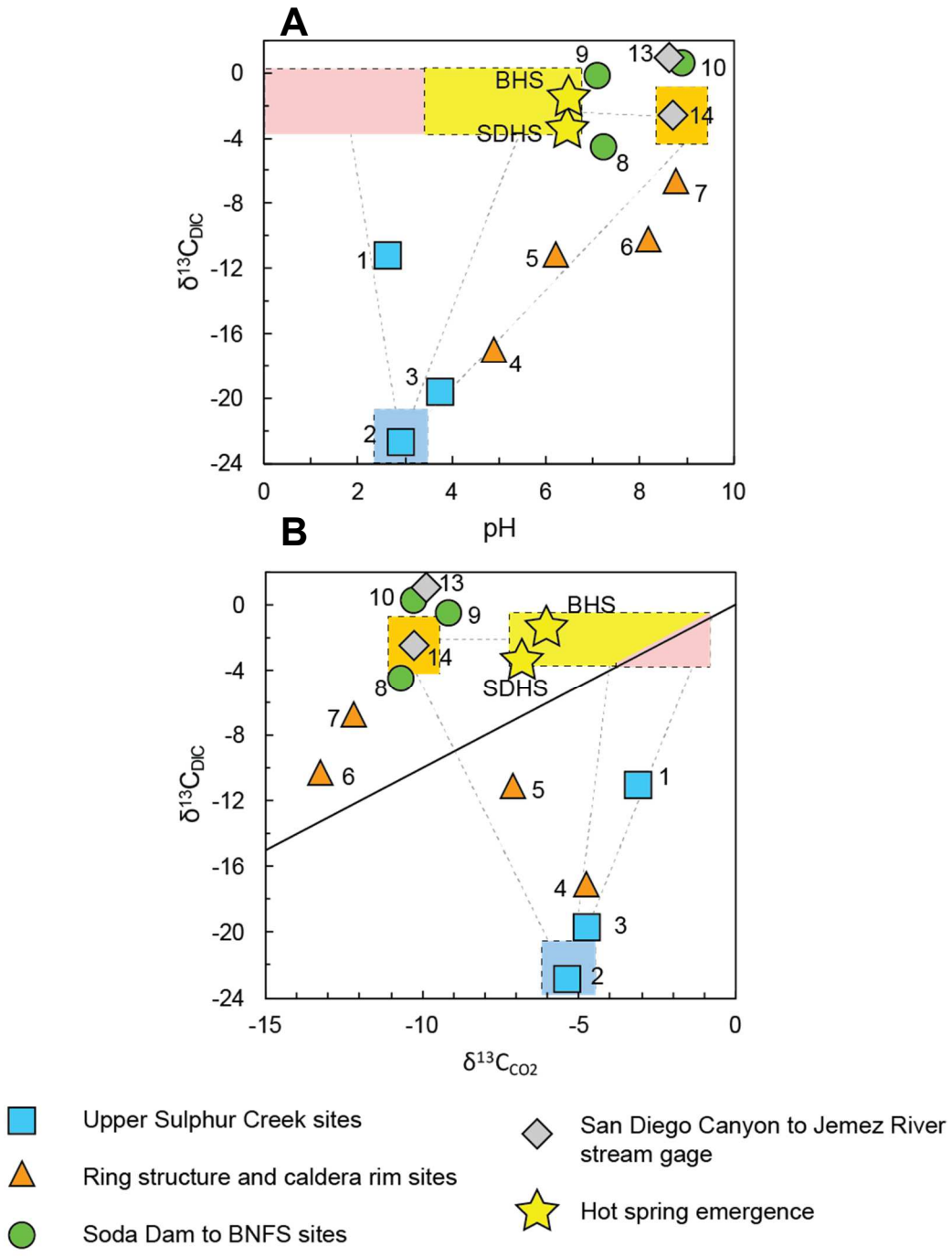

Figure 14. Estimated composition fields shown by shaded boxes for acid-sulphate thermal groundwater (salmon), non-thermal, soil-CO_2 equilibrated groundwater (blue), non-thermal, carbonate buffered groundwater (orange), and pH-neutral thermal groundwater (yellow) underlying **A**) $\delta^{13}C_{DIC}$ versus pH and **B)** $\delta^{13}C_{CO2}$ versus $\delta^{13}C_{DIC}$.

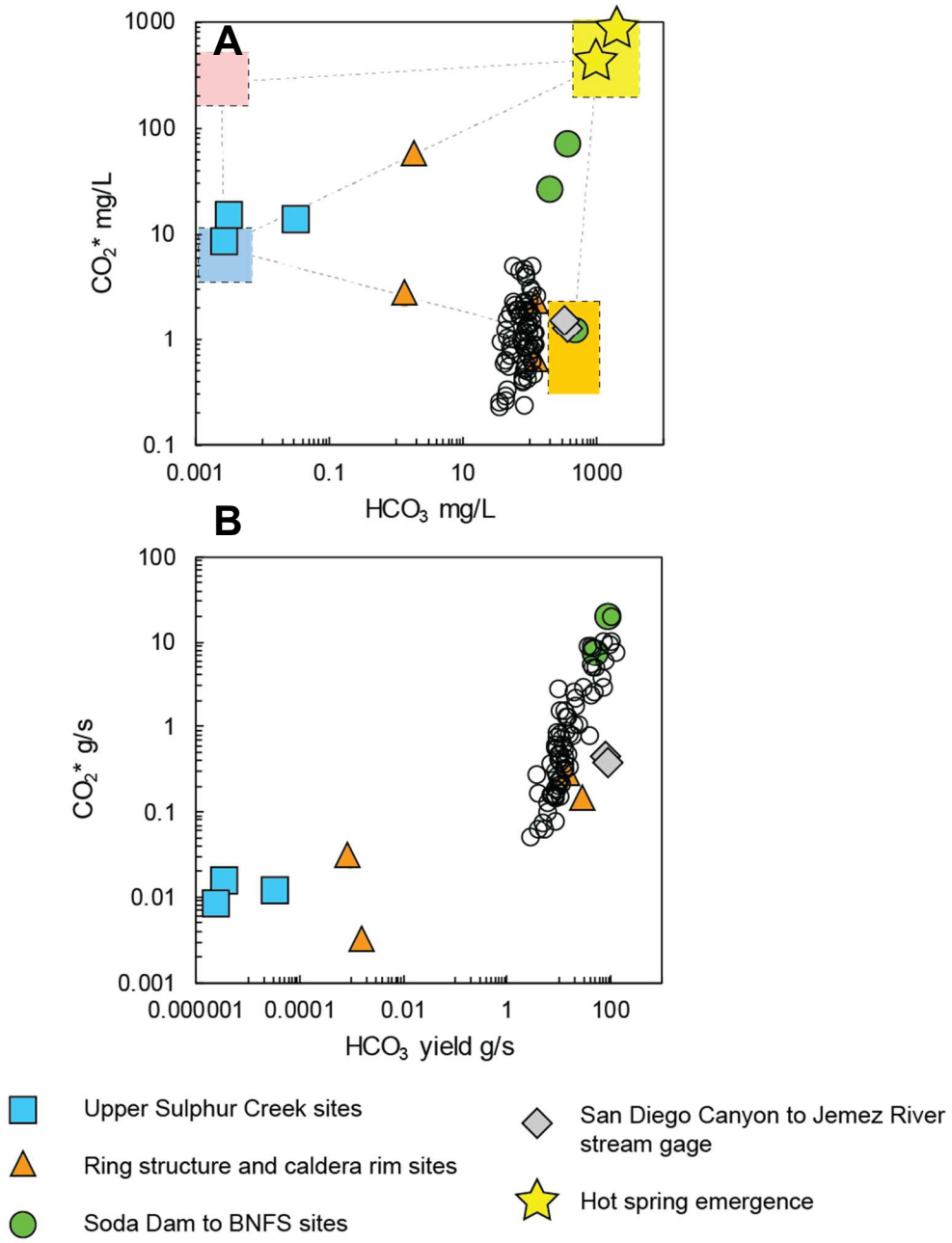

Figure 15. Estimated composition fields shown by shaded boxes for acid-sulphate thermal groundwater (salmon), non-thermal, soil-CO_2 equilibrated groundwater (blue), non-thermal, carbonate buffered groundwater (orange), and pH-neutral thermal groundwater (yellow) underlying **A**) CO_2* versus HCO_3 concentrations (mg/L) and **B)** CO_2* versus HCO_3 yield (g/s). Calculated HCO_3 and CO_2* concentrations and loads from historical water quality at Jemez River stream gage overlain (open black circles).

References Cited

Balleau, W.P., 1980, Geothermal hydrology at Jemez Mountains: ion balance and flow depletion: Report to Burea of Indian Affairs, Branch of Rights Protection, v. 35.

Banerjee, A. et al., 2011, Deep permeable fault-controlled helium transport and limited mantle flux in two extensional geothermal systems in the Great Basin, United States: Geology, v. 39, p. 195–198, doi:10.1130/G31557.1.

Bates, M.N., Garrett, N., Graham, B., and Read, D., 1998, Cancer incidence, morbidity and geothermal air pollution in Rotorua, New Zealand: International Journal of Epidemiology, v. 27, p. 10–14, doi:10.1093/ije/27.1.10.

Beitler, B., Chan, M.A., and Parry, W.T., 2003, Bleaching of Jurassic Navajo Sandstone on Colorado Plateau Laramide highs: Evidence of exhumed hydrocarbon supergiants? Geology, v. 31, p. 1041, doi:10.1130/G19794.1.

Burton, M.R., Sawyer, G.M., and Granieri, D., 2013, Deep Carbon Emissions from Volcanoes: Reviews in Mineralogy and Geochemistry, v. 75, p. 323–354, doi:10.2138/rmg.2013.75.11.

Campeau, A., Wallin, M.B., Giesler, R., Löfgren, S., Mörth, C.M., Schiff, S., Venkiteswaran, J.J., and Bishop, K., 2017, Multiple sources and sinks of dissolved inorganic carbon across Swedish streams, refocusing the lens of stable C isotopes: Scientific Reports, v. 7, p. 1–14, doi:10.1038/s41598-017-09049-9.

Caracausi, A., Ditta, M., Italiano, F., Longo, M., Nuccio, P.M., Paonita, A., and Rizzo, A., 2005, Changes in fluid geochemistry and physico-chemical conditions of geothermal systems caused by magmatic input: The recent abrupt outgassing off the island of Panarea (Aeolian Islands, Italy): Geochimica et Cosmochimica Acta, v. 69, p. 3045–3059, doi:10.1016/j.gca.2005.02.011.

Charles, R.W., Buden, R.J.V., and Goff, F., 1986, An interpretation of the alteration assemblages at Sulphur Springs, Valles Caldera, New Mexico: Journal of Geophysical Research, v. 91, p. 1887, doi:10.1029/JB091iB02p01887.

Chiodini, G., Frondini, F., Cardellini, C., Granieri, D., Marini, L., and Ventura, G., 2001, CO2 degassing and energy release at Solfatara volcano, Campi Flegrei, Italy: Journal of Geophysical Research: Solid Earth, v. 106, p. 16213–16221, doi:10.1029/2001JB000246.

Clark, I.D., 2018, Groundwater geochemistry and isotopes: Boca Raton, FL, CRC Press.

Crossey, L.J., Karlstrom, K.E., Springer, a. E., Newell, D., Hilton, D.R., and Fischer, T., 2009, Degassing of mantle-derived CO2 and He from springs in the southern Colorado Plateau region--Neotectonic connections and implications for groundwater systems: Geological Society of America Bulletin, v. 121, p. 1034–1053, doi:10.1130/B26394.1.

Davidson, E.A., Figueiredo, R.O., Markewitz, D., and Aufdenkampe, A.K., 2010, Dissolved CO2 in small catchment streams of eastern Amazonia: A minor pathway of terrestrial carbon loss: Journal of Geophysical Research: Biogeosciences, v. 115, p. 1–6, doi:10.1029/2009JG001202.

Doctor, D.H., Kendall, C., Sebestyen, S.D., Shanley, J.B., Ohte, N., and Boyer, E.W., 2008, Carbon isotope fractionation of dissolved inorganic carbon (DIC) due to outgassing of carbon dioxide from a headwater stream: Hydrological Processes, v. 22, p. 2410–2423, doi:10.1002/hyp.6833.

Duvert, C., Butman, D.E., Marx, A., Ribolzi, O., and Hutley, L.B., 2018, CO2 evasion along streams driven by groundwater inputs and geomorphic controls: Nature Geoscience, v. 11, p. 813–818, doi:10.1038/s41561-018-0245-y.

Elias, E., Steele, C., Brown, D., Behery, S., and Weight, E., 2019, Islands of resilience: Community challenges and responses to the 2018 Colorado Plateau exceptional drought, in Universities Council on Water Resources 2019 Conference, Snowbird, Utah, USA, https://www.ars.usda.gov/research/publications/publication/?seqNo115=364387 (accessed July 2019).

Ellis, A.J., 1977, Geothermal fluid chemistry and human health: Geothermics, v. 6, p. 175–182, doi:10.1016/0375-6505(77)90026-8.

Erikson, E., 1977, Hydrology-Jemez Mountains, New Mexico: open file report, Union Oil, Santa Rosa California, p. 35 pp.

Evans, W.C., Sorey, M.L., Cook, A.C., Kennedy, B.M., Shuster, D.L., Colvard, E.M., White, L.D., and Huebner, M.A., 2002, Tracing and quantifying magmatic carbon discharge in cold groundwaters: lessons learned from Mammoth Mountain, USA: Journal of Volcanology and Geothermal Research, v. 114, p. 291–312, doi:10.1016/S0377-0273(01)00268-2.

Florea, L.J., 2015, Carbon flux and landscape evolution in epigenic karst aquifers modeled from geochemical mass balance: Earth Surface Processes and Landforms, v. 40, p. 1072–1087, doi:10.1002/esp.3709.

Gardner, J.N., and Goff, F.E., 1996, Geology of the northern Valles Caldera and Toledo Embayment, New Mexico: Jemez Mountains Region, p. 225–236.

Gerlach, T.M., 1980, Investigation of volcanic gas analyses and magma outgassing from Erta' Ale lava lake, Afar, Ethiopia: Journal of Volcanology and Geothermal Research, v. 7, p. 415–441, doi:10.1016/0377-0273(80)90041-4.

Giggenbach, W.F., 1995, Variations in the chemical and isotopic composition of fluids discharged from the Taupo Volcanic Zone, New Zealand: Journal of Volcanology and Geothermal Research, v. 68, p. 89–116, doi:10.1016/0377-0273(95)00009-J.

Godsey, S.E., Kirchner, J.W., and Clow, D.W., 2009, Concentration-discharge relationships reflect chemostatic characteristics of US catchments: Hydrological Processes, v. 23, p. 1844–1864, doi:10.1002/hyp.7315.

Goff, F., and Gardner, J.N., 1994, Evolution of a mineralized geothermal system, Valles Caldera, New Mexico: Economic Geology, v. 89, p. 1803–1832, doi:10.2113/gsecongeo.89.8.1803.

Goff, F., Gardner, J.N., Hulen, J.B., Nielson, D.L., Charles, R., WoldeGrabriel, G., Vuataz, F.-D., Musgrave, J.A., Shevenell, L., and Kennedy, B.M., 1992, The Valles caldera hydrothermal system, past and present, New Mexico, USA: Sci. Drill, v. 3, p. 181–204, http://www.atlasgeoinc.com/wp-content/uploads/2012/Publications/New Mexico/Valles_Caldera.pdf.

Goff, F., Gardner, J.N., Reneau, S.L., Kelley, S.A., Kempter, K.A., and Lawrence, J.R., 2011, Geologic map of the Valles caldera, Jemez Mountains: Scorro, New Mexico Bureau of Geology and Mineral Resources, 30 p., http://ngmdb.usgs.gov/Prodesc/proddesc_9357.htm (accessed June 2019).

Goff, F., Gardner, J., Vidale, R., and Charles, R., 1985, Geochemistry and isotopes of fluids from sulphur springs, Valles Caldera, New Mexico: Journal of Volcanology and Geothermal Research, v. 23, p. 273–297, doi:10.1016/0377-0273(85)90038-1.

Goff, F., and Janik, C.J., 2002, Gas geochemistry of the Valles caldera region, New Mexico and comparisons with gases at Yellowstone, Long Valley and other geothermal systems: Journal of Volcanology and Geothermal Research, v. 116, p. 299–323, doi:10.1016/S0377-0273(02)00222-6.

Goff, F., Shevenell, L., Gardner, J.N., Vuataz, F.-D., and Grigsby, C.O., 1988, The hydrothermal outflow plume of Valles Caldera, New Mexico, and a comparison with other outflow plumes: Journal of Geophysical Research, v. 93, p. 6041–6058, doi:10.1029/JB093iB06p06041.

Griffin, B.A., and Jurinak, J.J., 1973, Estimation of activity coefficients from the electrical conductivity of natural aquatic systems and soil extracts: Soil Science, v. 116, p. 26–30, doi:10.1097/00010694-197307000-00005.

Griffin, D., Woodhouse, C.A., Meko, D.M., Stahle, D.W., Faulstich, H.L., Carrillo, C., Touchan, R., Castro, C.L., and Leavitt, S.W., 2013, North American monsoon precipitation reconstructed from tree-ring latewood: Geophysical Research Letters, v. 40, p. 954–958, doi:10.1002/grl.50184.

Hammer, Ø., Harper, D.A.T., Ryan, D.D., and Ryan, P.D., 2001, PAST : Paleontological statistics software package for education and data analysis: Palaeontologia Electronica, v. 4, p. 9, doi:10.1016/j.bcp.2008.05.025.

Hanson, M.C., Oze, C., and Horton, T.W., 2014, Identifying blind geothermal systems with soil CO2 surveys: Applied Geochemistry, v. 50, p. 106–114, doi:10.1016/j.apgeochem.2014.08.009.

Harvey, M.C., Rowland, J. V., Chiodini, G., Rissmann, C.F., Bloomberg, S., Hernández, P.A., Mazot, A., Viveiros, F., and Werner, C., 2015, Heat flux from magmatic hydrothermal systems related to availability of fluid recharge: Journal of Volcanology and Geothermal Research, v. 302, p. 225–236, doi:10.1016/j.jvolgeores.2015.07.003.

Henley, R.W., and Ellis, A.J., 1983, Geothermal systems ancient and modern: a geochemical review: Earth-Science Reviews, v. 19, p. 1–50, doi:10.1016/0012-8252(83)90075-2.

Hulen, J.B., Nielson, D.L., Goff, F., Gardner, J.N., and Charles, R.W., 1987, Molybdenum mineralization in an active geothermal system, Valles caldera, New Mexico: Geology, v. 15, p. 748–752, doi:10.1130/0091-7613(1987)15<748:MMIAAG>2.0.CO;2.

Hurwitz, S., Lowenstern, J.B., and Heasler, H., 2007, Spatial and temporal geochemical trends in the hydrothermal system of Yellowstone National Park: Inferences from river solute fluxes: Journal of Volcanology and Geothermal Research, v. 162, p. 149–171, doi:10.1016/j.jvolgeores.2007.01.003.

James, E.R., Manga, M., and Rose, T.P., 1999, CO2 degassing in the Oregon Cascades: Geology, v. 27, p. 823, doi:10.1130/0091-7613(1999)027<0823:CDITOC>2.3.CO;2.

Johnson, M.S., Billett, M.F., Dinsmore, K.J., Wallin, M., Dyson, K.E., and Jassal, R.S., 2009, Direct and continuous measurement of dissolved carbon dioxide in freshwater aquatic systems-method and applications: Ecohydrology, v. 3, p. n/a-n/a, doi:10.1002/eco.95.

Kerrick, D.M., 2001, Present and past nonanthropogenic CO2 degassing from the solid earth: Reviews of Geophysics, v. 39, p. 565–585, doi:10.1029/2001RG000105.

Kerrick, D.M., and Caldeira, K., 1998, Metamorphic CO2 degassing from orogenic belts: Chemical Geology, v. 145, p. 213–232, doi:10.1016/S0009-2541(97)00144-7.

Liu, F., Bales, R.C., Conklin, M.H., and Conrad, M.E., 2008a, Streamflow generation from snowmelt in semi-arid, seasonally snow-covered, forested catchments, Valles Caldera, New Mexico: Water Resources Research, v. 44, p. 1–13, doi:10.1029/2007WR006728.

Liu, F., Parmenter, R., Brooks, P.D., Conklin, M.H., and Bales, R.C., 2008b, Seasonal and interannual variation of streamflow pathways and biogeochemical implications in semi-arid, forested catchments in Valles Caldera, New Mexico: Ecohydrology, v. 1, p. 239–252, doi:10.1002/eco.22.

Liu, S., and Raymond, P.A., 2018, Hydrologic controls on pCO2 and CO2 efflux in US streams and rivers: Limnology and Oceanography Letters, v. 3, p. 428–435, doi:10.1002/lol2.10095.

Lowenstern, J.B., Bergfeld, D., Evans, W.C., and Hunt, A.G., 2015, Origins of geothermal gases at Yellowstone: Journal of Volcanology and Geothermal Research, v. 302, p. 87–101, doi:10.1016/j.jvolgeores.2015.06.010.

Lowenstern, J.B., Bergfeld, D., Evans, W.C., and Hurwitz, S., 2012, Generation and evolution of hydrothermal fluids at Yellowstone: Insights from the Heart Lake Geyser Basin: Geochemistry, Geophysics, Geosystems, v. 13, p. 1–20, doi:10.1029/2011GC003835.

Marini, L., and Gambardella, B., 2005, Geochemical modeling of magmatic gas scrubbing: Annals of Geophysics, v. 48, p. 739–753.

Martini, M., 1996, Chemical Characters of the Gaseous Phase in Different Stages of Volcanism: Precursos and Volcanic Activity, in Scarpa, R. and Tilling, R. eds., Monitoring and mitigation of volcano hazards, Berlin, Heidelberg, Springer, p. 199–219, doi:10.1007/978-3-642-80087-0.

Mayorga, E., Aufdenkampe, A.K., Masiello, C.A., Krusche, A. V., Hedges, J.I., Quay, P.D., Richey, J.E., and Brown, T.A., 2005, Young organic matter as a source of carbon dioxide outgassing from Amazonian rivers: Nature, v. 436, p. 538–541, doi:10.1038/nature03880.

McGibbon, C., Crossey, L.J., Karlstrom, K.E., and Grulke, T., 2018, Carbonic springs as distal manifestations of geothermal systems, highlighting the importance of fault pathways and hydrochemical mixing: Example from the Jemez Mountains, New Mexico: Applied Geochemistry, v. 98, p. 45–57, doi:10.1016/J.APGEOCHEM.2018.08.015.

McIntosh, J.C. et al., 2017, Geochemical evolution of the Critical Zone across variable time scales informs concentration-discharge relationships: Jemez River Basin Critical Zone Observatory: Water Resources Research, v. 53, p. 4169–4196, doi:10.1002/2016WR019712.

Meyer-Dombard, D.R., Swingley, W., Raymond, J., Havig, J., Shock, E.L., and Summons, R.E., 2011, Hydrothermal ecotones and streamer biofilm communities in the Lower Geyser Basin, Yellowstone National Park: Environmental Microbiology, v. 13, p. 2216–2231, doi:10.1111/j.1462-2920.2011.02476.x.

de Moor, J.M., Aiuppa, A., Pacheco, J., Avard, G., Kern, C., Liuzzo, M., Martínez, M., Giudice, G., and Fischer, T.P., 2015, Short-period volcanic gas precursors to phreatic eruptions: Insights from Poás Volcano, Costa Rica: Earth and Planetary Science Letters, v. 442, p. 218–227, doi:10.1016/j.epsl.2016.02.056.

Natural Resources Conservation Service, 2018, Mountain Snowpack Map - Colorado River:, https://www.wcc.nrcs.usda.gov/cgibin/colosnow.pl?state=colorado_river (accessed July 2019).

Person, M., Kelley, S., Kelley, R., Karra, S., Harp, D., Witcher, J., Bielicki, J., Sutula, G., Middleton, R., and Pepin, J.D., 2015, Hydrogeologic Windows : Detection of Blind and Traditional Geothermal Play Fairways in Southwestern New Mexico Using Conservative Element Concentrations and Advective-Diffusive Solute Transport: GRC Transactions, v. 39, p. 751–759.

Rao, U., Fehn, U., Teng, R.T.D., and Goff, F., 1996, Sources of chloride in hydrothermal fluids from the Valles caldera, New Mexico: a 36Cl study: Journal of Volcanology and Geothermal Research, v. 72, p. 59–70, doi:10.1016/0377-0273(95)00069-0.

Robbins, L.L., Hansen, M.E., Kleypas, J.A., and Meylan, S.C., 2010, CO2calc: A User-Friendly Seawater Carbon Calculator for Windows, Mac OS X, and iOS (iPhone):, doi:10.3133/OFR20101280.

Rogie, J.D., Kerrick, D.M., Sorey, M.L., Chiodini, G., and Galloway, D.L., 2001, Dynamics of carbon dioxide emission at Mammoth Mountain, California: Earth and Planetary Science Letters, v. 188, p. 535–541, doi:10.1016/S0012-821X(01)00344-2.

Self, S., Goff, F., Gardner, J.N., Ight, J.V.W., Kite, W.M., Wright, J. V., and Kite, W.M., 1986, Explosive Rhyolitic Volcanism in the Jemez Mountains: Vent Locations, Caldera Development and Relation to Regional Structure: Journal of Geophysical Research, v. 91, p. 1779–1798, doi:10.1029/JB091iB02p01779.

Sheppard, D., Truesdell, A., and Janik, C., 1992, Geothermal gas compositions in yellowstone National Park, USA: … of volcanology and geothermal …, v. 51, p. 79–93, http://www.sciencedirect.com/science/article/pii/037702739290061H (accessed January 2013).

Smith, R.L., and Bailey, R.A., 1968, Resurgent Cauldrons, in Coats, R.R., Hay, R.L., and Anderson, C.A. eds., Studies in Volcanology, Boulder, Colorado, Geological Society of America, p. 613–662, doi:10.1130/MEM116-p613.

Stumm, W., and Morgan, J.J., 1996, Aquatic Chemistry: New York, NY, John Wiley & Sons, 1040 p.

Szynkiewicz, A., Goff, F., Vaniman, D., and Pribil, M.J., 2019, Sulfur cycle in the Valles Caldera volcanic complex, New Mexico – Letter 1: Sulfate sources in aqueous system, and implications for S isotope record in Gale Crater on Mars: Earth and Planetary Science Letters, v. 506, p. 540–551, doi:10.1016/j.epsl.2018.10.036.

Trainer, F.W., 1974, Ground Water in the Southwestern Part of the Jemez Mountains Volcanic Region , New Mexico, in Siemers, C.T., Woodward, L.A., and Callender, J.F. eds., New Mexico Geological Society 25th Annual Fall Field Conference Guidebook, p. 337–345.

Trainer, F.W., 1984, Thermal mineral springs in Canon de San Diego as a window into Valles Caldera, New Mexico, in Baldridge, W.S., Dickerson, P.W., Riecker, R.E., and Zidek, J. eds., New Mexico Geological Society 35th Annual Fall Field Conference Guidebook, New Mexico Geological Society, p. 249–255.

Trainer, F.W., Rogers, R.J., and Sorey, M.L., 2000, Geothermal hydrology of Valles Caldera and the southwestern Jemez Mountains, New Mexico:, doi:10.3133/wri004067.

Truesdell, A.H., Haizlip, J.R., Armannsson, H., and D'Amore, F., 1989, Origin and transport of chloride in superheated geothermal steam: Geothermics, v. 18, p. 295–304, doi:10.1016/0375-6505(89)90039-4.

Truesdell, A.H., and Janik, C.J., 1986, Reservoir processes and fluid origins in the Baca Geothermal System, Valles Caldera, New Mexico: Journal of Geophysical Research, v. 91, p. 1817–1833, doi:10.1029/JB091iB02p01817.

Turnipseed, D.P., and Sauer, V.B., 2010, Discharge measurements at gaging stations, in U.S. Geological Survey Techniques and Methods, p. 87, https://pubs.usgs.gov/tm/tm3-a8/.

Vuataz, F.D., and Goff, F., 1986, Isotope geochemistry of thermal and nonthermal waters in the Valles Caldera, Jemez Mountains, Northern New Mexico: Journal of Geophysical Research, v. 91, p. 1835–1853, doi:10.1029/JB091iB02p01835.

Vuataz, F.-D., Goff, F., Fouillac, C., and Calvez, J., 1988, A strontium isotope study of the VC-1 core hole and associated hydrothermal fluids and rocks from Valles Caldera, Jemez Mountains, New Mexico: Journal of Geophysical Research, v. 93, p. 6059, doi:10.1029/JB093iB06p06059.

Werner, C., Evans, W.C., Kelly, P.J., McGimsey, R., Pfeffer, M., Doukas, M., and Neal, C., 2012, Deep magmatic degassing versus scrubbing: Elevated CO 2 emissions and C/S in the lead-up to the 2009 eruption of Redoubt Volcano, Alaska: Geochemistry, Geophysics, Geosystems, v. 13, p. n/a-n/a, doi:10.1029/2011GC003794.

White, A.F., 1986, Chemical and isotopic characteristics of fluids within the Baca geothermal reservoir, Valles caldera, New Mexico: Journal of Geophysical Research, v. 91, p. 1855–1866.

White, D.E., Barnes, I., and O'Neil, J.R., 1973, Thermal and Mineral Waters of Nonmeteoric Origin, California Coast Ranges: Geological Society of America Bulletin, v. 84, p. 547, doi:10.1130/0016-7606(1973)84<547:TAMWON>2.0.CO;2.

White, A.F., Chuma, N.J., and Goff, F., 1992, Mass transfer constraints on the chemical evolution of an active hydrothermal system, Valles caldera, New Mexico: Journal of Volcanology and Geothermal Research, v. 49, p. 233–253, doi:10.1016/0377-0273(92)90016-7.

White, A., Moravec, B., McIntosh, J., Olshansky, Y., Paras, B., Sanchez, R.A., Ferré, T.P.A., Meixner, T., and Chorover, J., 2019, Storage and routing of water in the deep critical zone of a snow dominated volcanic catchment: Hydrology and Earth System Sciences Discussions, p. 1–38, doi:10.5194/hess-2019-140.

Zhang, J., Quay, P.D., and Wilbur, D.O., 1995, Carbon isotope fractionation during gas-water exchange and dissolution of CO2: Geochimica et Cosmochimica Acta, v. 59, p. 107–114, doi:10.1016/0016-7037(95)91550-D.

Chapter 4. Monitoring atmospheric, soil, and dissolved CO_2 using a low-cost, Arduino monitoring platform (CO2-LAMP): theory, fabrication, and operation

This chapter is composed of the publication:

Blackstock, J.M., Covington, M.D., Perne, M., Myre, J.M., in review, Monitoring atmospheric, soil, and dissolved CO_2 using a low-cost, Arduino monitoring platform (CO2-LAMP): theory, fabrication, and operation: Frontiers in Earth Science

Abstract

Variability of CO_2 concentrations within the Earth system occurs over a wide range of time and spatial scales. Resolving this variability and its drivers in terrestrial and aquatic environments ultimately requires high-resolution spatial and temporal monitoring; however, relatively high-cost gas analyzers and data loggers can present barriers in terms of cost and functionality. To overcome these barriers, we developed a low-cost Arduino monitoring platform (CO2-LAMP) for recording CO_2 variability in electronically harsh conditions: humid air, soil, and aquatic environments. A relatively inexpensive CO_2 gas analyzer was waterproofed using a semi-permeable, expanded polytetrafluoroethylene membrane. Using first principles, we derived a formulation of the theoretical operation and measurement of $PCO_{2(aq)}$ by infrared gas analyzers submerged in aquatic environments. This analysis revealed that an IRGA should be able to measure $PCO_{2(aq)}$ independent of corrections for hydrostatic pressure. CO2-LAMP theoretical operation and measurement were also verified by accompanying laboratory assessment measuring $PCO_{2(aq)}$ at multiple water depths. The monitoring platform was also deployed at two sites within the Springfield Plateau province in northwest Arkansas, USA: Blowing Springs

Cave and the Savoy Experimental Watershed. At Blowing Springs Cave, the CO2-LAMP operated alongside a relatively greater-cost CO_2 monitoring platform. Over the monitoring period, measured values between the two systems covaried linearly (r^2 = 0.97 and 0.99 for cave air and cave stream dissolved CO2, respectively). At the Savoy Experimental Watershed, measured soil CO_2 variability capturing sub-daily variation was consistent with previously documented studies in humid, temperate soils. Daily median values varied linearly with soil moisture content (r^2 = 0.84). Overall, the CO2-LAMP captured sub-daily variability of CO_2 in humid air, soil, and aquatic environments that, while out of the scope of the study, highlight both cyclical and complex CO_2 behavior. At present, long-term assessment of platform design is ongoing. Considering cost-savings, CO2-LAMP presents a working base design for continuous, accurate, low-power, and low-cost CO_2 monitoring for remote locations.

Introduction

Carbon exchange within the Earth system is facilitated, in part, by the production, transfer, and uptake of carbon dioxide (Schimel et al., 2001; Brantley et al., 2007). Unraveling biologic and biogeochemical (Broecker and Sanyal, 1998; Deman et al., 2007; Davidson et al., 2010; Florea, 2015), geologic (Lowenstern, 2001; Werner and Cardellini, 2006; Burton et al., 2013; Queiβer et al., 2016), and anthropogenic factors (Olah et al., 2011; Ward et al., 2015; Decina et al., 2016) that influence CO_2 concentrations require not only accurate, high-frequency CO_2 concentration measurements, but widely distributed, and if possible, spatially dense CO_2 measurements (Schimel et al., 2001; McDowell et al., 2008; Hari et al., 2008; Richter and Mobley, 2009; Brantley et al., 2016).

Long-term, high-frequency measurements of CO_2 concentrations are limited across Earth (McDowell et al., 2008; Andrews et al., 2014) compared to other continuous environmental monitoring in terrestrial and aquatic environments (e.g. air and stream temperature, air pressure, humidity, stream pH) (Martin et al., 2017). In turn, the inter- and intra-seasonal variability of CO_2 and environmental factors controlling variability across terrestrial ecosystems remains poorly constrained (Serrano-Ortiz et al., 2010; Lombardozzi et al., 2015). Reducing these uncertainties in carbon transfers hinges upon increasing the spatial and temporal coverage of CO_2 measurements across the Earth system (Schimel et al., 2001, 2015; Lombardozzi et al., 2015; Bradford et al., 2016).

While the availability of commercial, field-deployable infrared gas analyzers (IRGA) have greatly enhanced measurement capacity, costs due to instrumentation acquisition, maintenance, and, in some cases, limited storage capacity and control over measurement frequency using proprietary systems greatly limit the spatial and temporal extent of monitoring

(Fisher and Gould, 2012; Martin et al., 2017). Furthermore, ancillary data, such as temperature (in air or water), are needed for environmental correction of CO_2 values, but combined sensor and data logger selection may be limited between proprietary systems stemming from incompatibilities between manufacturers (Fisher and Gould, 2012).

Over the last decade, the availability and use of relatively inexpensive microcontrollers and 'microcomputers' for scientific research has increased significantly (Cressey, 2017). Use of these platforms to interface sensors has grown, in part, from the increasing availability of sensors and the need for customized interfacing to measure and monitor conditions both in increasingly complex laboratory experiments and challenging environmental settings (e.g. caves) (Pearce, 2012; Beddows and Mallon, 2018). Low-cost CO_2 IRGAs (<$150 USD) and low-cost Arduino monitoring platforms (LAMPs) have been specifically used to measure and monitor dissolved CO_2 using automated floating chambers (Bastviken et al., 2015) and ambient CO_2 (Martin et al., 2017); however, adoption of a low-cost IRGA for electronically harsh conditions, such as high-humidity environments (e.g caves) or within stream environments (i.e. submerged, direct dissolved CO_2 measurement), have been limited. If similar methods for waterproofing CO_2 sensors are used (Johnson et al., 2009), adoption of a low-cost IRGA to monitor CO2 in electronically harsh environments should be possible.

We present a low-cost ($250 to $300 USD), Arduino-based monitoring platform (CO2-LAMP) for measuring atmospheric, soil, and dissolved CO_2 concentrations. Included in this study are methods for fabrication, reference measurement (i.e. zero and span reference gases), instrument value corrections and post-processing, and results from field-trial evaluations. As part of the reference measurement and post-processing, a novel presentation of theoretical sensor operation, sensor output, and accompanying empirical experiments were made to verify

theoretical instrument output and applicable environmental corrections. Consequently, the description and corrections are highly relevant to other direct, dissolved gas measurement systems by IRGAs (Johnson et al., 2009; Yoon et al., 2016). Field evaluation comprised: 1. a comparative field trial between the CO2-LAMP and a relatively greater-cost system for monitoring ambient CO_2 and dissolved CO_2, and 2. monitoring soil CO_2 in a shallow soil pit. Lastly, recommendations and future work with respect to fabrication, improving measurement accuracy, and deployment of the CO2-LAMP are discussed.

Research Questions and Hypotheses

The primary objectives of this research were to fabricate and assess the waterproofing of a low-cost CO_2 IRGA both in a laboratory and field-setting to which the study focused on answering three main research questions and associated empirical hypotheses.

Research Question I

Is waterproofing of a low-cost CO_2 infrared gas analyzer suitable for dissolved CO_2 measurements?

Hypothesis I

Using established methods previously implemented in waterproofing other IRGAs, adaptation of similar materials and methods are appropriate for a low-cost IRGA despite differences in form factor shape and size.

Research Question II

Are the differences between the low-cost IRGA and a commonly used, more expensive waterproofed CO2 analyzer within the range of other dissolved CO_2 measurement methods? If differences are present, what might explain these differences?

Hypothesis II

Assuming that: 1, field measurements by a relatively more expensive dissolved CO_2 system are a reference value; 2, the low-cost IRGA is operating within manufacturer specifications; and 3, environmental corrections for temperature are appropiate, the measurements made by the low-cost system should be within the typical range of values observed between variable dissolved CO_2 measurement methods.

Research Question III

Can the low-cost monitoring platform handle electronically harsh conditions during field deployment? What effects, if any, are observed several over weeks in these harsh environments?

Hypothesis III

If waterproofing is adequate, condensation is minimal, and environmental conditions (e.g. temperature, humidity) inside the membrane-enclosed volume are within the environmental ranges specified by low-cost gas analyzer manufacturer, harsh environments should not impede normal IRGA operation.

Measurement of CO_2 in Earth's near-surface environment

Analysis of CO_2 in air and soils

Analysis of ambient and soil CO_2 are routinely conducted by discrete sampling and in situ gas analyzers (Jassal et al., 2005; Andrews et al., 2014; Sánchez-Cañete et al., 2017; Jochheim et al., 2018). Discrete sampling is conducted primarily through gas collection into evacuated, air-tight or 'inert-gas flushed' (e.g. helium flushing) containers. Extracted gases are subsequently sampled, typically using an IRGA, gas chromatograph (GC), or isotope ratio mass spectrometer (Breecker and Sharp, 2008; Joos et al., 2008). Common in situ gas analyzers for

measuring $CO_{2(soil)}$ have included the Vaisala GMD20, GMM221, and GMM222 (Hirano et al., 2003; Jassal et al., 2005; Sánchez-Cañete et al., 2017). Unlike discrete measurements, in situ sensors require continual reference measurements to ensure accountability for sensor drift and offsets during deployment (Moran et al., 2010; Andrews et al., 2014). To further ensure instrument accuracy through time, ancillary parameters, which include temperature, relative humidity, and atmospheric pressure, must also be measured (Fietzek et al., 2014). To protect against instrument damage, a protective membrane, such as silicone or polytetrafluoroethylene, is used to cover the sensor, but still allow for gas exchange (Tang et al., 2003; Jassal et al., 2005).

Measurement of aqueous CO_2

Dissolved CO_2 concentrations are most often obtained through three common methods: 1. estimation of CO_2 concentrations from alkalinity titration and carbonate species equilibria calculations (Stumm and Morgan, 1996; Abril et al., 2015; Jarvie et al., 2017); 2. manual gas extraction from water sample collection in air-tight containers (e.g. copper tubing, manual headspace analysis) (Sanford et al., 1996 and references therein); and 3. directly measured through gas equilibration (Takahashi, 1961; Frankignoulle et al., 2001; Johnson et al., 2009; Yoon et al., 2016). The majority of dissolved CO_2 values reported for natural waters have been, to date, through carbonate equilibria calculations from measured pH and total alkalinity (Abril et al., 2015; Liu and Raymond, 2018). However, reported dissolved partial pressures of CO_2 and corresponding dissolved CO_2 concentrations for inland freshwaters are likely overestimated due to: 1. greater total alkalinity derived from organic acid anions with greater dissolved organic carbon and less carbonate alkalinity, and 2. calculations of the partial pressure of CO_2 are more sensitive given the diminished buffering capacity of water at lower pH (Abril et al., 2015).

Importantly, this research highlights the critical need for direct measurements of CO_2 given the large uncertainty that may arise for many inland, freshwater systems.

Direct measurement of dissolved CO_2

Direct dissolved CO_2 measurement systems have been previously described by Yoon et al. (2016) and are separated into two categories: active-equilibration and a passive-equilibration. The active-equilibration methods being: manual gas extraction; a spray-type equilibrator (Takahashi, 1961); and a marble-type equilibrator (Frankignoulle et al., 2001). In active-equilibration systems, an external power-source facilitates water-air equilibration by pumping external water through sprayers or marble media. Enclosed, internal air volumes are circulated through an IRGA. The passive method is referred to as a 'membrane-enclosed sensor'. Passive membrane-enclosed sensors work via diffusion and equilibration of gases across a liquid-impermeable, but gas-permeable, membrane (Sanford et al., 1996; Johnson et al., 2009).

Compared to spray- and marble-type equilibrators, membrane-enclosed sensors are practical in harsher environments such as soil and surface waters, which can be variably saturated or highly turbid and prone to tube clogging or instrument fouling. This method is also more useful in situations where power delivery is limited (e.g. caves). However, membrane-enclosed sensors have the drawback of significantly longer equilibration times (> 10 min), and therefore they may not fully capture short-term, large-magnitude variations (Yoon et al., 2016).

Hybrid systems also exist, which interface with surrounding water through membrane-mediated gas exchange (i.e. a membrane-enclosed equilibrator), but also internally circulate air for heating and thermal equilibrium (De Gregorio et al., 2011; Fietzek et al., 2014). To decrease equilibration time in membrane-enclosed systems, external pumps near the membrane may also

move water near the membrane interface to limit expansion of a static boundary layer (Manning et al., 2003; Fietzek et al., 2014).

For all direct-measurement systems, CO_2 measured by an IRGA or GC is the equivalent partial pressure of CO_2, $PCO_{2(aq)}$, in equilibrium with the dissolved CO_2 of the water in accordance with Henry's Law:

$$PCO_2 = KCO_2 C_i, \quad (1)$$

where KCO_2 is the Henry's Law constant for CO_2 at a given temperature and salinity and C_i is the concentration of dissolved CO_2 in water. Dalton's Law states that the sum of partial pressures for all dissolved gas species are equal to the total dissolved gas pressure in the water, P_{TDG}:

$$P_{TDG} = N_2 + O_2 + CO_2 + other gases. \quad (2)$$

For most shallow surface waters and unconfined groundwater systems, P_{TDG} is approximately equal to ambient atmospheric pressures (Manning et al., 2003; Gardner and Solomon, 2009); however, notable exceptions include: 1. dam tailwaters (D'Aoust and Clark, 1980; Urban et al., 2008) and similar surface conditions that promote entrainment of bubbles at greater depths where P_{TDG} may be upwards of 1.3 times atmospheric pressure; 2. deep, confined groundwater systems (Gardner and Solomon, 2009; Ryan et al., 2015); and 3. deep, crater lake systems containing subsurface gas vents at depth, such as Lakes Monoun and Nyos in Cameroon (Kling et al., 1987; Kusakabe and Sano, 1992). In both confined groundwater and deep, lake gas vent systems where increased hydrostatic pressure allows for greater gas saturation (i.e. increased concentration), P_{TDG} values may be several times that of atmospheric pressure if waters are gas saturated. In practice, dual measurement of total dissolved gas pressure and dissolved CO_2 are recommended in environments where P_{TDG} is suspected to be greater than atmospheric pressure (Ryan et al., 2015).

At abyssopelagic depths (> ~ 4000 m) in marine systems, changes in Henry's constant due to hydrostatic pressure must be taken in account when calculating expected PCO_2 for a given dissolved CO_2 concentration or vice versa (Enns et al., 1965; Hamme et al., 2015). However, for inland freshwater systems, such depths are not encountered. Moreover, Henry's Law constants for dissolved gas measurements at Lake Baikal (i.e. Earth's deepest lake at ~ 1600 m) would only be offset approximately 2.2% (Enns et al., 1965; Hamme et al., 2015). Therefore, changes in Henry's Constants with respect to hydrostatic pressure for respective dissolved gas species are negligible for relatively shallow water bodies.

Membrane-enclosed equilibration principles

Gas exchange between an external environment (i.e. atmosphere, soil, or water) and a membrane-enclosed volume, or headspace containing an IRGA, has been previously described using a Solution-Diffusion model, where exchange is driven by differences in the partial pressures of the external environment, P_{env}, and within the headspace, P_{IRGA} (Bareer, 1939; Sanford et al., 1996; De Gregorio et al., 2005; Gardner and Solomon, 2009). From De Gregorio et al. (2005), assuming P_{env} to be constant, the partial pressure of CO_2 in the headspace at some time, t, may be estimated by

$$P_{IRGA}(t) = P_{env} + (P_i - P_{env})e^{-\frac{K_p A}{Vh}t}, \quad (3)$$

where P_i is the initial partial pressure of CO_2 in the headspace, K_p is equal to the effective diffusivity of the gas through the environment-membrane boundary and the membrane material (Gardner and Solomon, 2009), A is membrane surface area, and h *is* membrane thickness.

Empirically, the exponential term can be calculated from experimental data using a modified form of Equation 3, whereby generalizing the exponential term and solving for a constant q:

$$P_{IRGA}(t) = P_{env} + (P_i - P_{env})e^{-qt}. \quad (4)$$

If K_p is unknown, but A, V, and h are well constrained, K_p can be solved by rearranging the obtained q constant:

$$K_p = \frac{-qVh}{A}. \quad (5)$$

Particularly in the case of membrane submersion within water, diffusion of the gas within the water may have an important impact on transfer rates, rather than mass transfer being controlled by diffusion through the membrane alone. In this case, a slight modification of Equation 4 can be used to calculate the mass transfer coefficient, k, where $k=K_p/h$ may be more meaningful.

For description of percent equilibration of CO_2 to a reference gas, an exponential, or *e*-folding, timescale can be used to describe the amount of time over which changes in concentration or percent equilibration associated with an exponential process (e.g. gas equilibration) occur by factors of $e \sim 2.718$. From measured PCO_2 using a waterproofed IRGA, *e*-folding time units, T_f in seconds, can be expressed as

$$T_f = \frac{t}{\ln\left(\frac{P_{IRGA}(t)}{P_i}\right)} \quad (6)$$

where t is equal to the time elapsed from the beginning of the observation period. To determine n *e*-folding time, where n is the folding time interval (e.g. 3-folding times), n is divided by τ, which is equal to the q constant value obtained from the exponential function term (see Equation 4): e-folding time = n/τ. For example, at 3 e-folding time (or $3/\tau$), equilibration of a mixture from the initial to final concentration is at approximately 95 %, i.e. $1-(1/e^3)$. In turn, solving for $3/\tau$ determines the specific T_f equivalent to a measured value and actual time, t, where the partial pressure or concentration of CO_2 is 95% equilibrated.

Materials and Methods

CO2-LAMP fabrication for humid and aqueous environments

Fabrication of CO2-LAMP consisted of waterproofing a relatively low-cost IRGA using a semi-permeable membrane (Figure 1) and interfacing the IRGA with an Arduino-based platform to read and record instrument values. The IRGAs used in this study were the K30 1 and 10 % analyzers manufactured by Senseair AB (Delsbo, Sweden). Analyzer accuracies are reported by the manufacturer as ±30 parts per million by volume (ppmv) ± 3% for the K30 1% model and ±300 ppmv ± 3% for the 10% model, respectively.

The membranes used were an expanded polytetrafluoroethylene ePTFE sleeve (Product number 200-07; International Polymer Engineering, Tempe, AZ, USA) and ePTFE gasket disc (Product number 1084N86, McMaster-Carr, Douglasville, GA, USA). Before enclosing the sensor, a serial cable was soldered to the K30 printed circuit boards (PCB) for interfacing the sensor with either Arduino microcontroller or desktop-PC. Then, the ePTFE membrane was placed over the K30 hydrophobic filter and attached to the K30 PCB by applying a small amount of Plasti Dip rubber compound (Plasti Dip International, Blaine, MN, USA). Subsequent coats of Plasti Dip were applied to create an effective seal at the contact of the membrane and the PCB.

During coating steps, small holes in the rubber compound can form from degassing of the agent requiring multiple rubber compound coats. Small openings on the underside of the K30 PCB were then also filled with Plasti Dip. Importantly, a one-hour curing period was allowed between applying coats of the rubber compound. After application, to ensure a complete seal, a 24 hour wait period was allotted allowing for a full cure of the rubber compound. A hole large enough for the serial cable was then drilled into a small plastic case and the K30 was placed inside the plastic case with the serial cable extending through the hole in the plastic case.

A small amount of Sugru silicone adhesive (FormFormForm Ltd, London, United Kingdom) was also used to horizontally level the K30. Subsequently, the K30 was then 'potted' in Hysol 9460 epoxy (Henkel Corporation, Rocky Hill, CT, USA) just up to the point of covering the membrane. Lastly, a final rubber coating was applied at the contact between the epoxy and membrane and at the serial cable-epoxy contact (Figure 1). Membrane thickness and estimated area were ~ 1 mm and 8 cm^2

For the majority of the laboratory experiments, respectively, and all field trials, the K30 was interfaced to an Arduino Uno (https://www.arduino.cc) with a connected Adafruit (New York, NY, USA) Data Logging shield using a universal asynchronous receiver/transmitter (UART) serial connection. During some laboratory trials, the K30s were instead interfaced via USB to a desktop computer where readings were read and logged using CO2Meter GasLab software (CO2Meter.com, Ormond Beach, FL, USA). Two Arduino sketches (i.e. programs) were written to interface the Uno and a power relay switch (Seeed Studio, Shenzhen, China) to control power delivery to the K30 in two modes: 1. a semi-continuous mode, where values were logged every 10 seconds for 60 seconds and then the sensor was powered off for one minute before another measurement period began; and 2. a lower-power mode, where values were logged every 10 seconds for 20 minutes, followed by a 40 minute sleep period. Between measurement cycles, the Uno was in 'sleep' mode to reduce power consumption. In general, the low-power mode is advantageous in environments where direct power and battery recharge (e.g. solar panels) are not possible (e.g. caves).

Power was delivered to the K30 and Arduino Uno using regulated power supplies in the laboratory and 12V batteries in the field. Between the power source and CO2-LAMP components, a step-down regulator was used to ensure a 6.5 V delivery to the Arduino and K30.

While the K30 required only 5.5 V for operation, the additional voltage was applied to supplement for transmission loss given the length of the cable to the K30 (~ 8 m). Measured K30 values were recorded on an SD Card using an Adafruit Assembled Data Logging shield for Arduino (Product 1141, Adafruit, New York, NY, USA).

Zero and span reference measurements

To initially verify K30 accuracy, span gas measurements were made using certified CO_2-Nitrogen balanced gas mixtures of 2,000 and 10,000 ppmv CO_2 (± 2% analytical uncertainty) both in a dry, gas-filled chamber (Figure 2A) and partially water-filled chamber where the sensor was submerged (Figure 2B). For the dry reference measurements, a waterproofed K30 was placed in a dry, vented chamber while the reference gas mixture was continuously delivered to the chamber until equilibration with the reference gas was obtained. For the submerged reference measurements, a waterproofed K30 was placed in a vented, partially water-filled chamber where reference gas mixtures were delivered to the chamber via a diffuser stone at the base of the chamber. The water in the chamber was considered equilibrated to 95 % once the CO2-LAMP readings reached the 3 e-folding time. The waterproofed K30 was then removed, allowed to re-equilibrate with the ambient laboratory air, and then re-submerged and allowed to reach the 3 e-folding time over three different submerged trials. Importantly, intervals for e-folding times were separately calculated for the individual submerged trials. Using Equations 4 and 5, values for K_p were then calculated using an estimated volume of 5.6 cm^3. Hereafter, $PCO2_{(aq)}$ refers to laboratory measurement of the partial pressure of dissolved CO_2.

The q constant values were determined by EXCEL Solver (Microsoft, Redmond, WA, USA) applying a least-sum-square error procedure, which uses a Generalized Reduced Gradient method (Gadagkar and Call, 2015). Calculated coefficients for curve steepness, c, were analyzed.

Submerged IRGA operation and validation

Seminal work by Johnson et al. (2010) on the construction of a passive, permeable membrane equilibrator suggested a depth-correction for IRGA output to account for increased hydrostatic pressure acting on a submerged gas analyzer. However, gas exchange will occur across a membrane until such time that PCO_2 is equal between the water and the membrane enclosed volume, irrespective of changes in the enclosed headspace volume brought on by increased hydrostatic pressure, suggesting that such a depth correction is not needed. To address this discrepancy related to potential effects of increasing hydrostatic pressure on membrane-enclosed IRGA operation, we explore the theory behind PCO_2 calculation for a membrane-enclosed submerged IRGA and describe laboratory experiments that we use to test the derived principles.

Submerged IRGA output: theoretical principles

In air, concentrations of CO_2 are typically reported by IRGAs as volumetric fractions, x_i, of CO_2 in dimensionless units either as parts per million volume (ppmv) or percent values for greater concentrations (> 10,000 ppm or 1%) where x_i may be expressed as

$$x_i = \frac{V_i}{V_{total}}, \tag{7}$$

where V_i equals the volume of CO_2 per total volume of gas, V_{total}. Alternatively, CO_2 in air may also be expressed as a partial pressure, PCO_2, from the product of x_i and total pressure (or sum of partial pressures, i.e. Dalton's Law), P_{total}:

$$PCO_2 = x_i P_{total}. \tag{8}$$

While P_{total} can be directly measured, or assumed to be near standard pressure, IRGAs do not directly measure x_i.

Principally, an IRGA measures the molecular density of CO_2 using the Beer-Lambert Law through the measured absorbance of CO_2 for a given wavelength (Fietzek et al., 2014). Molecular density, ρ, is expressed as $\rho = NCO_2/V_{total}$ where NCO_2 is the number of CO_2 molecules.

The x_i value from an IRGA is obtained using the ideal gas law, with

$$PCO_2 V_{total} = \frac{NCO_2}{N_A} RT, \quad (9)$$

$$PCO_2 = \frac{NCO_2}{V_{total}} \frac{RT}{N_A} = \rho \frac{RT}{N_A}, \text{ and} \quad (10)$$

$$x_i = \frac{PCO_2}{P_{total}} = \rho \frac{RT}{N_A P_{total}}, \quad (11)$$

where R is the universal gas constant, T is temperature in Kelvin and N_A is Avogadro's number. From Equation 7, x_i values depend on ρ, T, and P_{total}. If T and P_{total} are not measured, factory calibrated values for temperature, T_0, and pressure, P_0, are used to calculate a "reported" volume fraction, x_r, which is expressed as

$$x_r = \rho \frac{RT_0}{N_A P_0}. \quad (12)$$

For the majority of low-cost CO_2 gas analyzers, where T and P_{total} are not measured simultaneously, IRGA output will generally follow Equation 10 where T_0 and P_0 are at or near 25 °C and 1 atm, respectively. If T and P_{total} are measured, a corrected volume fraction, x_c, can be calculated with

$$x_c = x_r \frac{T}{T_0} \frac{P_0}{P_{total}}. \quad (13)$$

While the correction in Equation 11 is routinely employed for measurements of CO_2 concentrations in ambient air and soil, dissolved CO_2 concentrations are most commonly calculated from PCO_2, not a volumetric fraction. As can be seen in Equation 10, PCO_2 can be calculated directly from molecular density, ρ, temperature, and known constants. However, the

output given to us from the IRGA is x_r. To determine how to calculate PCO_2 from x_r, we can solve Equation 10 for ρ and substitute it into Equation 10, giving

$$PCO_2 = \frac{x_r N_A P_0}{RT_0}\frac{RT}{N_A} = \frac{x_r P_0 T}{T_0}. \quad (14)$$

Note that calculation of PCO_2 from the reported volumetric fraction only requires the calibration pressure (typically ~1 atm), not the pressure during measurement. On the other hand, a temperature correction does need to be applied if temperature during measurement is substantially different than during calibration.

Equation 12 demonstrates that, even with introduction of sensor operating principles, total pressure factors out of the calculation of PCO_2. Therefore, for a well-mixed, relatively shallow water body of equal temperature, salinity, and dissolved gas concentrations, the partial pressure of CO_2 measured by an IRGA at equilibrium (i.e. no gas exchange across the membrane) should be equal at all depths irrespective of hydrostatic pressure. Combining Equations 1 and 14, the concentration of CO_2 as determined from direct, membrane equilibration methods using an IRGA can be expressed as

$$C_i = \frac{PCO_2}{KCO_{2(T,S)}} = \frac{x_r P_0 T}{KCO_{2(T,S)} T_0}. \quad (15)$$

While the theoretical results suggest that no depth correction is needed for calculation of PCO_2, if a sensor is suddenly lowered to greater depths, compression of the membrane or sensor housing may introduce increases in total gas pressure within the IRGA. This will produce a short-term spike in the pressures of all gases, including CO_2. However, this produces disequilibrium between the gas pressures within the water and the IRGA, which will drive exchange across the membrane until dissolved gas pressure in the water and gas pressure in the IRGA are back in equilibrium.

Variable water depth experiments: laboratory simulation

An accompanying depth compensation experiment measuring CO_2 at multiple depth intervals (Figure 2C) was conducted to observe if $PCO_{2(aq)}$ values varied with submerged depth. A 7.62 cm inner diameter PVC pipe, 152.5 cm in length was filled with water (i.e. synthetic well) to accommodate varying depth interval measurements. The gas mixture was delivered via a porous stone at the bottom of the well. Initially, the submerged K30 recorded $PCO_{2(aq)}$ values to confirm equilibration. To begin the experiment, the K30 was removed from the well and allowed to re-equilibrate with laboratory atmospheric CO_2 concentrations and then quickly submerged to an initial depth of 20 cm and allowed to equilibrate. Once equilibrated, the probe was then dropped quickly from the 20 cm to the 70 cm depth and allowed to re-equilibrate. This process was further repeated for depth intervals of 100 and 140 cm.

Field trials

Field trials were carried out at Blowing Springs Cave and the Savoy Experimental Watershed located in Northwest Arkansas, USA (Figure 3). The two sites represent karst environments within the Springfield Plateau physiographic province overlying the Springfield Plateau aquifer (Kresse et al., 2014). The Springfield Plateau province can be characterized as a mantled karst terrain consisting of a cherty regolith overlying the Boone Formation, a cave-forming Paleozoic carbonate unit (Brahana et al., 1999; Knierim et al., 2013; Al-Qinna et al., 2014; Jarvie et al., 2014).

Blowing Springs Cave

At Blowing Springs Cave, both cave air, $CO_{2(air)}$ and dissolved CO_2 within the cave stream, $PCO_{2(stream)}$ were measured independently by: 1. the CO2-LAMP, and 2. an enclosed membrane-equilibrator similar to Johnston et al. (2010) using a Vaisala GMT220 (Helsinki,

Finland), hereafter referred to as the 'Vaisala'. Along with measuring $CO_{2(air)}$ and $PCO_{2(stream)}$, a Campbell Scientific (Logan, UT) CS451 sensor was used to record absolute pressure in the cave air and water temperature. Vaisala $CO_{2(air)}$, Vaisala $PCO_{2(stream)}$, absolute pressure, and temperature values were logged using a Campbell Scientific CR850. Sensors were located approximately 100 m within the cave. For $CO_{2(air)}$ and $PCO_{2(stream)}$, waterproofed IRGA sensors were placed alongside each other. Monitoring using the CO2-LAMP lasted from 25 February to 9 March 2017.

Percent differences between the Vaisala and CO2LAMP were calculated for measurements of $CO_{2(air)}$ and $PCO_{2(stream)}$, respectively:

$$\% = 100 \times \frac{|CO_{2,CO2LAMP} - CO_{2,Vaisala}|}{\frac{(CO_{2,CO2LAMP} + CO_{2,Vaisala})}{2}}. \quad (17)$$

Savoy Experimental Watershed

The Savoy Experimental Watershed (SEW) is a long-term experimental research station owned by the University of Arkansas encompassing numerous karst features including sinking streams, caves, cave springs, and epikarst springs (Brahana et al., 1999; Al-Qinna et al., 2014; Covington and Vaughn, 2018). Soil series at SEW have been previously classified as Clarksville (Loamy-skeletal, siliceous, semiactive, mesic Typic Paleudults), Nixa (Loamy-skeletal, siliceous, active, mesic Glossic Fragiudults), Razort (Fine-loamy, mixed, active, mesic Mollic Hapludalfs), and Pickwick (Fine-silty, mixed, semiactive, thermic Typic Paleudults) (Soil Survey Staff, 2019). Soils consist of very deep, moderately to excessively drained, slow to moderately permeable soils with clay contents ranging from 20 to 50% (Soil Survey Staff, 2019).

Soil CO_2 concentrations at the SEW are reported for the period of 9 July to 22 July 2017 and were measured approximately 3 m from a centrally located weather station. $CO_{2(soil)}$ was

measured at approximate 10 cm depth within a soil cavity with the dimensions of ~ 10 cm depth and 4 cm diameter. A small opening was dug into the wall of the soil cavity where the sensor was placed laterally in the base of the cavity wall. The soil cavity was back-filled as to minimize soil disturbance. At the weather station, measurements of air temperature, soil moisture, and rainfall were recorded every 5 minutes.

Data processing

During field deployments, the low-power mode Arduino sketch was used to record measurements. Post-processing consisted of removal of data during warm-up and stabilization periods and selecting a final, stabilized value (Figure 4A-D). Final values measured during measurement cycles at Blowing Springs for cave air and dissolved CO_2 and soil CO_2 at SEW are reported here.

At Blowing Springs, stabilization periods for the sensor during warm-up changed through the monitoring period (Figure 5). Using a heuristic approach, the Hill equation (Hill, 1910)—a non-linear, four-parameter equation—was fit to data collected during the monitoring after 100 seconds to evaluate changes in stabilization times over the monitoring period. Fitting to the data after 100 seconds minimized influence of the initial CO_2 peak (Figure 4A). In general, the Hill equation is useful in describing experimental data that are sigmoid in shape where multiple non-linear processes may be present (Goutelle et al., 2008; Gadagkar and Call, 2015).

The formulation of the Hill equation used in this study was

$$y = d + \left(\frac{a-d}{1+\left(\frac{b}{t}\right)^c}\right), \quad (16)$$

where the coefficients calculated for this study were: *d*, the initial CO_2 value; *a*, the final CO_2 value; b, the time at which the PCO_2 value has changed halfway between *a* and *d*; *c,* the "Hill

Slope" or "steepness" value (Gadagkar and Call, 2015); and t, is the time elapsed during the measurement period. Coefficient values were also determined by EXCEL Solver applying a least-sum-square error procedure, as previously described. Calculated coefficients for curve steepness, *c*, were analyzed.

CO2-LAMP $CO2_{(air)}$ and Vaisala $CO_{2(air)}$ data were corrected using Equation 11 from ancillary pressure and temperature measurements made in the cave. CO2-LAMP $PCO2_{(stream)}$ and Vaisala $PCO_{2(stream)}$ values were corrected using water temperature data (Equation 12).
At Blowing Springs, measurements with the CO2-LAMP and Vaisala included cave stream temperature, cave air temperature, and cave air pressure, but were recorded at slightly different intervals. Vaisala CO_2 values and environmental parameters (i.e. cave air, cave stream temperature, and cave air pressure) were linearly interpolated between timestamps for direct comparison to CO2-LAMP measurements.

Data analysis

Assessment of bivariate relations were carried by correlation and regression analyses using the PAST statistical software package (Hammer et al., 2001). Specific relations assessed were between: 1, $CO_{2(Vaisala)}$ and $CO_{2(CO2\ LAMP)}$ for measurements in cave air and dissolved CO_2 in the cave stream, respectively; and 2, between $CO_{2(soil)}$ within the shallow soil cavity and soil moisture content measured at SEW.

Results

Reference measurements to known gas mixtures

Gas-equilibrated reference measurements of CO_2 and PCO_2 using the CO2-LAMP were within the accuracy stated by the manufacturer for the K30 1% and 10% IRGAS, respectively, in

both dry and aqueous environments. In the submerged reference gas mixture experiments, the time needed for the water to reach three e-folding intervals (or 95 % equilibration) from the onset of gas flow from the diffusing stone into the water and measured through exchange by the waterproofed K30 was ~ 86 minutes for a volume of ~ 2.5 liters (Figure 6A). Once the measurements read by waterproofed K30 reached three e-folding times, the waterproofed K30s were removed from the water and allowed to re-equilibrate with laboratory ambient air. The K30s were then re-submerged three separate times for a minimum period to reach three e-folding times for each of the three submerged periods, respectively, (Figure 6B-D). The average effective K_p value calculated was 1.2 x 10^{-4} cm^2 s^{-1}, which, while nearly two orders of magnitude lower than CO_2 diffusivity through ePTFE from air-to-air environments (0.01 cm^2 s^{-1}; Johnson et al., 2009), is nearly an order of magnitude greater than diffusivity of CO_2 in water (1.77 x 10^{-5} cm^2 s^{-1} at 20 °C; Scott, 2000).

Variable depth trials

Equilibrated PCO_2 values did not vary with submergence depth (Figure 7). As predicted, however, there were repeated patterns of an initial sharp increase in PCO_2 followed by a decline to imposed PCO_2 values upon rapid lowering of the K30 to greater depth. For all depth values, measured CO_2 values stabilized within 1 % of the imposed dissolved CO_2 concentrations imposed by the reference gas.

Blowing Springs Cave $CO_{2(air)}$ and $CO_{2(stream)}$

Measurements of $CO_{2(air)}$ and $PCO_{2(stream)}$ between the Vaisala and CO2-LAMP measurements did not appear to vary randomly during the monitoring period. The largest differences between $CO_{2(air)}$ values for the two instruments were observed during temperature peaks and coincided with cave air flow reversals. Differences in $PCO_{2(stream)}$ between the Vaisala

and CO2-LAMP appeared to exhibit a quasi-oscillatory behavior and some covariation was observed between measurement differences and curvature (or *c* coefficient) values calculated from the Hill-equation fits to the equilibration curves for the CO2-LAMP. Overall, measurements of $CO_{2(air)}$ ($r^2 = 0.97$, $p <<< 0.05$) and $PCO_{2(stream)}$ ($r^2 = 0.99$, $p <<< 0.05$) between the Vaisala and CO2-LAMP platform were well correlated during the monitoring period (Figure 8).

During the field test, $CO_{2(air)}$ exhibited two pronounced periods of greater concentrations when cave air flow was outward from the main cave entrance (data not shown here; Covington et al., in prep). Overall, $CO_{2(air)}$ increased over the monitoring period. Notably, broader CO_2 peaks in $PCO_{2(stream)}$ were observed following periods of increased $CO_{2(air)}$ (Figure 9A).
Percent and ppmv differences between the Vaisala and CO2-LAMP for $CO_{2(air)}$ ranged from 2.1 to 20.9 % and 13 to 147 ppmv, respectively (Figure 9B). Percent and ppmv differences between the Vaisala and CO2-LAMP for $PCO_{2(stream)}$ ranged from 1.3 to 11.9 % and 16 to 147 ppmv, respectively, and exhibited a slight overall increase in percent difference during deployment (Figure 9C). Median percent and ppmv differences between $CO_{2(air)}$ and $PCO_{2(stream)}$ were 11.6 % and 56 ppmv and 8.1 % and 92 ppmv, respectively. Values for $CO_{2(air)}$ measured using a K30 1% were often outside specific absolute accuracy ±30 ppmv ±3% stated for the K30. Values for $PCO_{2(stream)}$ measured using the K30 10%, however, were within the stated absolute accuracy of ±300 ppmv ±3%.

Savoy Experimental Watershed $CO_{2(soil)}$

Measurements of $CO_{2(soil)}$ at SEW exhibited both diurnal variation and an overall decline during the monitoring period. The daily amplitude of CO_2 variation ranged from 1170 to 5460 ppm with daily minimum and maximum values of $CO_{2(soil)}$ observed at approximately mid-night

and mid-day (local time), respectively. Similar timing of minimum and maximum $CO_{2(soil)}$ values were also reported by Hirano et al. (2003). During the monitoring period, a light rain event occurred on 14 July evident from small rainfall totals and reduced daily temperatures, but no change in soil moisture was observed. However, $CO_{2(soil)}$ values decreased over 7000 ppm from 14 to 15 July, increasing into 16 July, and subsequently decreasing over the remainder of the monitoring period. Overall, daily median $CO_{2(soil)}$ values were well correlated with daily median soil moisture values ($r^2 = 0.84$, $p <<< 0.05$).

Discussion

Measurement accuracy and assessment

Laboratory reference experiments using a known, imposed reference $PCO_{2(aq)}$ value demonstrated the viability of waterproofing a K30 sensor for direct measurement of the partial pressure of dissolved CO_2. Initial offsets and drift that might have occurred during and post-laboratory measurements were not assessed; however, accounting for any drift over the ~ 12 hour period would have had negligible difference for reported $PCO_{2(aq)}$ values and the outcome of the reference experiments. Moreover, observed differences between reference values and the K30 $PCO_{2(aq)}$ were well within similar percent differences as between active membrane equilibrators and headspace measurements without zero-offset or drift corrections (Abril et al., 2015).

Comparatively, the Vaisala IR source generates more heat than the light source in the K30. In turn, the Vaisala heating element potentially allows for faster removal of any moisture within the IRGA given 100 % humidity conditions, which can interfere with measurement magnitude and stability. Specifically, greater initial PCO_2 concentrations for CO2-LAMP data

during warm-up periods (Figure 4A-C) could be resultant from liquid water condensate decreasing light intensity at the infrared detector (i.e. resulting in artificially large CO_2 values) (Fietzek et al., 2014). Measurement stability over time was likely better sustained in the Vaisala given the ability to remove excess moisture over deployment periods.

IRGA principle operation and PCO_2 depth dependence

Based on both theoretical principles and empirical evidence, the measurement of partial pressure of CO_2 using a submerged IRGA in equilibrium with surrounding water is independent of hydrostatic pressure (Equation 17; Figure 7). However, CO_2 concentration spikes occur during sudden increases in hydrostatic pressure (i.e., submerging to deeper depths) before the submerged IRGA returns to the reference CO_2 value. This temporary increase in CO_2 is interpreted to indicate compression of the enclosed membrane volume followed by a period of re-equilibration.

More specifically, when the enclosed membrane volume is compressed, this leads to a decrease in the gas volume, V_{total}, which: 1. increases the molecular density of CO_2 without adding more CO_2 molecules; whereby 2. a greater CO_2 concentration is measured by the IRGA due to greater molecular density; and 3. the total gas pressure inside the enclosed membrane volume is then in disequilibrium with the total dissolved gas pressure of the water. In this experiment, as N_2 was the predominant species present in the reference gas, total pressure equilibration was driven by N_2. As total pressure within the enclosed membrane re-equilibrated with the total dissolved gas pressure of the water (i.e. N_2 exchange), the remaining gas exchange was driven by re-equilibration of partial pressures of the dissolved CO_2. Overall from empirical experiments, the timescale associated with equilibration of the waterproofed IRGA upon submergence was approximately 20 minutes.

Assuming an initial V_{total} of 5 cm^3 and rearranging Equation 14, a volume change of 6.7 % would produce the observed increase in PCO_2 of approximately 150 ppmv during the 20 to 70 cm variable depth experiment from the 0 minute to 20 minutes of elapsed time (Figure 7C). Given the K30 model materials and waterproofing components being partially flexible, this percent change was within reason.

Importantly, accounting for increased hydrostatic pressure acting on the sensor (Johnson et al., 2009) with depth gives rise to overestimates of PCO_2, and these overestimates are proportional to the submerged depth. Assuming a water density of 1000 kg/m^3, every 10 cm imparts an increase in hydrostatic pressure equivalent to 9.81 hPa, which would equal an approximate 8.8 & overestimation per meter. Considering the comparative accuracy of dissolved CO_2 measurement between various equilibration methods to be approximately 15 % (Abril et al., 2015; Yoon et al., 2016), an equal value of overestimation because of the hydrostatic pressure correction is incurred at only 1.68 m depth.

Field instrument comparison

Overall, measured CO_2 relations between the Vaisala and CO2-LAMP for $CO_{2(air)}$ and $PCO_{2(stream)}$ covaried linearly and were statistically significant ($r^2 > 0.97$, $p <<< 0.005$). As previously mentioned, broader inter-comparison assessments of manual, active, and passive equilibration methods for direct PCO_2 measurement exhibited average differences of ~15 % between measurement methods from field sampling (Abril et al., 2015; Yoon et al., 2016). Observed differences for $PCO_{2(stream)}$ between the Vaisala and CO2-LAMP in this study were only 8.6 % and were nearly constant. For both $CO_{2(air)}$ and $PCO_{2(stream)}$, differences between the Vaisala and CO2-LAMP likely arose from the varying ability to drive off moisture build up inside the IRGA. Related effects from moisture interference, such as band broadening, effective

pressure, and, particularly, water dilution effects (McDermitt et al., 1993; Welles and McDermitt, 2005), will affect IRGA accuracy, but were ultimately not fully assessed in this study. The specific factors and correction coefficients for these factors vary not only between manufacturers, but for individual IRGAs of the same manufacturer (McDermitt et al., 1993; Martin et al., 2017). Fully explaining observed differences between $CO_{2(air)}$ and $PCO_{2(stream)}$ were outside of the scope of this study, but accounting for humidity, temperature, and pressure within the membrane-enclosed headspace for the K30 and Vaisala would certainly increase accuracy.

Capturing CO_2 variability in natural settings

Variations in $CO_{2(air)}$ and $PCO_{2(stream)}$ recorded by the CO2-LAMP at Blowing Springs mirrored CO_2 variability recorded by the Vaisala, albeit with values that were overestimated. At SEW, $CO_{2(soil)}$ variability exhibited similar ranges and environmental response to soil CO_2 variability observed by previous studies (Hirano et al., 2003; Jassal et al., 2005). Overall, the CO2-LAMP captured sub-daily CO_2 variability at a temporal resolution comparable to values obtained from greater-cost passive-membrane equilibration platforms.

Carbon dioxide variability at both sites may be generally described as arising from complex carbon exchange pathways and biogeochemical cycling, which vary down to hourly time-scales. At Blowing Springs Cave, large changes in $CO_{2(air)}$ and $PCO_{2(stream)}$ are linked to cave ventilation and air flow reversals in the cave system; when $CO_{2(air)}$ increases, the flux of CO_2 from the stream decreases, subsequently increasing $PCO_{2(stream)}$. At SEW, $CO_{2(soil)}$ decreases over the monitoring period are likely related to changes in soil moisture (i.e. drying) and corresponding reduced soil respiration (Hirano et al., 2003). Increasing 'noise' observed in soil moisture content measurements with lower soil moisture content observed in this study is well

documented at other localities and are characteristic of loamy sand, silt loam, and clay loam soils present at SEW (see Vereecken et al., 2007 and references therein).

Instrument fouling, future fabrication, and field deployment

From initial deployments of the CO2-LAMP system, environmental factors have been noted which may have solely or in part caused temporary and permanent K30 instrument fouling. First, suspended sediments and other materials (e.g. branches, shells, etc.) can abrade the membrane surface causing microtears. Microtears, while not always visible, allow for liquid water to seep through and damage the K30 instrument's components. Second, upon epoxy application and waterproofing of the K30, careful attention is needed to ensure the rubber compound seals the contact between the serial cable, epoxy, and plastic case to prevent water intrusion to the K30 from openings that, similar to microtears, are not always visually apparent. Moreover, application of the rubber compound greatly aids strain relief for the serial cable exiting the plastic case. Third, silt and smaller clay size particles can accumulate on the membrane surface particularly if oriented 'face up' relative to the stream surface. If left unprotected, a mud layer or biofilm can accumulate. In both cases, dissolved CO_2 concentrations would be more influenced by dissolved CO_2 changes within the mud or algal boundary rather than the surrounding water. For protection against sediment and biofilm buildup on the membrane surface, it is recommended to orient the sensor vertically in the water column or 'face down' relative to the stream surface. For biofilms specifically, use of a bronze mesh has been found to be successful in preventing biofilm accumulation in other freshwater and marine environments (Steven et al., 2014).

Recommendations for future, long-term field deployments using a design similar to that presented should consider two modifications. During fabrication, a conformal coating was not

applied in this study; however, previous studies employing the K30 for use in floating chambers noted utility in application of a protective coating on electronic components both during assembly and field operation (Bastviken et al., 2015). In terms of bolstering the waterproofing of the K30, a conformal coating would serve as a protective layer with no disturbance to the K30 circuit board. Importantly, the conformal coating also provides additional structural support to the initial UART serial connection made to the circuit board before attaching the membrane and rubber compound coating and may help limit any effects from contraction or expansion of the epoxy-resin during curing.

Lastly, inability to remove excess condensation that results from membrane saturation (Manning et al., 2003) or in-stream temperature changes will greatly diminish instrument accuracy and potentially cause permanent instrument fouling over time (Fietzek et al., 2014). While condensation buildup was not directly investigated, removal of excess moisture is warranted for long-term CO2-LAMP deployment and CO_2 accuracy.

Conclusions

Expanding the variety of sites and frequency of CO_2 measurements in ambient, soil, and aqueous environments are critical in constraining local carbon dynamics and addressing gaps in efforts to quantify the planetary-scale carbon cycle. Reduction of instrument costs provides a pathway to expand CO_2 monitoring across Earth, particularly in research programs where relatively greater-cost platforms are cost-prohibitive.

As part of the CO2-LAMP development, a theoretical presentation of IRGA output and accompanying experimentation demonstrate that, for PCO_2 measurements, temperature is the only correcting variable; however, for measurements in ambient air, total pressure is needed for calculating x_c (i.e. pressure- and temperature-corrected values). Importantly, these findings hold

significant implications for past, current, and future implementation of IRGA analyzers for dissolved PCO_2 measurement, and, where applicable, recalculation of reported values from previous studies should be considered, particularly for probes at deeper water depths. Recorded observations in both the laboratory and field demonstrate the CO2-LAMP to be a viable, low-cost alternative to monitoring CO_2 in field settings. In the case of $PCO_{2(aq)}$, reported values were within reported uncertainties between different methods. Future work will modify the gas analyzer-water interface to minimize potential fouling due to moisture intrusion and/or long-term condensation buildup.

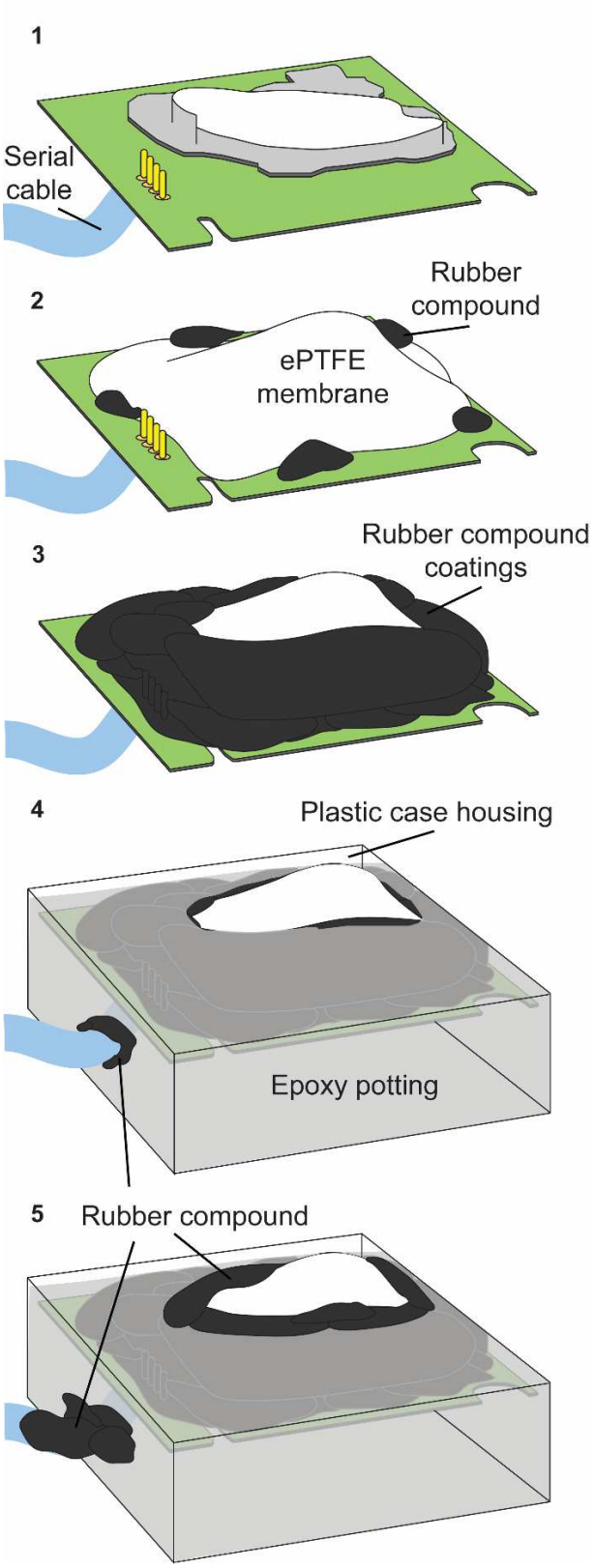

Figure 1. Simplified schematic of step-wise waterproofing of K30 sensor.

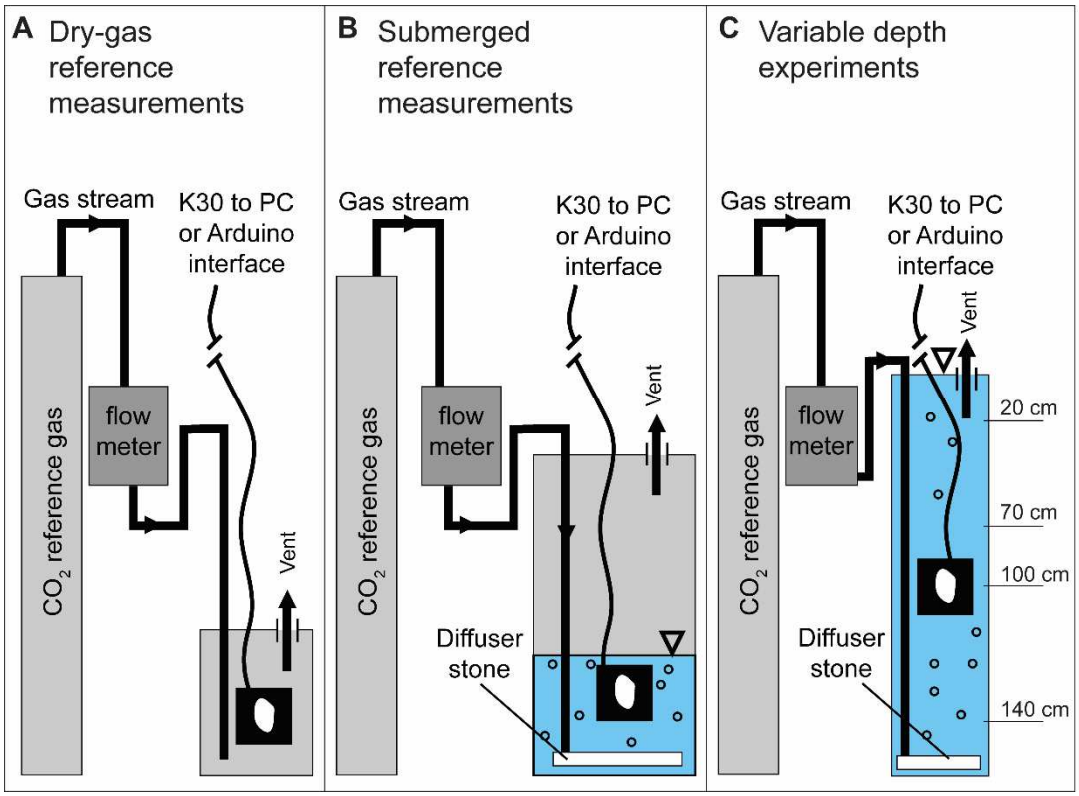

Figure 2. Schematic of reference measurement configurations for **A)** dry-gas, **B)** submerged, PCO_2, and **C)** variable depth experiments. Note: Not to scale.

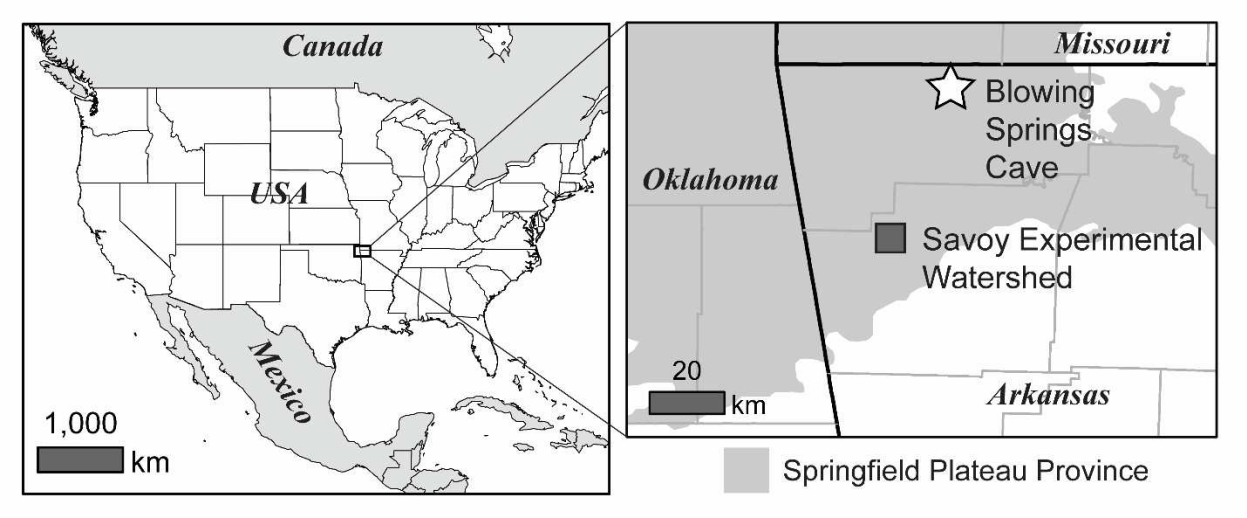

Figure 3. Location of Blowing Springs Cave and the Savoy Experimental Watershed located within the Springfield Plateau physiographic province in northwestern Arkansas, USA.

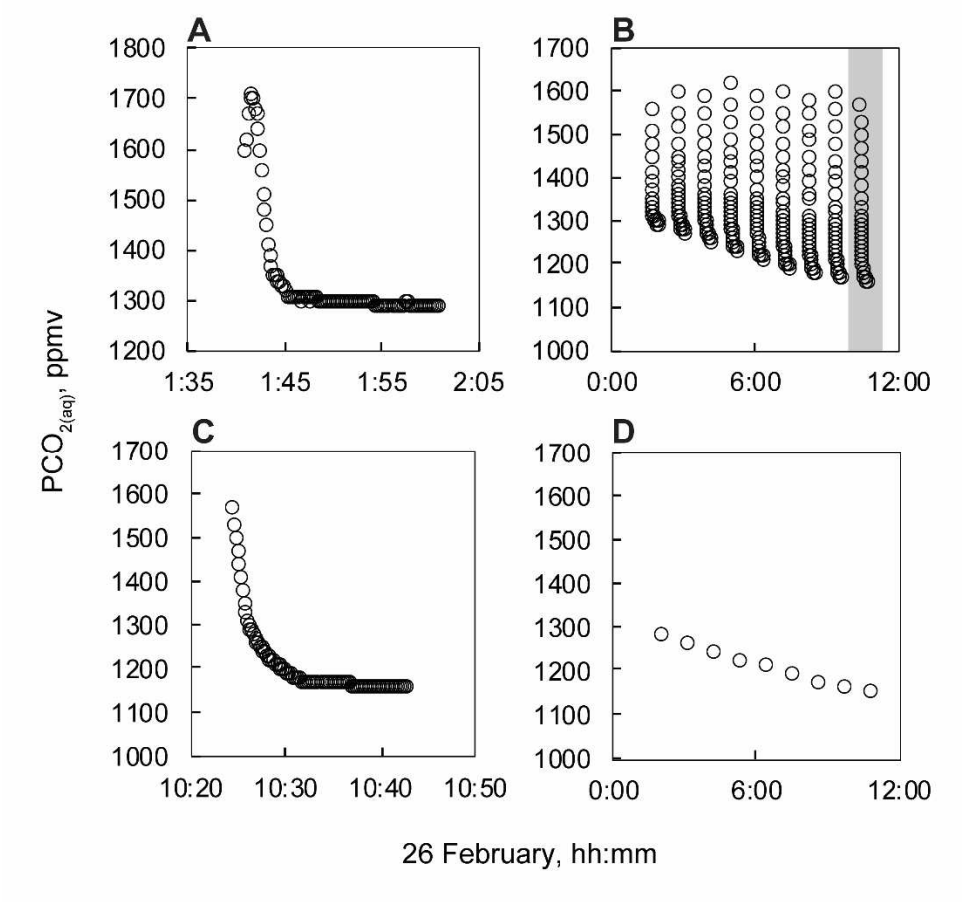

Figure 4. A-D) Post-processing steps for $PCO_{2(stream)}$ data. **A)** Example of full measurement cycle data, which includes initial peak in first 100 seconds. **B)** Example of initial filtering removing first 100 seconds of measurement cycles for nine measurement cycles on 26 February. **C)** The last measurement value during each measurement cycle was selected as the 'stabilized' values for comparison with Vaisala data. **D)** Example of filtered from data set in panel B.

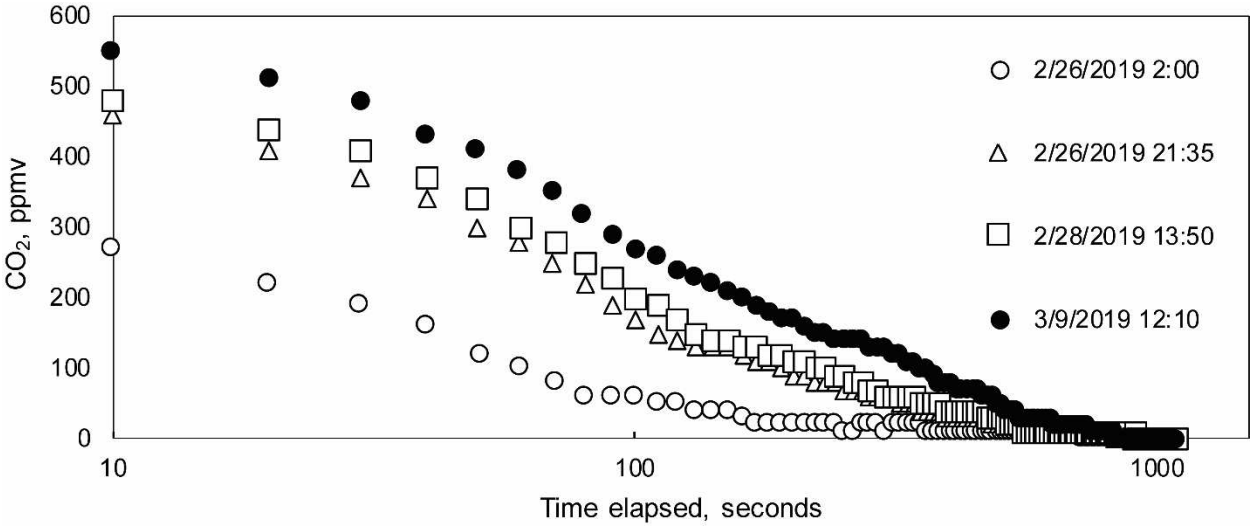

Figure 5. Progressive change in $PCO_{2(stream)}$ stabilization curves through monitoring period.

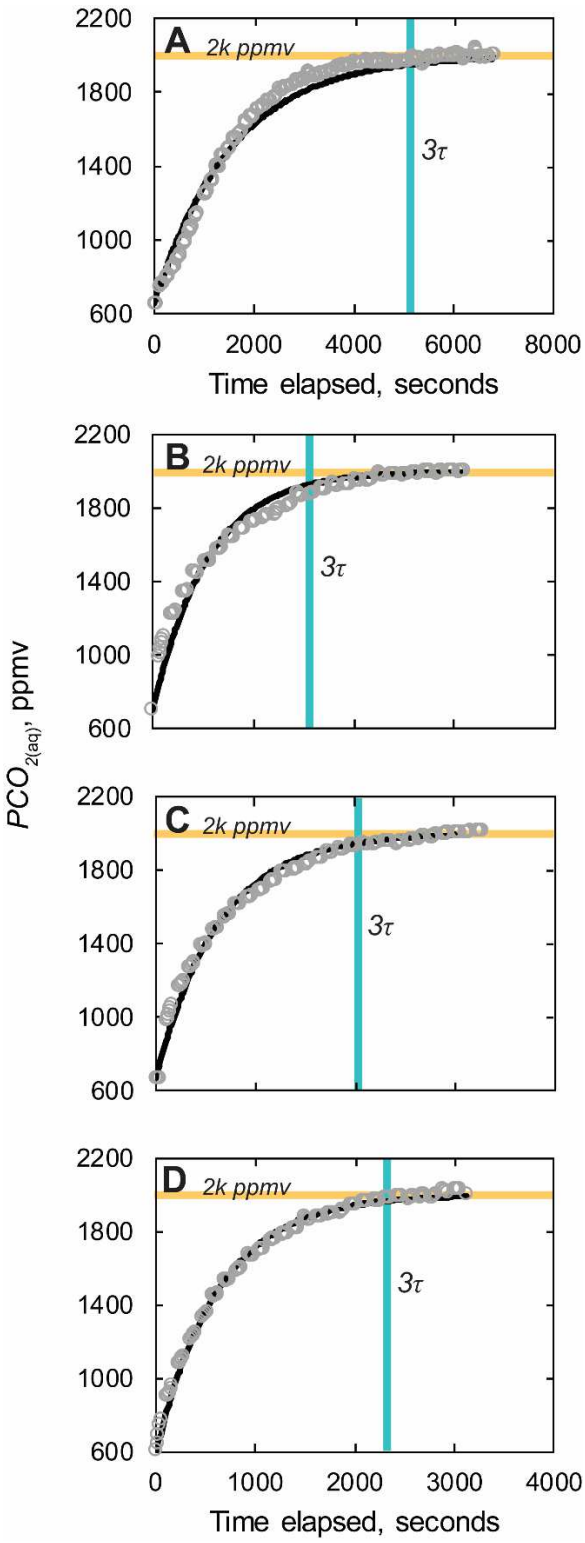

Figure 6. A) $PCO_{2(aq)}$ measured during injection of 2000 ppmv reference gas. **B-D)** PCO2(aq) re-equilibration after equilibration of water to reference gas. Modeled exponential fits are solid black lines. Horizontal orange line, 2k ppmv, denotes 2000 reference PCO2(aq) value. Vertical blue line indicated 3 e-folding time, 3τ, or ~ 95 % equilibration.

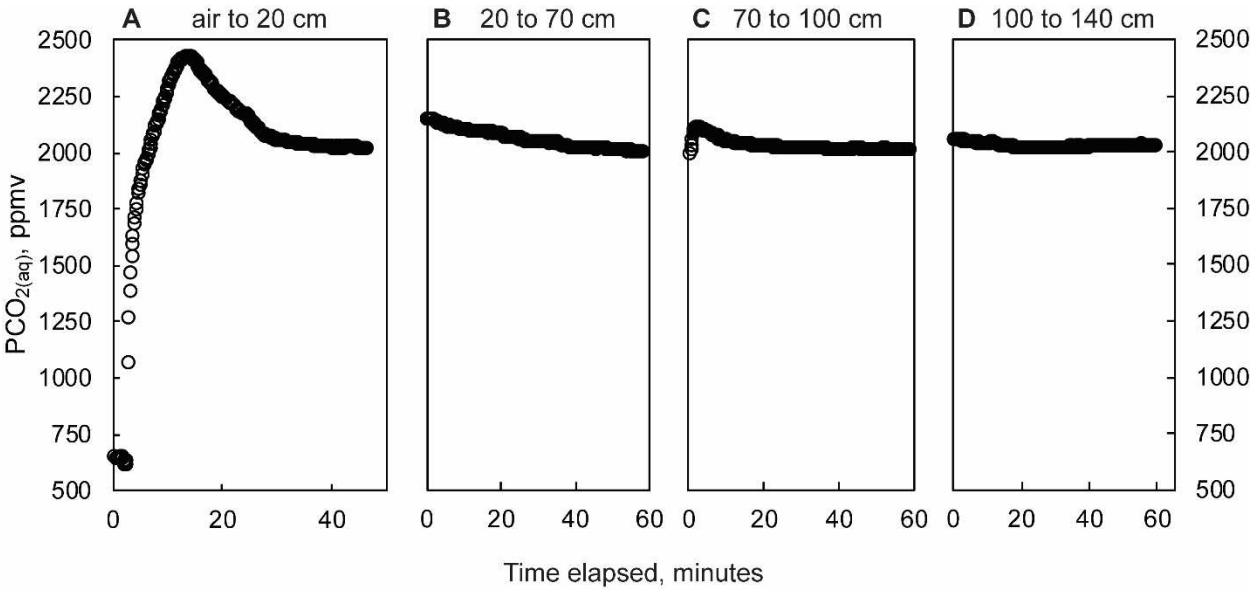

Figure 7. Change in $PCO2_{(aq)}$ and time elapsed lowering from **A)** air to 20 cm, **B)** 20 to 70 cm, **C)** 70 to 100 cm, and **D)** 100 to 140 cm depth intervals. Note: Recorded values missed initial peaks when submerged for B (20 to 70 cm) and D (100 to 140 cm) due to lagged start time on data logger.

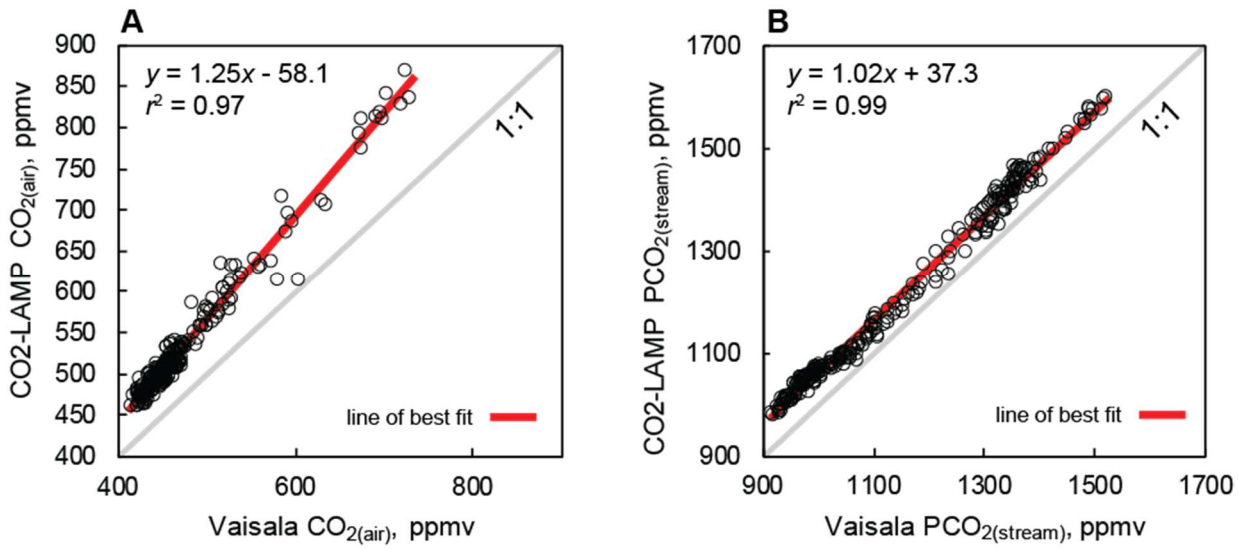

Figure 8. CO2-LAMP versus Vaisala measurements for **A)** $CO_{2(air)}$ and **B)** Vaisala $PCO_{2(stream)}$.

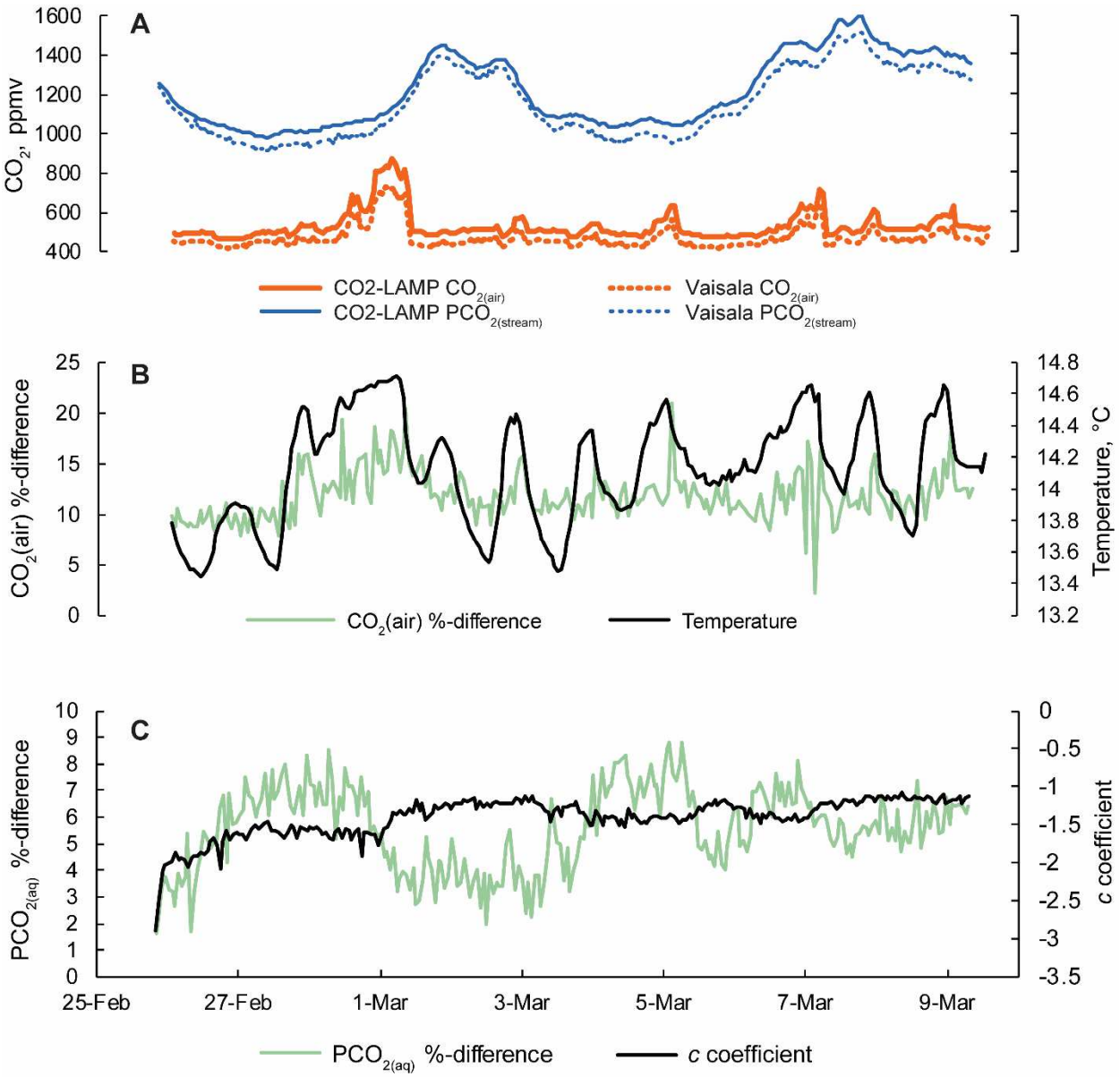

Figure 9. A) Concurrent measurements of $CO_{2(air)}$ and $PCO_{2(stream)}$ collected by the CO2-LAMP and Vaisala platforms from 26 February to 9 March 2017. **B)** Percent difference for $CO_{2(air)}$ between the CO2-LAMP and Vaisala and changes in cave air temperature over the monitoring period. C) Percent differences for $PCO_{2(stream)}$ between the CO2-LAMP and Vaisala and changes in curvature (i.e. *c* coefficient) derived from the Hill-equation.

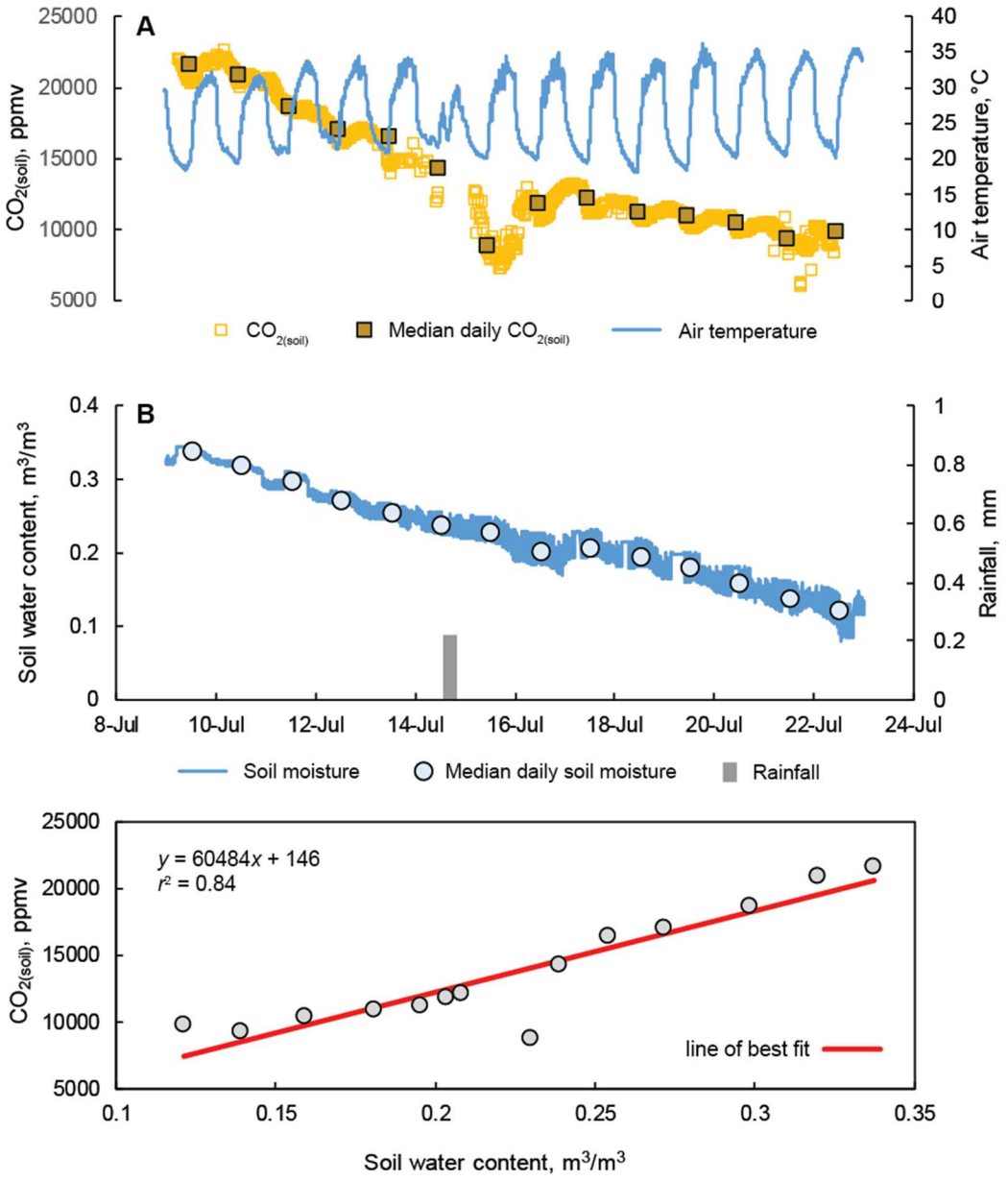

Figure 10. A) Hourly $CO_{2(soil)}$ concentrations and median daily values from a 10 cm soil cavity and overlying air temperature from 9 to 24 July at the Savoy Experimental Watershed. **B)** Fifteen-minute interval measurement of soil moisture, median daily soil moisture values, and rainfall totals measured from a weather station located approximately 2 m from the soil cavity. **C)** $CO_{2(soil)}$ versus soil water content and derived linear line of best fit.

References Cited

Abril, G. et al., 2015, Technical note: Large overestimation of pCO2 calculated from pH and alkalinity in acidic, organic-rich freshwaters: Biogeosciences, v. 12, p. 67–78, doi:10.5194/bg-12-67-2015.

Al-Qinna, M., Scott, H.D., Brye, K.R., Van Brahana, J., Sauer, T.J., and Sharpley, A., 2014, Coarse fragments affect soil properties in a mantled-karst landscape of the ozark highlands: Soil Science, v. 179, p. 42–50, doi:10.1097/SS.0000000000000034.

Andrews, A.E. et al., 2014, CO2, CO, and CH4 measurements from tall towers in the NOAA Earth System Research Laboratory's Global Greenhouse Gas Reference Network: instrumentation, uncertainty analysis, and recommendations for future high-accuracy greenhouse gas: Atmospheric Measurement Techniques, v. 7, p. 647–687, doi:10.5194/amt-7-647-2014.

Bareer, R.M., 1939, Permeation, diffusion and solution of gases: Trans. Faraday soc., v. 35, p. 628–643.

Bastviken, D., Sundgren, I., Natchimuthu, S., Reyier, H., and Gålfalk, M., 2015, Technical Note: Cost-efficient approaches to measure carbon dioxide (CO2) fluxes and concentrations in terrestrial and aquatic environments using mini loggers: Biogeosciences, v. 12, p. 3849–3859, doi:10.5194/bg-12-3849-2015.

Beddows, P.A., and Mallon, E.K., 2018, Cave Pearl Data Logger: A Flexible Arduino-Based Logging Platform for Long-Term Monitoring in Harsh Environments: Sensors, v. 18, p. 530, doi:10.3390/s18020530.

Bradford, M.A., Wieder, W.R., Bonan, G.B., Fierer, N., Raymond, P.A., and Crowther, T.W., 2016, Managing uncertainty in soil carbon feedbacks to climate change: Nature Climate Change, v. 6, p. 751–758, doi:10.1038/nclimate3071.

Brahana, J.V., Hays, P.D., Kresse, T.M., Sauer, T.J., and Stanton, G.P., 1999, The Savoy Experimental Watershed–Early Lessons for Hydrogeologic Modeling From a Well-Characterized Karst Research Site, in Palmer, A.N., Palmer, M.V., and Sasowsky, I.D. eds., Karst Waters Institute Special Publication 5, Charles Town, WV, Karst Waters Institute, p. 247–254.

Brantley, S.L. et al., 2016, Designing a suite of measurements to understand the critical zone: Earth Surface Dynamics, v. 4, p. 211–235, doi:10.5194/esurf-4-211-2016.

Brantley, S.L., Goldhaber, M.B., and Vala Ragnarsdottir, K., 2007, Crossing disciplines and scales to understand the critical zone: Elements, v. 3, p. 307–314, doi:10.2113/gselements.3.5.307.

Breecker, D., and Sharp, Z.D., 2008, A field and laboratory method for monitoring the concentration and isotopic composition of soil CO2: Rapid Communications in Mass Spectrometry, v. 22, p. 449–454, doi:10.1002/rcm.3382.

Broecker, W.S., and Sanyal, A., 1998, Does atmospheric CO2 police the rate of chemical weathering? Global Biogeochemical Cycles, v. 12, p. 403–408, doi:10.1029/98GB01927.

Burton, M.R., Sawyer, G.M., and Granieri, D., 2013, Deep Carbon Emissions from Volcanoes: Reviews in Mineralogy and Geochemistry, v. 75, p. 323–354, doi:10.2138/rmg.2013.75.11.

Covington, M.D., and Vaughn, K.A., 2018, Carbon dioxide and dissolution rate dynamics within a karst underflow-overflow system, Savoy Experimental Watershed, Arkansas, USA: Chemical Geology, p. 0–1, doi:10.1016/j.chemgeo.2018.03.009.

Cressey, D., 2017, Toolbox: Age of the Arduino: Nature, v. 544, p. 125–126, doi:10.1038/544125a.

D'Aoust, B.G., and Clark, M.J.R., 1980, Analysis of Supersaturated Air in Natural Waters and Reservoirs: Transactions of the American Fisheries Society, v. 109, p. 708–724, doi:10.1577/1548-8659(1980)109<708:AOSAIN>2.0.CO;2.

Davidson, E.A., Figueiredo, R.O., Markewitz, D., and Aufdenkampe, A.K., 2010, Dissolved CO2 in small catchment streams of eastern Amazonia: A minor pathway of terrestrial carbon loss: Journal of Geophysical Research: Biogeosciences, v. 115, p. 1–6, doi:10.1029/2009JG001202.

Decina, S.M., Hutyra, L.R., Gately, C.K., Getson, J.M., Reinmann, A.B., Short Gianotti, A.G., and Templer, P.H., 2016, Soil respiration contributes substantially to urban carbon fluxes in the greater Boston area: Environmental Pollution, v. 212, p. 433–439, doi:10.1016/j.envpol.2016.01.012.

Deman, K.L. et al., 2007, The phylogeography of Amazonia revisited: new evidence from riodinid butterflies., in Solomon, S., Qin, D., Manning, M., Chen, Z., Marquis, M., Averyt, K.B., Tignor, M., and Miller, H.L. eds., Cambridge, United Kingdom and New York, NY, USA, Cambridge University Press, Climate Change 2007: The Physical Science Basis. Contribution of Working Group I to the Fourth Assessment Report of the Intergovernmental Panel on Climate Change.

Enns, T., Scholander, P.F., and Bradstreet, E.D., 1965, Effect of hydrostatic pressure on gases dissolved in water: Journal of Physical Chemistry, v. 69, p. 389–391, doi:10.1021/j100886a005.

Fietzek, P., Fiedler, B., Steinhoff, T., and Körtzinger, A., 2014, In situ quality assessment of a novel underwater pCO2 sensor based on membrane equilibration and NDIR spectrometry: Journal of Atmospheric and Oceanic Technology, v. 31, p. 181–196, doi:10.1175/JTECH-D-13-00083.1.

Fisher, D.K., and Gould, P.J., 2012, Open-source hardware is a low-cost alternative for scientific instrumentation and research: Modern Instrumentation, v. 1, p. 8–20, doi:10.4236/mi.2012.12002.

Florea, L.J., 2015, Carbon flux and landscape evolution in epigenic karst aquifers modeled from geochemical mass balance: Earth Surface Processes and Landforms, v. 40, p. 1072–1087, doi:10.1002/esp.3709.

Frankignoulle, M., Borges, A., and Biondo, R., 2001, A new design of equilibrator to monitor carbon dioxide in highly dynamic and turbid environments: Water Research, v. 35, p. 1344–1347, doi:10.1016/S0043-1354(00)00369-9.

Gadagkar, S.R., and Call, G.B., 2015, Computational tools for fitting the Hill equation to dose–response curves: Journal of Pharmacological and Toxicological Methods, v. 71, p. 68–76, doi:10.1016/J.VASCN.2014.08.006.

Gardner, P., and Solomon, D.K., 2009, An advanced passive diffusion sampler for the determination of dissolved gas concentrations: Water Resources Research, v. 45, p. 1–12, doi:10.1029/2008WR007399.

Goutelle, S., Maurin, M., Rougier, F., Barbaut, X., Bourguignon, L., Ducher, M., and Maire, P., 2008, The Hill equation: a review of its capabilities in pharmacological modelling: Fundamental & Clinical Pharmacology, v. 22, p. 633–648, doi:10.1111/j.1472-8206.2008.00633.x.

De Gregorio, S., Camarda, M., Longo, M., Cappuzzo, S., Giudice, G., and Gurrieri, S., 2011, Long-term continuous monitoring of the dissolved CO2 performed by using a new device in groundwater of the Mt. Etna (southern Italy): Water Research, v. 45, p. 3005–3011, doi:10.1016/j.watres.2011.03.028.

De Gregorio, S., Gurrieri, S., and Valenza, M., 2005, A PTFE membrane for the in situ extraction of dissolved gases in natural waters: Theory and applications: Geochemistry, Geophysics, Geosystems, v. 6, doi:10.1029/2005GC000947.

Hamme, R.C., Berry, J.E., Klymak, J.M., and Denman, K.L., 2015, In situ O2 and N2 measurements detect deep-water renewal dynamics in seasonally-anoxic Saanich Inlet: Continental Shelf Research, v. 106, p. 107–117, doi:10.1016/J.CSR.2015.06.012.

Hammer, Ø., Harper, D.A.T., Ryan, D.D., and Ryan, P.D., 2001, PAST : Paleontological statistics software package for education and data analysis: Palaeontologia Electronica, v. 4, p. 9, doi:10.1016/j.bcp.2008.05.025.

Hari, P., Pumpanen, J., Huotari, J., Kolari, P., Grace, J., Vesala, T., and Ojala, A., 2008, High-frequency measurements of productivity of planktonic algae using rugged nondispersive infrared carbon dioxide probes: Limnology and Oceanography: Methods, v. 6, p. 347–354, doi:10.4319/lom.2008.6.347.

Hill, A. V., 1910, The possible effects of the aggregation of the molecules of haemoglobin on its dissociation curves: Proceedings of the Physiological Society, v. 53, p. 1689–1699, doi:10.1017/CBO9781107415324.004.

Hirano, T., Kim, H., and Tanaka, Y., 2003, Long-term half-hourly measurement of soil CO2 concentration and soil respiration in a temperate deciduous forest: Journal of Geophysical Research Atmospheres, v. 108, p. 1–13, doi:10.1029/2003JD003766.

Jarvie, H.P., King, S.M., and Neal, C., 2017, Inorganic carbon dominates total dissolved carbon concentrations and fluxes in British rivers: Application of the THINCARB model – Thermodynamic modelling of inorganic carbon in freshwaters: Science of the Total Environment, v. 575, p. 496–512, doi:10.1016/j.scitotenv.2016.08.201.

Jarvie, H.P., Sharpley, A.N., Brahana, V., Simmons, T., Price, A., Neal, C., Lawlor, A.J., Sleep, D., Thacker, S., and Haggard, B.E., 2014, Phosphorus retention and remobilization along hydrological pathways in karst terrain: Environmental Science and Technology, v. 48, p. 4860–4868, doi:10.1021/es405585b.

Jassal, R., Black, A., Novak, M., Morgenstern, K., Nesic, Z., and Gaumont-Guay, D., 2005, Relationship between soil CO2 concentrations and forest-floor CO2 effluxes: Agricultural and Forest Meteorology, v. 130, p. 176–192, doi:10.1016/j.agrformet.2005.03.005.

Jochheim, H., Wirth, S., and von Unold, G., 2018, A multi-layer, closed-loop system for continuous measurement of soil CO2 concentration: Journal of Plant Nutrition and Soil Science, v. 181, p. 61–68, doi:10.1002/jpln.201700259.

Johnson, M.S., Billett, M.F., Dinsmore, K.J., Wallin, M., Dyson, K.E., and Jassal, R.S., 2009, Direct and continuous measurement of dissolved carbon dioxide in freshwater aquatic systems-method and applications: Ecohydrology, v. 3, p. n/a-n/a, doi:10.1002/eco.95.

Joos, O., Saurer, M., Heim, A., Hagedorn, F., Schmidt, M.W.I., and Siegwolf, R.T.W., 2008, Can we use the CO2 concentrations determined by continuous-flow isotope ratio mass spectrometry from small samples for the Keeling plot approach? Rapid Communications in Mass Spectrometry, v. 22, p. 4029–4034, doi:10.1002/rcm.3827.

Kling, G.W., Clark, M.A., Compton, H.R., Devine, J.D., Evans, W.C., Humphrey, A.M., Koenigsberg, E.J., Lockwood, J.P., Tuttle, M.L., and Wagner, G.N., 1987, The 1986 Lake Nyos gas disaster in Cameroon, West Africa: Science, v. 236, p. 169–175, doi:10.1126/science.236.4798.169.

Knierim, K.J., Pollock, E., and Hays, P.D., 2013, Using Isotopes of Dissolved Inorganic Carbon Species and Water To Separate Sources of Recharge in a Cave Spring, Northwestern Arkansas, Usa: Acta Carsologica, v. 42, p. 261–276.

Kresse, T.M., Hays, P.D., Merriman, K.R., Gillip, J.A., Fugitt, D.T., Spellman, J.L., Nottmeier, A.M., Westerman, D.A., Blackstock, J.M., and Battreal, J.L., 2014, Aquifers of Arkansas-Protection, Management, and Hydrologic and Geochemical Characteristics of Groundwater Resources in Arkansas: U.S. Geological Survey Scientific Investigations Report 2014-5149:, doi:10.3133/sir20145149.

Kusakabe, M., and Sano, Y., 1992, The origin of gases in Lake Nyos, Cameroon, in Natural Hazards in West and Central Africa, Wiesbaden, Vieweg+Teubner Verlag, p. 83–95, doi:10.1007/978-3-663-05239-5_9.

Liu, S., and Raymond, P.A., 2018, Hydrologic controls on pCO2 and CO2 efflux in US streams and rivers: Limnology and Oceanography Letters, v. 3, p. 428–435, doi:10.1002/lol2.10095.

Lombardozzi, D.L., Bonan, G.B., Smith, N.G., Dukes, J.S., and Fisher, R.A., 2015, Temperature acclimation of photosynthesis and respiration: A key uncertainty in the carbon cycle-climate feedback: Geophysical Research Letters, v. 42, p. 8624–8631, doi:10.1002/2015GL065934.

Lowenstern, J.B., 2001, Carbon dioxide in magmas and implications for hydrothermal systems: Mineralium Deposita, doi:10.1007/s001260100185.

Manning, A.H., Solomon, D., and Sheldon, A.L., 2003, Applications of a Total Dissolved Gas Pressure Probe in Ground Water Studies: Ground Water, v. 41, p. 440–448, doi:10.1111/j.1745-6584.2003.tb02378.x.

Martin, C.R., Zeng, N., Karion, A., Dickerson, R.R., Ren, X., Turpie, B.N., and Weber, K.J., 2017, Evaluation and environmental correction of ambient CO2 measurements from a low-cost NDIR sensor: Atmospheric Measurement Techniques, v. 10, p. 2383–2395, doi:10.5194/amt-10-2383-2017.

McDermitt, D.K., Welles, J.M., and Eckles, R.D., 1993, Effects of temperature, pressure and water vapor on gas phase infrared absorption by CO2: LI-COR Technical Publication,.

McDowell, N. et al., 2008, Understanding the Stable Isotope Composition of Biosphere-Atmosphere CO 2 Exchange: Eos, Transactions American Geophysical Union, v. 89, p. 94, doi:10.1029/2008EO100002.

Moran, D., Tirsgård, B., and Steffensen, J.F., 2010, The accuracy and limitations of a new meter used to measure aqueous carbon dioxide: Aquacultural Engineering, v. 43, p. 101–107, doi:10.1016/j.aquaeng.2010.07.003.

Olah, G.A., Prakash, G.K.S., and Goeppert, A., 2011, Anthropogenic Chemical Carbon Cycle for a Sustainable Future: Journal of the American Chemical Society, v. 133, p. 12881–12898, doi:10.1021/ja202642y.

Pearce, J.M., 2012, Building Research Equipment with Free, Open-Source Hardware: Science, v. 337, p. 1303–1304, doi:10.1126/science.1228183.

Queiβer, M., Granieri, D., and Burton, M., 2016, A new frontier in CO2 flux measurements using a highly portable DIAL laser system: Scientific Reports, v. 6, p. 33834, doi:10.1038/srep33834.

Richter, D. deB., and Mobley, M.L., 2009, Monitoring Earth's Critical Zone: Science, v. 326, p. 1067–1068, doi:10.1126/science.1179117.

Ryan, M.C., Roy, J.W., and Heagle, D.J., 2015, Dissolved gas "concentrations" or "concentration estimates" - A comment on 'Origin, distribution and hydrogeochemical controls on methane occurrences in shallow aquifers, southwestern Ontario, Canada' by Jennifer C. McIntosh, Stephen E. Grasby, Stewart M.: Applied Geochemistry, v. 63, p. 218–221, doi:10.1016/j.apgeochem.2015.08.015.

Sánchez-Cañete, E.P., Scott, R.L., van Haren, J., and Barron-Gafford, G.A., 2017, Improving the accuracy of the gradient method for determining soil carbon dioxide efflux: Journal of Geophysical Research: Biogeosciences, v. 122, p. 50–64, doi:10.1002/2016JG003530.

Sanford, W.E., Shropshire, R.G., and Solomon, D.K., 1996, Dissolved gas tracers in groundwater: Simplified injection, sampling, and analysis: Water Resources Research, v. 32, p. 1635–1642, doi:10.1029/96WR00599.

Schimel, D.S. et al., 2001, Recent patterns and mechanisms of carbon exchange by terrestrial ecosystems.: Nature, v. 414, p. 169–72, doi:10.1038/35102500.

Schimel, D., Stephens, B.B., and Fisher, J.B., 2015, Effect of increasing CO2 on the terrestrial carbon cycle: Proceedings of the National Academy of Sciences, v. 112, p. 436–441, doi:10.1073/pnas.1407302112.

Scott, H.D., 2000, Soil physics: agricultural and environmental applications: Iowa State University Press, 421 p.

Serrano-Ortiz, P., Roland, M., Sanchez-Moral, S., Janssens, I.A., Domingo, F., Goddéris, Y., and Kowalski, A.S., 2010, Hidden, abiotic CO2 flows and gaseous reservoirs in the terrestrial carbon cycle: Review and perspectives: Agricultural and Forest Meteorology, v. 150, p. 321–329, doi:10.1016/j.agrformet.2010.01.002.

Soil Survey Staff, 2019, National Cooperative Soil Characterization Database:

Steven, A., Hodge, J., Cannard, T., Carlin, G., Franklin, H., McJannet, D., Moeseneder, C., and Searle, R., 2014, Continuous Water Quality Monitoring on the Great Barrier Reef.:, doi:na.

Stumm, W., and Morgan, J.J., 1996, Aquatic Chemistry: New York, NY, John Wiley & Sons, 1040 p.

Takahashi, T., 1961, Carbon dioxide in the atmosphere and in Atlantic Ocean water: Journal of Geophysical Research, v. 66, p. 477, doi:10.1029/JZ066i002p00477.

Tang, J., Baldocchi, D.D., Qi, Y., and Xu, L., 2003, Assessing soil CO2 efflux using continuous measurements of CO2 profiles in soils with small solid-state sensors: Agricultural and Forest Meteorology, v. 118, p. 207–220, doi:10.1016/S0168-1923(03)00112-6.

Urban, a. L., Gulliver, J.S., and Johnson, D.W., 2008, Modeling Total Dissolved Gas Concentration Downstream of Spillways: Journal of Hydraulic Engineering, v. 134, p. 550–561, doi:10.1061/(ASCE)0733-9429(2008)134:5(550).

Vereecken, H., Kamai, T., Harter, T., Kasteel, R., Hopmans, J., and Vanderborght, J., 2007, Explaining soil moisture variability as a function of mean soil moisture: A stochastic unsaturated flow perspective: Geophysical Research Letters, v. 34, p. 1–6, doi:10.1029/2007GL031813.

Ward, H.C., Kotthaus, S., Grimmond, C.S.B., Bjorkegren, A., Wilkinson, M., Morrison, W.T.J., Evans, J.G., Morison, J.I.L., and Iamarino, M., 2015, Effects of urban density on carbon dioxide exchanges: Observations of dense urban, suburban and woodland areas of southern England: Environmental Pollution, v. 198, p. 186–200, doi:10.1016/j.envpol.2014.12.031.

Welles, J.M., and McDermitt, D.K., 2005, Measuring carbon dioxide in the atmosphere, in Micrometerology in Agricultural Systems, doi:10.2134/agronmonogr47.c13.

Werner, C., and Cardellini, C., 2006, Comparison of carbon dioxide emissions with fluid upflow, chemistry, and geologic structures at the Rotorua geothermal system, New Zealand: Geothermics, v. 35, p. 221–238, doi:10.1016/j.geothermics.2006.02.006.

Yoon, T.K., Jin, H., Oh, N.-H., and Park, J.-H., 2016, Technical note: Assessing gas equilibration systems for continuous pCO2 measurements in inland waters: Biogeosciences, v. 13, p. 3915–3930, doi:10.5194/bg-13-3915-2016.

Chapter 5. Conclusions

Groundwater mixing and recirculation in hydrothermal systems

Determination of end-members and application of EMMA in the TVZ presented three key findings: 1, the low-temperature, groundwater end-members could be predicted using empirical spatial relationships between Cl concentrations and Cl/Br ratios with increasing distance inland, albeit with notable uncertainty for the most inland locations as the number of control points decreased; 2, while uncertainties exist in EMMA for hydrothermal and low-temperature end-members as applied here, EMMA using Cl and Br offered a simple and replicable method to assess groundwater mixing, particularly for hydrothermal surface features having lower fractions of the hydrothermal end-member; and 3, by incorporating information gleaned from this study and numerical simulations of hydrothermal systems to-date, distillation of meteoric solutes from phase separation and recirculation of meteoric solutes could be used to explain Cl/Br ratios of hydrothermal surface features having intermediate values of the low-temperature and hydrothermal end-members.

Directed efforts for the collection and analysis of dissolved Cl and Br in shallow groundwater across large areas along with more sophisticated spatial analyses could yield high accuracy, spatially distributed end-member prediction maps. These spatially distributed end-member maps would serve efforts to not only constrain groundwater mixing in hydrothermal systems, but a broad and diverse range of groundwater environments concerning movement and mixing in aquifer systems ranging from zero-order basins to continental-scale aquifer systems (e.g. High Plains Aquifer System, North America; Nubian Sandstone Aquifer Systems, northern Africa; other aquifers; Great Artesian Basin, Australia).

EMMA in the TVZ was implemented in this research as a two end-member mixing model between a low-temperature end-member and 'mixed' hydrothermal end-member. Meaning, the hydrothermal end-member and the individual contributions from either magmatic volatiles, water-rock interaction, or meteoric solute sources do not have to be individually solved, separately, when using EMMA. This serves as evidence of EMMA as a pragmatic approach in groundwater systems where end-members compositions are influenced by prior geochemical processes. This suggestion is pertinent not only in the TVZ, but elsewhere, globally, where monitoring of hydrothermal surface features seek to monitor mixing induced from natural variability or human-influenced (i.e. geothermal production). Understanding these changes in mixing ratios are critical to management of geothermal energy resources, volcanogenic monitoring, and conservation efforts of geoethermal areas (Burnell et al., 2016; Climo et al., 2016).

Tracing DIC and factors influencing DIC transport in hydrothermal watersheds

From investigation of DIC and δ^{13}_{DIC} relations along the Jemez River, four end-member groundwater compositions were inferred. Contributions from these end-members were found to be variable along the stream reach. Neutral-pH thermal waters were significant contributors of HCO_3 and CO_2 to streams and CO_2 was interpreted to rapidly degas. End-members determined in HCO_3-CO_2 yield space from the July 2018 survey relations were combined with estimated HCO_3-CO_2 loads from historical data at the Jemez River USGS stream gage in which seasonally greater HCO_3 and CO_2 loads were observed in the spring months. Moreover, these values plotted more towards the neutral-pH, thermal end-member. Previous studies presented interpretations that, while snowmelt comprises a fraction of streamflow, streamflow is primarily baseflow contributions from groundwater. As groundwater mixing between the thermal and non-thermal

waters is pervasive, it was interpreted that seasonal HCO_3 and CO_2 laods are derived from an increase of the thermal DIC to streamflow.

Systematically, with increased groundwater recharge, this increases groundwater levels, which in turn, increase groundwater contributions to baseflow. It is therefore speculated higher groundwater levels and baseflow contributions hydraulically generate greater mixing and discharge of pH-neutral thermal groundwater from the Valles Caldera groundwater system. This leads to greater DIC loads and, ultimately, greater HCO_3 exports and greater CO_2 degassing from streams. Previous studies have postulated 'groundwater scrubbing' to be the controlling factor of S fluxes at active volcanoes, it is possible groundwater-climate dynamics also drive HCO_3 and CO_2 fluxes from hydrothermal systems. Continued investigation into groundwater-climate-DIC feedbacks is needed.

Long-term, low-cost dissolved CO_2 monitoring

Presently, continuous, direct measurements of dissolved CO_2 in streams across Earth are limited compared to other environmental parameters, such as pH, temperature, and dissolved oxygen. The methods for fabrication, operating principles, field trials from Northwest Arkansas demonstrated operational capacity of measuring and recording dissolved CO_2 at approximately hourly intervals. With some modifications, reducing condensation potential within the headspace could be achieved to allow for much longer-term deployments than were observed at the Valles Caldera (< 2 to 4 weeks) where large temperature differences in the stream drove large temperature variability in the IRGA headspace. The CO2LAMP presents a simple, cost-effective solution that can easily be replicated and to which improvements are ongoing. Additionally, Arduinos and similar microcontrollers, such as ALog (Wickert, 2014) that are 'weatherproofed'

(i.e. lodge in waterproof cases) present an inexpensive alternative to more expensive data loggers, albeit with reduced 'out of the box' functionality.

Implications

Halogen mixing, modeling, and evolution in groundwater systems

Modeling efforts over the last three decades utilizing variable groundwater temperature, salinity, and permeability have indicated that varying proportions of modeled groundwater flow returning to the hydrothermal plume (i.e. recirculation). Meaning, hydrothermal groundwater flow is not always 'single pass' and, thus, not all groundwater entering the hydrothermal convection cell discharges at the surface. Conceptually, these are akin to vertical eddies.

It has been inferred this recirculation is a primary driver of increasing salinity with depth and time in geothermal areas (i.e. saline stratification). This research posits that a non-trivial amount of low-temperature groundwater is incorporated into hydrothermal circulation evidenced by varying degrees of dilution and lower Cl/Br ratios with high Cl concentrations at the Mokai geothermal areas in the TVZ. At present, the timing and groundwater flow paths associated with recirculation in numerical simulations are dependent on model parameterization. How this recirculation physically manifests within individual hydrothermal systems is likely site-dependent (similar to numerical simulation variation and model parameterization). Incorporation of Br into NaCl multiphase hydrothermal circulation models would vastly improve current knowledge of geochemical change throughout hydrothermal circulation and allow for further development of expanded testable hypotheses at the field-scale where model parameterization is specific to individual hydrothermal systems.

As the geochemistry of 'fossil' hydrothermal systems are mostly 'snapshots' or heavily overprinted, geochemically, long-term simulations (i.e. $> 10^5$ years) are of particular interest for

coupled NaCl-NaBr-H_2O evolution through time. Tracing these changes through model simulations would allow for an entirely new 'window' into the evolution Cl and Br within Earth's crust as NaCl-H_2O simulations have provided for ore-genesis and geothermal reservoir modeling.

Groundwater in the global carbon cycle

Characterizing DIC fluxes from groundwater systems (thermal and non-thermal) has been described as one of the most perplexing components of the geologic carbon cycle (Berner and Lasaga, 1989). While the principle of uniformitarianism states that the various forms of DIC fluxes from the lithosphere have not changed over time (Kerrick, 2001), the predominance of has likely varied, substantially. Greater understanding of the role of groundwater in modulating current DIC fluxes would greatly aid interpreting hydroclimatic feedbacks within the carbon cycle for Earth's past. Specifically, large shifts in ocean-terrestrial carbon cycles and related feedback within the hydrologic cycle are not well understood at present, let alone, during high CO_2 periods in Earth's history (e.g. Pleistocene epoch, Mesozoic period).

Expanding in situ observations and end-user capacity

Original-equipment-manufacturer gas analyzers are available for a number of other environmentally important compounds and elemental gases (e.g. CO, CH_4, N_2, Ar, O, He). For an IRGA-based sensor a theoretical formulation can be modified from the one presented here (e.g. CO, CH_4). Similarly, known constants for dissolved gases in water and sensor-operating principles could be combined to formulate operating principles of non-IRGA gas analyzers using a similar approach to the IRGA formulation presented in this research. Furthermore, as dissolved gas research encompasses a wide spectrum of interests, further development of low-cost,

continuous monitoring techniques based on research from this body of work have broad and diverse applications.

Reducing the costs of measurement acquisition and storage of environmental data will not only serve to expand hydrologic measurement stations, globally, but also invite a much more diverse range of users across numerous disciplines and localities (e.g. agricultural hydrology, environmental engineering, ecology), particularly those from underrepresented minorities and nationalities.

Understanding groundwater within the Earth System

Lastly, groundwater is a dynamic resource to which mixing among surface water and aquifers occur throughout the crust. As climate norms shift across the planet, groundwater presents a readily available, but finite water resource, particularly to drought-stricken areas. Increased abstraction and demand on the resource could yield unforeseen interactions of groundwater between aquifers and surface water bodies. While unintended, mixing between contrasting salinities and DIC chemistry may adversely affect conjunctive use by ecosystems and human populations. Implications from this research suggest broader characterization of halogens and DIC variability and implementation of lower-cost technologies could support water resource assessment and monitoring.

References Cited

Berner, R.A., and Lasaga, A.C., 1989, Modeling the Geochemical Carbon Cycle: Scientific American, v. 260, p. 74–81, doi:10.1038/scientificamerican0389-74.

Burnell, J., Campen, B. van, Kortright, N., Lawless, J., McLeod, J., Luketina, K., and Robson, B., 2016, Sustainability of TVZ geothermal systems: The regulatory perspective: Geothermics, v. 59, p. 225–235, doi:10.1016/J.GEOTHERMICS.2015.08.001.

Climo, M., Milicich, S.D., and White, B., 2016, A history of geothermal direct use development in the Taupo Volcanic Zone, New Zealand: Geothermics, v. 59, p. 215–224, doi:10.1016/J.GEOTHERMICS.2015.07.004.

Kerrick, D.M., 2001, Present and past nonanthropogenic CO2 degassing from the solid earth: Reviews of Geophysics, v. 39, p. 565–585, doi:10.1029/2001RG000105.

Wickert, A.D., 2014, The ALog: Inexpensive, Open-Source, Automated Data Collection in the Field: Bulletin of the Ecological Society of America, v. 95, p. 166–176, doi:10.1890/0012-9623-95.2.68.